INVESTIGATION OF ELECTROMAGNETIC INDUCTION RETRIEVALS OF SEA ICE THICKNESS USING MODELS AND MEASUREMENTS

by

Jesse Paul Samluk

A dissertation submitted to the Faculty of the University of Delaware in partial fulfillment of the requirements for the degree of Doctor of Philosophy in Electrical and Computer Engineering

Spring 2016

INVESTIGATION OF ELECTROMAGNETIC INDUCTION RETRIEVALS OF SEA ICE THICKNESS USING MODELS AND MEASUREMENTS

by

Jesse Paul Samluk

Approved: _____
Kenneth E. Barner, Ph.D.
Chair of the Department of Electrical and Computer Engineering

Approved: _____
Babatunde A. Ogunnaike, Ph.D.
Dean of the College of Engineering

Approved: _____
Ann L. Ardis, Ph.D.
Senior Vice Provost for Graduate and Professional Education

I certify that I have read this dissertation and that in my opinion it meets the academic and professional standard required by the University as a dissertation for the degree of Doctor of Philosophy.

Signed: _____

Cathleen A. Geiger, Ph.D.
Professor in charge of dissertation

I certify that I have read this dissertation and that in my opinion it meets the academic and professional standard required by the University as a dissertation for the degree of Doctor of Philosophy.

Signed: _____

Daniel S. Weile, Ph.D.
Member of dissertation committee

I certify that I have read this dissertation and that in my opinion it meets the academic and professional standard required by the University as a dissertation for the degree of Doctor of Philosophy.

Signed: _____

Robert L. Opila, Ph.D.
Member of dissertation committee

I certify that I have read this dissertation and that in my opinion it meets the academic and professional standard required by the University as a dissertation for the degree of Doctor of Philosophy.

Signed: _____

Xiang-Gen Xia, Ph.D.
Member of dissertation committee

I certify that I have read this dissertation and that in my opinion it meets the academic and professional standard required by the University as a dissertation for the degree of Doctor of Philosophy.

Signed: _____

Chester J. Weiss, Ph.D.
Member of dissertation committee

DEDICATION

This work is dedicated to:

Jesse William Samluk

Matilda DelGrosso Samluk

Gwen S. McWilliams

Louise Fidance

Paul J. Fidance I

Paul J. Fidance II

1LT Justin Smith

ACKNOWLEDGMENTS

"A failure is not always a mistake – it may simply be the best one can do under the circumstances. The real mistake is to stop trying."

-B. F. Skinner

"I do it because I can. I can because I want to. I want to because you said I couldn't."

-Unknown

There are so many people that I would like to thank that have helped me come all of this way to write this dissertation. First and foremost, I would like to thank my advisor, Dr. Cathleen A. Geiger, for making it all possible. Dr. Geiger gave me hope and a chance to fulfill my dream of obtaining my doctorate in this field, and to you, Dr. Geiger, I am completely indebted. No words can express how I truly feel. I'd also like to thank Dr. Tracy DeLiberty for introducing me to Dr. Geiger. Without you, the start of this project would have never even taken off! Additionally, I'd also like to thank my committee members: Dr. Dan Weile, Dr. Robert Opila, Dr. Xiang-Gen Xia, and Dr. Chester J. Weiss. To Dr. Weile, Dr. Xia, and Dr. Opila - I've known you all for many, many years, and I hope this work is a demonstration of the growth and maturity I've achieved during my time here since my undergraduate days. And to Dr. Chester Weiss, my external committee member from Sandia National Laboratories, thank you for all of the explanations with the APhiD model and other relevant technical discussions. I sincerely hope that our development opens the door for more

opportunities for the model. I took a chance in messaging you 4 years ago and I have learned a lot from you. Thank you all for being my esteemed mentors.

I would also like to thank the National Science Foundation for funding this research under award number ARC-1107725. Additionally, I would also like to thank the Delaware Space Grant College and Fellowship Program (NASA grant NNX10AN63H). Both programs helped me conduct research and finish this dissertation. Also, special thanks to Dr. James Kolodzey for technical discussions on electromagnetic theory.

As an aside, I come from military roots. I'd like to thank some of my close friends and comrades that I have had the honor to know and to serve with, in particular CPT Sarah Wadsworth, SFC Burt Hensley, CPT Starvonsky Gibbs, CPT Joseph Williams, MAJ Barry White, MAJ Roland Foss, CPT Roger Garcia and his wife Deanita. Thank you for being you! I'd also like to extend a warm thanks to past members of the 71st Transportation Battalion (United States Army) that I've also served with: COL (ret.) Mark R. Hicks, COL (ret.) Jennifer Reinkober, MAJ Annie Robinson, MAJ Barrick K. Elmore, CPT (CH) Joel Raoelina, and SFC Dondi L. Humphrey. Thank you – and FULL SPEED AHEAD! Other military personnel I'd like to acknowledge are BG (ret.) Tom Lauppe, BG (ret.) Frank Pontelandolfo, and MG (ret.) Tom Thomas, all from the Delaware Air National Guard, for their words of encouragement during trying times. Thank you all!

As this journey has taken many years, there are some people that I have to thank as they have helped me one way or another along the way: Dave Ramos, Mike Blyskal, Kjeld Krag-Jensen, Debbie Nelson, Kathy Forwood, Gwen Looby, Wendy Scott, Cathy Cathell, Chuck Hanavin, Kaci Middlemas, Colleen Leithren, Ingrid

Callaghan, Dr. Kenji Matsuura, Dr. Delphis Levia, Vicky Grypa, Brenda Radziewicz, Michele Jennings, Pam McDermott, Debbie Whitesel, Karen DiStefano, Terrie Kalesse, Christine Shinn, Kathy Werrell, Dr. Babatunde Ogunnaike, Dr. Charles Riordan, Dr. Mary Martin, Mary Zielinski, Eileen Burget, Scott Sorensen, Renny Kane, Dr. E. Rachel Bernstein, Penelope Wagner, Vicky Corradina, Dr. Chris Schuetz, Dr. Rick Martin, Dr. Tom Dillon, Dr. Ahmed Sharkawy, Dr. Xiaolin Lu, Dr. Chunchen Lin, Dr. Peng Yao, Dr. Rownak Shireen, Dr. Iftekhar Mirza, Dr. Caihua Chen, Binglin Miao, Dr. Mat Zablocki, Dr. Janusz Murakowski, Dr. Garrett Schneider, Dr. Shouyuan Shi, Lee Stein, Andrew Robbins, Timothy Hodson, Dr. Elton Marchena, Dr. Tim Creazzo, Dr. John Wilson, Dr. Liang Qiu, Dr. Andre Rauh, Dr. Rohit Nair, Dr. Tian Gu, Dr. Muzammil Iqbal, Dr. Anuraag Mohan, Dr. Greeshma Pisharody, Dr. Ray Wildman, Dr. James Mutitu, Christine Longhitano, Matt Konkol, Ryan Hickey, Ramsey Hazbun, John Hart, Dr. Jay Gupta, Dr. Nupur Bhargava, Josh Marks, Rodney McGee, Mike Stamat, Steve Janansky, Furkan Cayci, Nick Waite, Josh Sutterlein, Garrett Ejzak, Hristo Asenov, Dr. Chase Cotton, Phil Petty, Helen Meehan, Robert Crissman, David Hom, Jerrod Bates, the Wells family, Andrew Zeltner, Scott and Melissa Huffman, Ken Ehrenzeller, Leroy Daley, Ivan and Lora Learmont, Donald and Shawnna Williamson, Michael and Sharon Cesky, Drew LaRoche, Gerald Oravitz, Dr. Jirar Helou, Dr. John Pelesko, and Dr. Fiorabla Cakoni. I'd also like to specially recognize Dan Mackrides and Stephen Kozacik – you guys rock! Thanks for keeping my head in it when things were getting tough – I can't thank you enough! Additionally, I'd like to thank: Yang Song and family, Paul Schweiger, Renier Zambrano, Bradley Miller, Pat Kozacik, Kerel Way, Matt Dolson, LaMont Cannon, Becky Unruh and family, Maryann Durham, Carter McCoy and family,

Marquita Howard, LaShawn Jones, Mark Luck, Ronitha McCray, Joel Kellem, MSG (ret.) Kenneth E. Younker, Julie Vari, Stephanie Hurst, Gloria Cook, the Smolka family, Cyndy Flynn, Lisa Hitchens, Joe Opalach, Mark Cockeril, Carl and Patsy Roock, Clayton and Sherri Gebhart, Tina Akers, Kevin Gephart, Nicola Trincia, Tanielle Savage, Mercedes Durant, Penny Armstrong, Denise Emory, Lori Spader, John Kempa, Augustine Appiah, Diak Toure, Siani Howard, Donna Brady, Donna Ellis, Rich Erb, Erica Wood, Joey Baltar, Bobbie Conner, Sang "Sam" Lee, Ann Hershberger, Devan Glaviano, Vincent Colombo, Sandra Popoca, Tina Hadik, Joan Powers, Patience Gowan, Amanda Taylor, Kevin Dailey, Randi Green, Amitabh Sharma, David Workman, Philamena Sagoe, John D'Amato, Steve Masters, Robert Pagano, Jeff Wood, Shane Collins, Ronnie Johansen, Matt McGilloway, Andre "Andy" Letnianczyk, Yoel Moore, Aniaya Motley-Harris, Maya Graves, the Chaposky family, the Steinbrunner family, the Gruss family, the Davis family, the Kuss family, the Kinch family, the Devries family, the Wick family, the Soucy family, the Walker family, the Chaposky family, the Alvarez family, Jevonia Harris, Frank Eastman, Stacy Weile, Amanda Wise, Becky Kinney, Jann Sutton, Dr. Nancy O'Laughlin, Mathieu Plourde, Erin Sicuranza, Debbie Jeffers, Paul Hyde, Sandy McVey, Mu He, Rich Copley, Mengyu Li, Paul Rickards, the Fawcett and Sarver families, Tom and Linda Cofran, Justian Neely, Connie Threet, Stacy Taylor, Ange Dixon, Dr. Aubrey de Grey, Dave Mays, Ginger Noon, Mary Ellen Naugle, Charlsie Hurley, Katelynne Lord, Lauren Lord, Anne Golematis, and Robin Marks. Thank you all for your support over the years. I sincerely apologize if I missed anyone from this extended list!

Last, but finally not in the least, I'd like to thank my family, especially to all of my numerous relatives from my Mom's side (Fidance) and my Dad's side (Samluk) that have supported my through the years – I thank all of you!

To my mother, Michele, and to my father, John: Mom and Dad, I know it has been a long, tough road, and many things have happened, good and bad, through all of these years. I know there are times when I wanted to quit and give up. But your love and support drove me to complete this dissertation. To my sister, Marissa (and her husband Shawn) and to my twin sister, Christina (and her husband Jeremy. And of course all my awesome nephews Carl, Paxton, Jacob, and Alexander!) – thank you both for your patience and understanding. You both are the best sisters a brother could ever ask for. I love all of you!

With that, I would like to close my acknowledgements with two quotes:

"Free at last! Free at last! Thank God Almighty, we are free at last!"

-Dr. Martin Luther King, Jr., "I Have A Dream" – 1963

"What a long, strange trip it's been."

-The Grateful Dead – "Truckin'"- 1970

TABLE OF CONTENTS

LIST OF TABLES

LIST OF FIGURES

ABSTRACT

Using sea ice as a test material, this dissertation explores how electromagnetic responses interact with low-induction-number composite materials as a function of instrument footprint size and shape. This research combines several interdisciplinary topics including electrical engineering, materials science in composites, signal processing, and the geophysics of sea ice itself. Specifically, this work explores the development of new best practices that address consistency issues with electromagnetic induction instruments used on sea ice that employ electrical conductivity as a material property measurement. It does so by using two methods: modeling and measurements. For modeling, a three-dimensional, full-physics, heterogeneous model is used to investigate the electromagnetic field response of several sea ice cases. These cases include changing the material makeup of the sea ice, as well as using different transmitter locations and orientations, with the focus being how instrument footprint varies in each simulated case. For measurements, a co-calibration routine, among two physically different EM induction instruments in terms of instrument footprint, is developed and analyzed. Since these types of instruments are commonly used to measure conductivity in sea ice environments, historical calibration routines are only valid for one instrument at a time. The developed method presented herein provides a statistical solution for the material conductivities of both sea ice and seawater, as well as a solution for the actual ice thickness. These solutions are all based on field measurements made on sea ice during a data collection event held in Barrow, Alaska, in March 2013.

Chapter 1

INTRODUCTION

Incorporating the principles of electromagnetics into sensing subsurface interfaces has developed various mature technologies, such as ground penetrating radar, radio echosounding, electromagnetic (EM) induction, and even millimeter-wave imaging to name a few. The general problem of subsurface interface detection of structures complicates quickly when geophysical composite materials are involved. In general, composite materials are a result of the combination of two or more different materials that have different physical properties into one material, where the combined material (the composite) has different physical characteristics then the individual components. Some examples of typical composite materials are aluminum alloys, cement, and plastics. In geophysical terms, composite materials can be clay, soil, and sea ice. Since the physical properties of these geophysical composite materials are constantly dynamic, where their characteristics change based on environmental factors, subsurface interface detection is a constant challenge. Therefore, electromagnetics is key in this area since it involves understanding the dynamic behavior of a composite material to accurately and successfully define interface detection.

As mentioned previously, one geophysical composite material is sea ice. A particular area where electromagnetics is used is in determining sea ice thickness by way of measuring electrical conductivity levels present in the sea ice and surrounding media, such as seawater, snow, and air, by non-invasive means. A similar, but vastly

different, scenario to calculating sea ice thickness by conductivity measurements would be locating a landmine in buried soil. The objective in this example is to locate the device by the change in conductivity levels by subsurface interface detection, since both the landmine and surrounding soil have different conductivity levels. Furthermore, non-invasive means are required so that the landmine does not detonate.

In terms of detecting conductivity changes in sea ice in order to calculate its thickness, sea ice is itself a low-conductive composite material, and has a bulk conductivity on the order of 20 mS/m [1]. The reason why sea ice is considered a composite material is that it is, by definition, frozen seawater. By extension, seawater is also considered a composite material since it contains unfrozen water and salt (i.e., a combination of sodium ions and chloride ions), and has a higher bulk conductivity value than sea ice, on the order of 2500 (mS/m) [1]. It is important to note here that natural variability in conductivity occurs in the sea ice and seawater, and bulk measurements are used for simplifying calculations. While the obvious difference between sea ice and seawater is that one is frozen and the other is fluid, the explanation for a lower conductivity value in sea ice is due to the physical process of brine rejection. When ice starts to form (called frazil ice crystals [2, 3]), salt accumulates into water droplets, which constitutes brine. Some of these droplets are expelled back into the ocean, and others remain in the ice structure. These brine droplets, which are more saline than the surrounding ice, drain over time. The drainage of these droplets reduces the salinity, and therefore the electrical conductivity, of the sea ice [2]. Temperature also has an effect on the natural variability in sea ice conductivity, as the melting and freezing cycles impact the brine content in the ice structure. On a molecular level, the salt ions that comprise brine

contain an electrical charge, and the more ions present, the more conductive ice is, and vice versa [4].

Since conductivity is defined by how well electrical current flows in a material, current flow occurs in sea ice due to the presence of two components: a magnetic field and a conductor. In order to measure the conductivity of the sea ice and surrounding media, while being non-invasive so that the sample under study is undisturbed, an EM induction instrument is commonly employed to meet these requirements. EM induction instruments contain two coils that function as self-contained dipoles; one a transmitter coil, the other a receiver coil. The transmitter coil produces an alternating current at a particular frequency, usually in the kilohertz range, and creates a primary magnetic field in the space around the transmitter coil itself as well as the material below the transmitter. This magnetic field penetrates the sea ice and seawater underneath. The interaction of the primary field, which is a changing magnetic field, with the material underneath the transmitter induces small eddy currents in the material underneath the instrument. At this stage, the sea ice and seawater are electrically conducting, though seawater is more conductive than sea ice due to the ions being held by the intermolecular bonds in ice [5]. These eddy currents produce a secondary magnetic field that, along with the primary magnetic field that is a result of the alternating current produced in the transmitter coil, is detected by the receiver coil. The magnetic field values, along with the operating frequency and the coil separation of the instrument, provide a quantity referred to as “apparent conductivity” to the user. Apparent conductivity, in this context, can be defined as a representation of the electrical conductivity of an equivalent homogenous earth given by the integrated contribution from all the materials sensed by the receiver. Additionally, the

measurement of apparent conductivity is proportional to the ratio of the received primary and secondary magnetic field by way of low-induction-number theory [6]. This theory states that if the operating frequency is so low that the skin depth is much greater than the coil spacing, the magnitude of the secondary magnetic field is directly proportional to the ground conductivity [7].

Even though these apparent conductivity measurements at low-induction numbers provide necessary data to determine ice thickness, they do not tell the whole story. Since apparent conductivity is the contribution of all materials below the receiver, the sea ice/seawater interface still needs to be defined in order to provide a thickness. For further insight, these apparent conductivity measurements historically rely on one-dimensional (1D) approximations to a homogenous layered-earth solution to relate how the fields react with the material underneath the EM induction instrument. One such approximation is that sea ice conductivity is negligible. This approximation alone does not account for various physiographic features in sea ice, such as pressure ridges, cracks, and even brine intrusions form the seawater into the sea ice. Additionally, these historical approximations generalize instrument footprint to the 1D space, where the footprint increases with height. Instrument footprint is defined as the area contributing to a measurement made by an instrument. These historical thoughts on instrument footprint, along with the 1D approximations, can affect the overall accuracy of the ice thickness result. Since sea ice itself is three-dimensional (3D), what is needed is a 3D full-physics, heterogeneous EM model to show how the EM field responses react to a change in material properties (i.e., interface detection), and how instrument footprint is affected, when the situation comprises of weakly conductive sea ice in contrast to stronger conductive seawater.

A model is an important first step to map the subsurface interface between sea ice and seawater to better improve accuracy in thickness measurements. As such, it provides a unique opportunity to explore, in detail, the effects of electromagnetic responses in a given composite material matrix in relation to subsurface interface detection in a general sense. However, the model currently uses simulated data in order to explore the EM response at the interface. Therefore, actual in situ field-collected data needs to be included, and also how it is used to calculate thickness must be considered and discussed. Since EM induction instruments collect apparent conductivity, this quantity can be related to ice thickness through various numerical routines, such as non-linear regression and digital filter techniques. While these routines provide a thickness result, they only establish thickness for one instrument at a time, and need to be recalculated for each additional instrument used. Additionally, some parameters established with these numerical routines have no geophysical meaning. What is needed to improve thickness accuracy with actual data is a way to co-calibrate multiple instruments in a statistically consistent manner to compare thickness measurement results between instruments of different footprint size with the type of dipole construct exhibited in using the EM induction technique. This routine could give insight into the general case of how a composite material matrix affects the actual field collected data from instruments that have different instrument footprints.

In an effort to explore these areas of increasing accuracy in sea ice thickness by way of modeling and developing a new calibration approach for in situ data, this dissertation focuses on the following science question:

How can different aspects of geophysical composite properties, such as material conductivity, be used to improve the accuracy of sea ice thickness measurements based on numerical-modeling techniques and electromagnetic induction field instruments?

This question will be answered by exploring the following topic areas:

1) Objective 1 – Simulate field excitations of level and deformed sea ice with a 3D full-physics heterogeneous model in order to analyze field responses of multiple geophysical composite materials.
2) Objective 2 – Develop a co-calibration algorithm among different EM induction instruments based on ground truth thickness data collected from a field excursion in Barrow, Alaska, during 2013.

The anticipated impact of this research touches on three important areas: 1.) in-depth analysis of the full three-dimensional electromagnetic field response when it interacts with sea ice, 2.) challenging long-standing assumptions about how sea ice can be treated in terms of dimensionality, and 3.) advancing the level of knowledge that could provide the capability to develop new types of instruments that collect data more accurately in the future.

Therefore, in the context of this research dissertation, I outline these objectives in the following manner: Chapter 2 comprises a literature review, Chapter 3 provides the necessary mathematical background for this thesis, Chapter 4 is a modeling study that explores the use of a 3D numerical simulator to provide EM responses of several cases of sea ice to take a closer look at how instrument footprint and subsurface detection is affected by different physical properties, Chapter 5 describes the fieldwork conducted in Barrow, Alaska, and presents the mathematical theory for the

co-calibration algorithm, Chapter 6 is an analytical study that explores a co-calibration routine for two separate EM instruments based on the fieldwork and theory presented in Chapter 5, and Chapter 7 concludes this dissertation with responses to the central question posed for this research work.

Chapter 2

LITERATURE REVIEW

This chapter provides the necessary background to describe EM induction principles as they apply to the mapping of low-induction-number composite-layered materials. This chapter is organized into four sections. The first section presents a brief historical perspective of how EM induction instruments came into use when measuring sea ice. Additionally, it also presents alternatives to using EM induction in a sea ice environment The second section reviews the conceptual background for electromagnetic induction in the kilohertz range interacting with sea ice. It also discusses important concepts of electrical skin depth and instrument orientation. The third section reviews existing response functions used with EM induction units, depending on instrument orientation. The fourth section discusses the weakness of existing EM induction techniques at low induction numbers with respect to sea ice as the chosen test material. The goal of these summaries is to highlight the connections between instrument measurements of integrated surface apparent conductivity and layered composite materials with differing material conductivities within the low-induction-number range.

2.1 History of EM Induction on Ice-Covered Seas

For the purposes of this dissertation, since EM induction instruments are interacting with sea ice, it is necessary to present a brief historical overview of how EM induction became involved with measuring sea ice during the modern era (1940s

onward). During the Cold War, the study of sea ice thickness was based on a response to several factors. One such example was a response to submarine attack strategy, in which both the Soviet and US Navies would hide missile-launching submarines below pack ice where the inherent acoustical noise made detection very difficult [8]. One method explored during the Cold War to aid in determining ice thickness and counter these threats was with an EM induction instrument [9]. EM induction instruments were historically used by geophysicists to study strong conductivity contrast to the background soil, such as with ore bodies, groundwater, or even unexploded ordnance [1]. In turn, these instruments were applied to sea ice since this environment provides an excellent contrast between weakly conducting sea ice and stronger conducting seawater [9, 10].

So how is information collected with an EM induction instrument on sea ice used today? The accurate measurement of sea ice provides critical information for decision making in areas of environmental and climate policy, logistics operations, civil infrastructure near sea ice, and national security issues as sea ice opens up new shipping lanes for commerce [11]. But what is the requisite accuracy of ice thickness estimates for policy decision makers? From the existing literature [12,13], EM induction instruments can measure thickness of flat ice to within 10% accuracy. For ridged ice, the uncertainties exceed 10%, with one main reason being footprint size and shape not being accounted for in those measurements. Therefore, if the requisite accuracy were to be quantified, ideally the uncertainty should not exceed 10% for both level and ridged ice for all measurement platforms (not just with using EM induction).

In the area of environmental and climate policy, Arctic sea ice, referred to as "Earth's air conditioner", is important since it keeps the polar region cold and also helps moderate the global climate as a whole [14]. For both logistics operations and civil infrastructure, the Arctic Ocean is a strategic sea route not only as described for the military, but also for commercial operations, both locally and abroad. Additionally, structures such as oil drilling platforms could be affected by changing ice conditions, as well as inaccurate ice thickness measurements. Here, the consequences could potentially be catastrophic. For example, if the ice thickness was underestimated in the face of changing ice conditions, structures such as oil drilling platforms could be destroyed since they would be constructed on ridged ice not accounted for in measurements instead of being constructed on a more secure footing, which would cause the platform to become unstable and potentially cause injuries. Another example of how changing ice conditions affect commercial operations is with the Prudhoe Bay oil fields in Alaska that lie on the shore, where pollutants can become an issue due to sea ice pattern change and would contaminate wide areas undetected beneath the ice cover [15]. Therefore, sea ice acts like a filter as well as an air conditioner. The Arctic also provides the shortest shipping route between Europe and Asia. Normally, ships have to sail around Africa, the Panama Canal, or in increasingly hostile seas to travel between these continents, but as sea ice continues to decline, routes continue to be tested and expanded into longer summer shipping seasons [15]. Using established scientific principles, one can address fundamental science questions, such as how the ice thickness relates to changes in the climate index (such as the Arctic Oscillation and the North Atlantic Oscillation [16]), how to develop a non-invasive method to measure something while preserving it, and how changes in sea ice thickness can possibly

project how it might recover. The next section provides alternatives to using EM induction on sea ice.

2.1.1 Alternatives to EM Induction

Outside of the EM induction method, there are other methods used to quantify sea ice thickness, such as satellites [17, 18], submarines and autonomous water vehicles by way of upward looking sonar [19], ground penetrating radar (GPR), and radio echosounding. While this is an incomplete list of all the methodologies used to collect sea ice information, the following examples are mentioned along with their respective strengths and weaknesses. Satellites can measure the largest swaths of ice compared to all methodologies, but the expense of resolution can be a concern. Submarines inherently measure sea ice from the bottom of the ice structure, but cannot capture topside information (such as snow thickness). GPR has been used successfully with freshwater ice, but has only proven partly successful with sea ice due to the brine content, which limits the propagation distance of the GPR signal [20]. Radio echosounding has achieved some success when used on glaciers, but emits pulse lengths that are too large to measure sea ice [20]. Additionally, to include EM induction with these examples, it provides rapid data collection, but a mathematical correlation from apparent conductivity data to sea ice thickness is always needed. However, the EM induction method compliments most existing methodologies used for sea ice, such as satellites and submarines, because it provides ground truth data for these systems. EM induction systems also provide repeatability and time series capability.

2.2 Electromagnetic Induction Fundamentals

Figure 2-1 can be used as a visual reference to explain how the EM induction technique is levied on sea ice; it shows a transmitter-receiver pair separated by a coil spacing distance *r*. As introduced in Chapter 1, the transmitter is a coiled wire configured to generate a sinusoidal-varying electric current [7] at a specific low-frequency *f* (1's of kHz). The electric current sets up a time-harmonic primary magnetic field *P* which emits spherically from the transmitter. The nearby conductive seawater responds to the emitted primary magnetic field by generating electric eddy currents, which, in turn create their own secondary *S* magnetic fields. Since the secondary magnetic fields are passively responding to the primary field, the response defines the induced magnetic field [21]. With regard to a sea ice environment, induction takes place in a thin layer under the ice because the more conductive seawater prevents deeper penetration of the fields [1]. This limiting factor is due to signal absorption and scattering in the ice [22]. Absorption is where electromagnetic signals become attenuated when travelling through a medium, and scattering occurs when the signal is deflected from a straight path due to material obstacles, such as roughness and inhomogeneous matter within the medium. In essence, using an EM induction instrument on sea ice is an ideal case for an approximate two layer system, that being the low-conductive (or highly resistive) sea ice against an infinitely deep, more conductive seawater as the background composite material [1].

For completeness, the transmitter and receiver use complex signals both containing in-phase (real) and quadrature (imaginary) components with the secondary electric and magnetic responses being 90° out of phase with the primary fields [7]. With frequency domain EM instruments that operate in low-induction numbers, the secondary field is 90° out of phase with the primary field [6]. Essentially, the receiver

coil of a low-induction-number magnetic dipole pair behaves like an antenna to detect the magnetic field produced by nearby geophysical materials from eddy currents that are induced by the transmitter. Subsequently, the apparent conductivity quantity reported to the user is proportional to the ratio of the secondary (quadrature) magnetic field divided by the primary magnetic field [6]. In order to relate apparent conductivity to an actual thickness, physical sea ice measurements are obtained using the drill hole method. The drill hole method uses large augers to drill holes in the ice, which allows the thickness to be determined with measuring tape. While the drill hole method could be considered more accurate because of its inherent nature of providing a measured thickness, it is a slow process. When compared to EM induction units, the drilling equipment used for this method can be very heavy. On the other hand, EM induction units provide apparent conductivity information rapidly (with the push of a button). To sum up, apparent conductivity is a bulk average estimate of composite material layers with averaging weights applied based on EM field propagation principles.

Additionally, the distance between the coils r is small compared to the electrical skin depth of the surrounding materials. As an important principle in electromagnetic theory, the electrical skin depth (commonly referred to as skin depth) of any material can be calculated to determine how far a signal will penetrate in a material, given the frequency of the instrument, the permeability of the material, and the conductivity of the material. Physically, the skin depth of a material can be defined as the distance in the halfspace that a propagating plane wave has travelled when its amplitude has been attenuated by e^{-1} of the amplitude at the surface. Halfspace is a geophysical term that means the material beneath the surface has the same physical properties as far as an instrument can detect [23]. In other words, halfspace is a

volume where half is air and the other half has constant physical parameters, such as conductivity, salinity, etc. [24]. The skin depth calculation of a physiographic material, such as sea ice, is also an important metric in determining the variability of instrument footprint. It can be defined mathematically as

$$\delta = \sqrt{\frac{2}{\omega \mu_0 \sigma}} \ , \tag{2.1}$$

where ω is the angular frequency, μ_0 is the permeability constant of free space (4π * 10^{-7} henries/meter), and σ is the conductivity of the material. The angular frequency is defined as

$$\omega = 2\pi f \ , \tag{2.2}$$

where f is the temporal frequency (Hertz). To put Equation 2.1 into words, the amount of signal that is able to penetrate a given medium decreases with either increasing frequency or increasing material conductivity.

EM induction instruments can also be used in different dipole configurations. Depending on the orientation used, the penetration depth of the transmit signal, as well as the information collected at the receiver, become affected. These configurations consist of a vertical dipole mode and a horizontal dipole mode [6]. In the vertical dipole mode, the dipoles are parallel to the surface under measurement, and the magnetic field is normal to the surface. In contrast, using the horizontal dipole mode means the dipoles are normal to the surface, and the magnetic field is parallel to the surface under measurement. The vertical dipole mode allows for more exploration depth when compared to the horizontal dipole mode. However, the horizontal dipole mode is more sensitive to responses near the surface than the vertical dipole mode since the relative response contribution from the materials underneath the instrument

is large, but decays with depth. For simplicity in this thesis, we will follow the terminology presented in [21], and subsequently label the vertical dipole mode as "horizontal coplanar" (HCP), and the horizontal dipole mode as "vertical coplanar" (VCP). Figure 2-2 demonstrates the respective geometries of HCP and VCP.

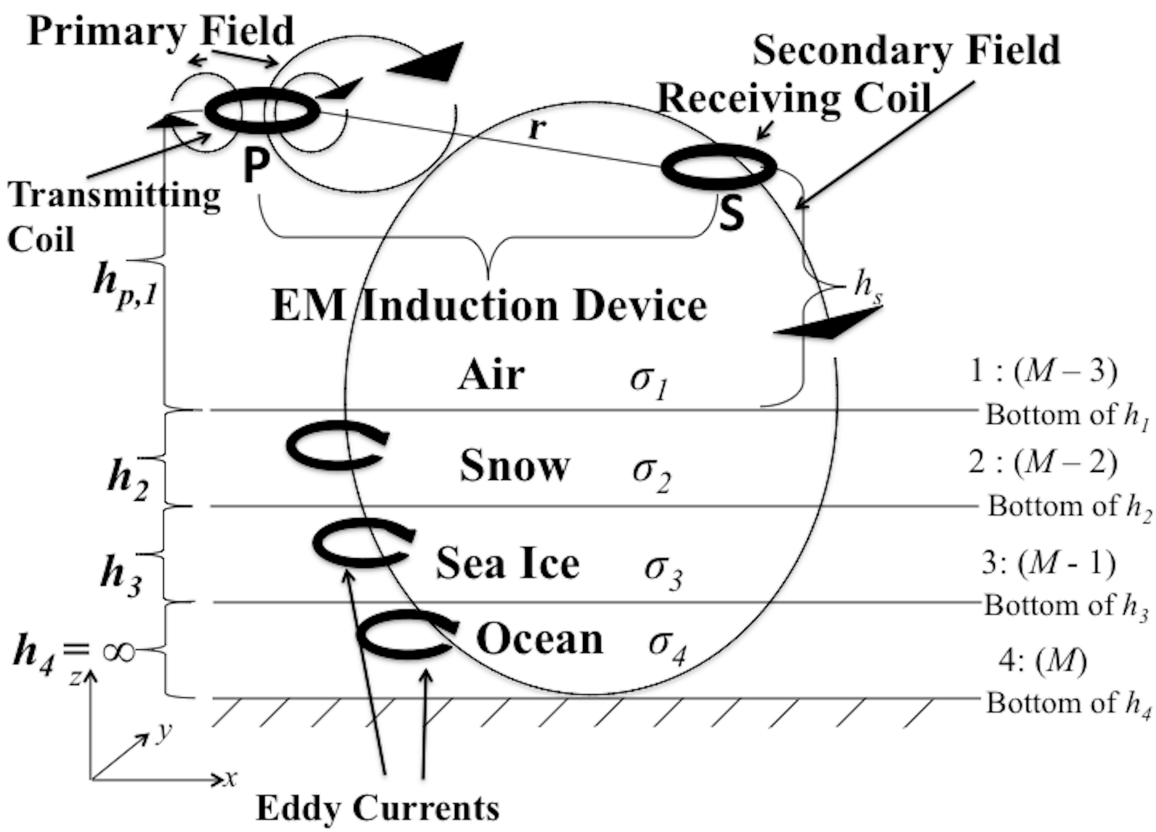

Figure 2-1. Schematic of EM induction concept through multiple level materials. Note that this schematic represents a vertical dipole configuration, which is depicted by having both the transmitting and receiving coils in a horizontal orientation. The secondary field is induced in the receiving coil by the eddy currents that were created (induced) in each material by the transmission of a primary field from the transmitter coil, separated by a fixed length *r* from the receiver coil. *M* represents the number of layers, *h* is the height of the layers, and σ is the conductivity of a particular material layer.

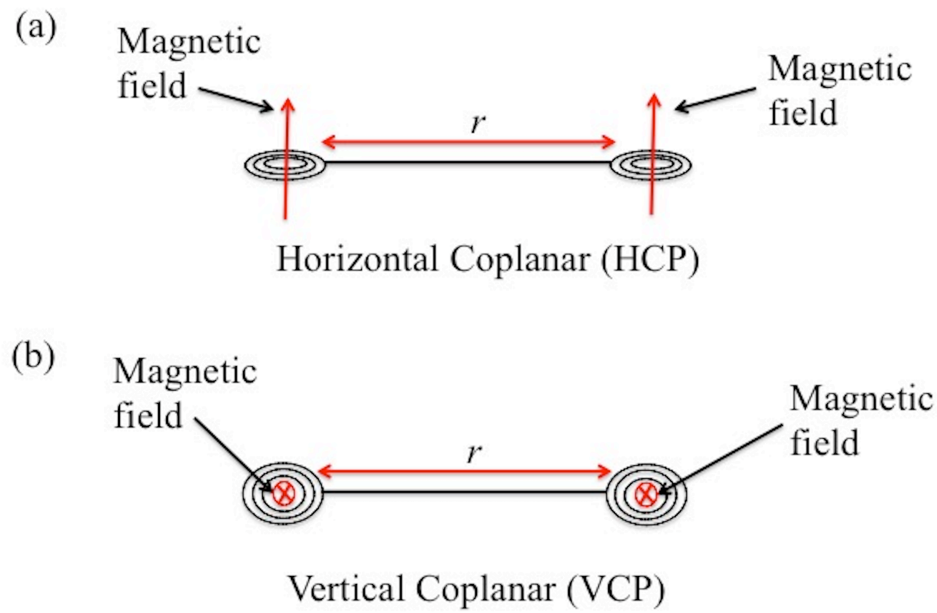

Figure 2-2. EM induction instrument dipole geometries (a) Horizontal coplanar (HCP) is the dipole configuration where the dipoles are parallel (horizontal) to the surface under measurement, and the magnetic field is normal to the surface. (b) Vertical coplanar (VCP) is where the dipoles are normal (vertical) to the surface under measurement, and the magnetic field is parallel to the surface, indicated by the red circles with a red "X" through it. Here, the coil spacing *r* is shown for clarity.

2.3 Responses of EM Induction Instruments

With the previous section establishing how an EM induction unit (Figure 2-3) operates on a physical level, the response functions of these instruments must now also be defined. There are two types of functions used with EM induction instruments: relative response functions and cumulative response functions. First, the relative response function ϕ is defined as the relative contribution to the secondary magnetic field coming from a thin layer at a certain distance in a homogenous halfspace [6]. This function also gives the material's relative contribution at different distances to the

apparent conductivity measured by the EM induction instrument [6]. The relative response function in the HCP mode can be defined mathematically as

$$\phi(\zeta)_{HCP} = \frac{4\zeta}{\left(4\zeta^2+1\right)^{3/2}} \quad , \tag{2.3}$$

where

$$\zeta = \frac{z}{r} \quad , \tag{2.4}$$

and z is the depth. Since this function is related to a physical dimension of the instrument itself (r), the relative response for the VCP can be stated as

$$\phi(\zeta)_{VCP} = 2 - \frac{4\zeta}{\sqrt{4\zeta^2+1}} \quad . \tag{2.5}$$

Figure 2-4 displays the relative responses for both HCP and VCP as mathematical functions relative to a certain distance ζ, and shows that the depth of penetration is greater for HCP when compared to VCP. For sea ice thickness scenarios, VCP mode will be a good choice for flat ice that is at most 3 m thick since the relative contribution is at a maximum at the surface, which demonstrates that it is sensitive to conductivity changes for thinner ice. If the study focuses on ridged ice (greater than 3 m), then HCP should be used to provide further penetration depth, as this mode typically has a maximum depth of investigation limited to about twice the coil separation [25].

Second, the cumulative response function represents the multi-layer relative contribution to the secondary magnetic field from all material below a certain distance, not just a thin layer as in the case of defining the relative response. Simply put, it is the

mathematical integration of the relative responses, where the integration is also the total secondary magnetic field at the receiver [6]. Additionally, if the coil spacing r is less than the skin depth of the cumulative layers, as is the case with materials that have low induction numbers such as sea ice, apparent conductivity for a simple two-layer system can be stated as

$$\sigma_a = \sigma_1\left[1 - R(\zeta_1)_{HCP,VCP}\right] + \sigma_2 R(\zeta_1)_{HCP,VCP} \tag{2.6}$$

where σ_a is the apparent conductivity recorded by the instrument, σ_1 and σ_2 are material conductivities for layers below the EM induction instrument, and the cumulative response functions $R(\zeta)_{HCP,VCP}$ are defined per polarization, and the subscript of "1" indicates the response function of the first layer. Per [6], the cumulative response in HCP is expressed as

$$R(\zeta)_{HCP} = \frac{1}{\sqrt{4(\zeta)^2 + 1}} \ , \tag{2.7}$$

and for VCP,

$$R(\zeta)_{VCP} = \sqrt{4(\zeta)^2 + 1} - 2(\zeta) \ . \tag{2.8}$$

The response curves for these equations are shown in Figure 2-5. The information on this curve works with respect to thickness of different materials and their placement in a layered composite by relating measured field quantities to unknown values. As an example to clarify this concept, assume a two-layer system such as sea ice (layer 1) and seawater (layer 2) where the EM induction instrument sits directly on top of the sea ice surface, their respective bulk material conductivities are known, as well as the

ice thickness and the coil separation. The information from Figure 2-5 provides a value for the cumulative response function *R*, where the measured thickness *z* of layer 1 is divided by the coil separation (i.e., Equation 2.4). This *R* value is valid for the space between the bottom of the instrument to the bottom of layer 1. Depending on the coil orientation, along with the material conductivities of layer 1 and layer 2, the determined *R* value (y-axis of Figure 2-5) is substituted into Equation 2.6 to provide an apparent conductivity result. This example, however, is only one possibility. Another possibility is if the apparent conductivity, the layer 1 thickness, and the coil separation are known, then the material conductivities of the layers can be deduced. Even the layer 1 thickness can be determined if all of the aforementioned parameters are known. Additionally, this concept also works with systems with more than two layers.

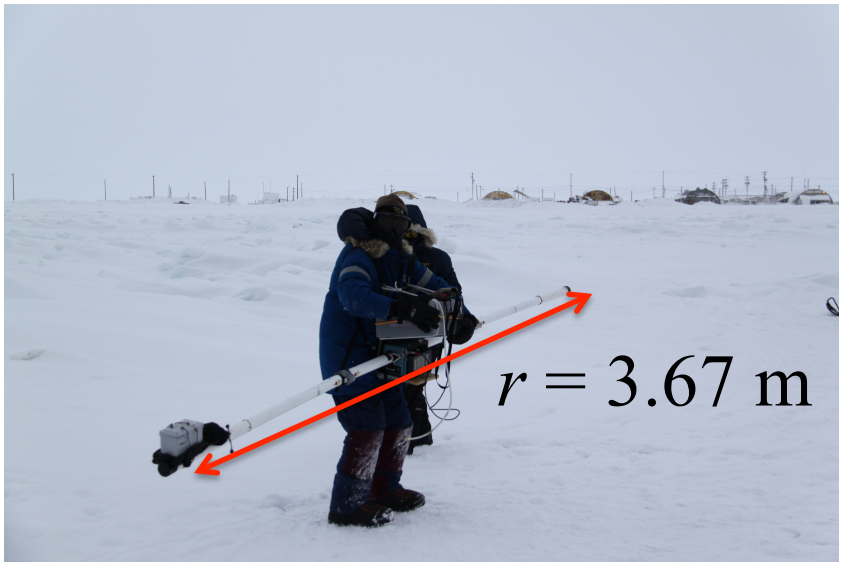

(a)

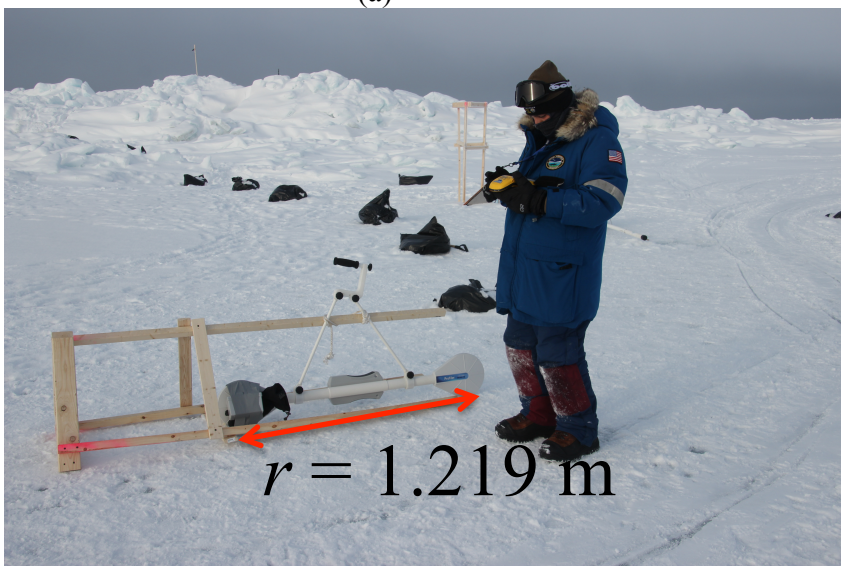

(b)

Figure 2-3. Examples of EM induction units used on sea ice. Panel (a) shows the Geonics Limited EM31-MK2 [26], and panel (b) shows the Geophysical Survey Systems, Incorporated (GSSI) EMP-400 [27]. Shown in both panels is the coil spacing *r* as discussed in Figure 2-1. Additionally, the GSSI EMP-400 is shown in the horizontal dipole configuration, where the transmit and receive coils are in the vertical orientation. These photos of the author were taken during a fieldwork excursion in Barrow, Alaska, during March 2013. These photos also display the environment that the EM induction units were used in. (*Photo Credit: Tracy DeLiberty)*

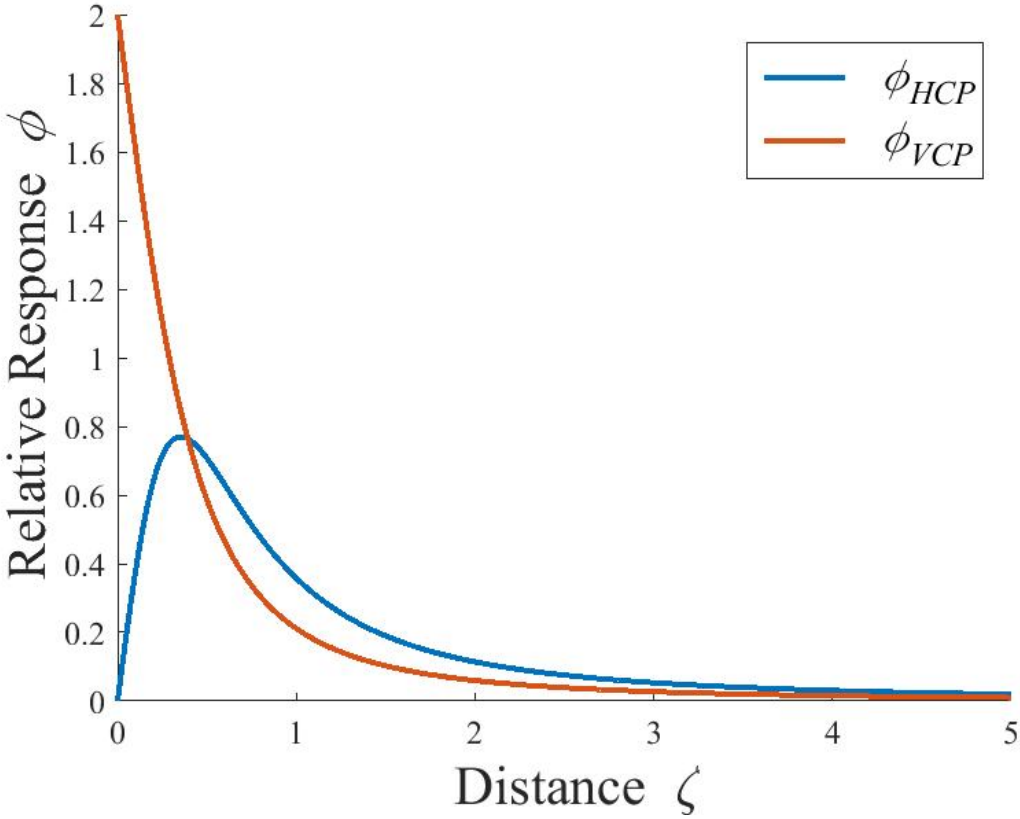

Figure 2-4. Relative response curves. The curves in this figure are a graphical representation of Equation 2.3 for the HCP case and Equation 2.5 for the VCP case. The HCP case allows for greater depth of exploration since the relative contribution from near-surface material is large, and the VCP case is more appropriate for shallower applications since the relative contribution at the surface is very small [6].

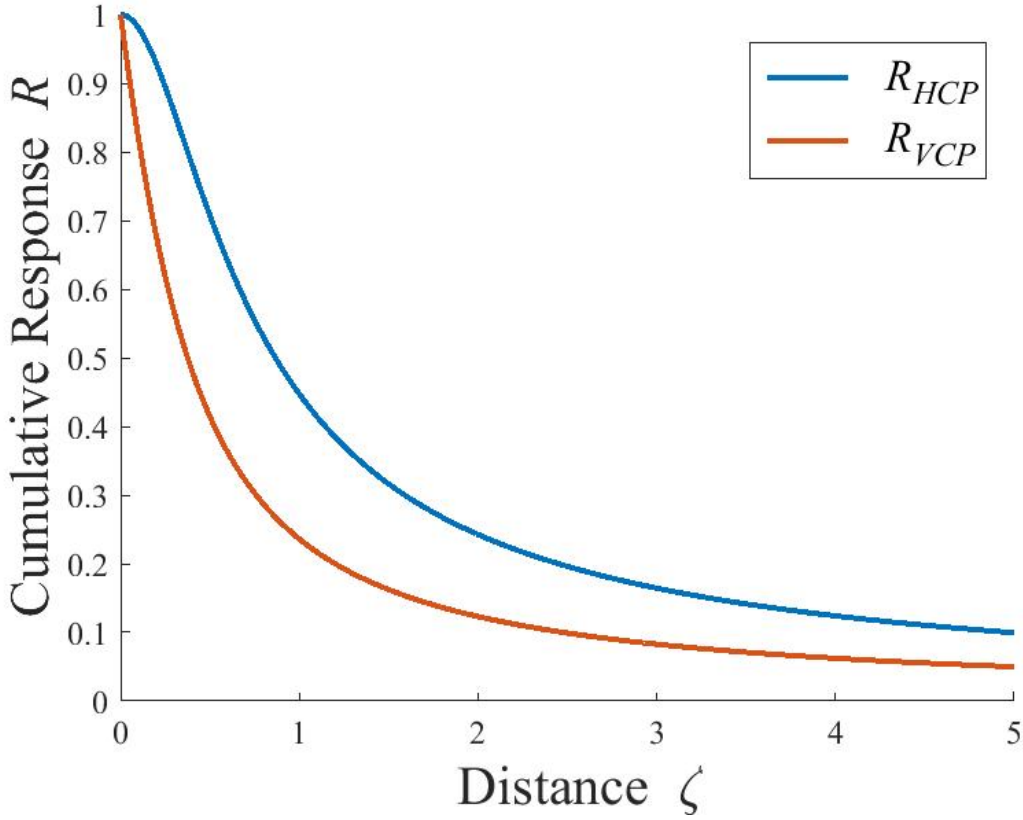

Figure 2-5. Cumulative response curves. The curves in this figure are a graphical representation of Equation 2.7 for the HCP case and Equation 2.8 for the VCP case. This figure demonstrates the difference in responses from all material below an EM inductive instrument based on dipole configuration.

2.4 Disadvantages of Using EM Low Induction Number Techniques

This section will discusses two weaknesses that surround using EM induction instruments at low induction numbers as they apply to a sea ice environment: the accuracy with current methods used for a.) modeling sea ice environments, and b.) processing ice thickness results from field measurements.

2.4.1 Accuracy Concerns with Modeling Sea Ice Environments

The shortcoming in accuracy with modeling sea ice environments lies in the specific problems found in approximations to the layered-earth model related to the instruments that use the EM induction technique at low-conduction numbers for geophysical applications. As mentioned in the previous chapter, current modeling techniques make approximations to the layered-earth model [28]. Two critical assumptions for these approximations are 1) all layers are level and 2) conductivity values are uniform for the material within each layer. These assumptions include negligible conductivity for air/snow/ice layers given an approximated conductivity (~2 S/m) for the ocean. From [29], these assumptions can then be cast into semi-analytic formulae for the layered Earth problem, which are inversion based on the distance between the antenna and the ice/ocean interface. The specific thickness solution is rendered through digital filter techniques [30] based on Hankel transforms [31]. However, for sea ice geophysical conditions, the assumptions of lateral homogeneity through the idealized model aforementioned are proving to be inaccurate in the presence of major physiographic features such as ice rafting, ridges, and cracks.

2.4.2 Accuracy Concerns with Processing Ice Thickness Results

The same issue of accuracy, in regard to processing the thickness results, can be stated with EM induction instruments when the collected data is used against a calibration routine to determine actual ice thickness. One method to determine thickness from received apparent conductivity is through a non-linear regression approach [32-35]. Thickness data collected at drill holes serve a calibration point of measured thickness to the EM induction instrument's reading of apparent conductivity. Multiple drill holes, drilled to the water line, are needed in order to

provide data points to construct thickness relationships. Since this approach provides an apparent conductivity/thickness relationship, any data point collected on survey lines in field campaigns can be matched to a total thickness through an exponential fit curve. However, there are several drawbacks to this approach. First, the calibration curve method relies on coefficients to "fit" the curve to the data, and these coefficients have no geophysical meaning. Second, the curve is solely based on apparent conductivity collected at the drill hole location, but does not account for physiographic features underneath the surface of the ice. Third, the curve is only valid for one instrument and its characteristics, such as coil spacing and operating frequency. Should any of these characteristics change, a new calibration curve must be generated. Finally, the curve is generated based on collected apparent conductivity values alone, without accounting for calculated material conductivity values of the individual layers of sea ice and seawater.

To determine how accurate ice thickness calculations are with these types of processing routines one must calculate error propagation or uncertainty. Outside of using measured ice thickness values collected at drill hole sites, the apparent conductivity/thickness relationship values are calculated values based on field measurements, where uncertainty (or error) is an inherent part of the measurement process. To calculate the uncertainty, the following formula is used [36]:

$$\Delta_{error} = \overline{x} \pm t * \left(\frac{s}{\sqrt{n}} \right) \tag{2.9}$$

where $\overline{x}$ is the sample mean, t is the t-distribution, s is the sample standard deviation, and n is the number of samples (valid values of material conductivities). The t-distribution is based on the 95% confidence interval and n-1 degrees of freedom.

Therefore, the results calculated with this metric provide a useful gauge on how accurate a method is for determining calculated ice thickness values.

2.5 Chapter Summary

This chapter expressed four key points necessary for this research. First, it presented a brief historical note on how EM induction units became involved with the study of sea ice thickness, and also introduced alternative methods to EM induction used in the study of sea ice. Second, a description of how the EM induction process works on sea ice at a conceptual level was also discussed. Third, the concept of response functions and how they relate to physical parameters of sea ice was also presented. Additionally, terms in that section were defined that will be used throughout this dissertation. Defining these terms was necessary in this context since the terminology of the classical literature in this field, at times, can be somewhat confusing to the reader. Lastly, this chapter also examined weaknesses of EM induction with low inductive materials like that of sea ice, specifically on the issues with accuracy with regard to modeling sea ice environments and processing thickness data. The degree of accuracy with models and measurements is based on calculating the uncertainty or error of propagation. Even though some of the methods discussed in this chapter provide accurate results, some assumptions (i.e., negligible ice conductivity) are made that can skew these results. But before these concerns can be addressed, a mathematical premise to this dissertation is presented in the next chapter to provide the background derivations to the formulas used in this research.

Chapter 3

MATHEMATICAL BACKGROUND

This chapter provides the necessary mathematical premise to the objectives discussed in Chapter 1. It does so by presenting a key aspect of electromagnetic theory, that of Maxwell's equations. Some mathematical material was briefly introduced in Chapter 2, but this chapter goes more in depth to describe where the resulting equations are derived from. Therefore, the first section of this chapter presents a review of Maxwell's equations and how they relate to the historical definition of apparent conductivity as discussed in [6]. The second section relates Maxwell's equations to the numerical simulator presented and discussed in Chapter 4. The third section relates Maxwell's equations to the relative and cumulative response functions needed for developing a co-calibration algorithm discussed in Chapter 5. The goal of this chapter is to align the objectives of this dissertation back to Maxwell's equations, in the form of historical geophysical texts [37-39]. Therefore, while the contents of this chapter may be found throughout graduate textbooks and other references stated within this chapter, this chapter takes that information and presents it relative to the focus of this thesis work.

3.1 Relating EM Induction Concepts to Maxwell's Equations

This section introduces Maxwell's equations in both differential and integral form. It also discusses how to uncouple Maxwell's equations, a step that is necessary to derive other equations needed in this dissertation. Vector potentials are also

presented since they relate to such concepts as defining the historical equation for apparent conductivity. Finally, this section also looks into the derivation of HCP and VCP modes for EM induction units of the magnetic dipole type.

3.1.1 Maxwell's Equations to Vector Potentials and Beyond

Referring to Figure 2-1 and based on the historical definition from [6], apparent conductivity (σ_a) can be defined mathematically as

$$\sigma_a = \frac{4}{\omega \mu_0 r^2}\left(\frac{H_s}{H_p}\right) \tag{3.1}$$

where ω is the angular frequency defined by Equation 2.2, μ_0 is the permeability of free space, r is the coil spacing between the transmitter and receiver of the inductive instrument, H_s is the secondary magnetic field, and H_p is the primary magnetic field. However, recall that there are two orientations for electromagnetic induction instruments, and two approaches for HCP and VCP are used herein to derive and define apparent conductivity. Since the equation in [6] for apparent conductivity is based on a homogeneous earth, a comment must be made here to detail the complexity of arriving at Equation 3.1 from first principles in the forthcoming discussion involving Maxwell's equations. From [38] and [37], respectively, there are two approaches, one using Sommerfeld integrals and Bessel functions [38], and the other approach from [37] uses the aforementioned functions, plus Fourier transform pairs and Green's functions. While the latter is more complicated, it is the most complete form, and will be presented here in this chapter, but only relevant equations to achieve the result of Equation 3.1 from both a VCP and HCP perspective.

To start from first principles, Chapter 1 states that the use of EM induction is related to electromagnetics, and so, it is shown here now that Equation 3.1 can be

derived from Maxwell's equations. It should be noted that separate mathematical relations will be provided in later chapters and appendices of this dissertation based on the concepts presented in each particular chapter. This chapter presents the "base" equations needed for this research. With that, Maxwell's equations are introduced, as defined in [31] and shown in Table 3-1. The field quantity terms, including the instantaneous (i.e., time-varying) field vectors, are defined in Table 3-2.

Differential Form	Integral Form
$\nabla \times \boldsymbol{E} = -\boldsymbol{M}_i - \frac{\partial \boldsymbol{B}}{\partial t}$	$\oint_C \boldsymbol{E} \cdot d\mathbf{l} = -\iint_S \boldsymbol{M}_i \cdot d\mathbf{s} - \frac{\partial}{\partial t}\iint_S \boldsymbol{B} \cdot d\mathbf{s}$
$\nabla \times \boldsymbol{H} = \boldsymbol{J}_i + \boldsymbol{J}_c + \frac{\partial \boldsymbol{D}}{\partial t}$	$\oint_C \boldsymbol{H} \cdot d\mathbf{l} = \iint_S \boldsymbol{J}_i \cdot d\mathbf{s} + \iint_S \boldsymbol{J}_c \cdot d\mathbf{s} + \frac{\partial}{\partial t}\iint_S \boldsymbol{D} \cdot d\mathbf{s}$
$\nabla \cdot \boldsymbol{D} = q_{ev}$	$\oiint_S \boldsymbol{D} \cdot d\mathbf{s} = Q_e$
$\nabla \cdot \boldsymbol{B} = q_{mv}$	$\oiint_S \boldsymbol{B} \cdot d\mathbf{s} = Q_m$
$\nabla \cdot \boldsymbol{J}_{ic} = -\frac{\partial q_{ev}}{\partial t}$	$\oiint_S \boldsymbol{J}_{ic} \cdot d\mathbf{s} = -\frac{\partial Q_e}{\partial t}$

Table 3-1. Maxwell's equations in differential and integral forms.

Field Quantity Term	Definition	Units
$\boldsymbol{E}$	Electric field intensity	volts/meter
$\boldsymbol{M_i}$	Impressed (source) magnetic current density	volts/square meter
$\boldsymbol{B}$	Magnetic flux density	webers/square meter or teslas
$\boldsymbol{H}$	Magnetic field intensity	amperes/meter
$\boldsymbol{J_i}$	Impressed (source) electric current density	amperes/square meter
$\boldsymbol{J_c}$	Conduction electric current density	amperes/square meter
$\boldsymbol{J_{ic}}$	The sum of $\boldsymbol{J_i}$ and $\boldsymbol{J_c}$	amperes/square meter
$\boldsymbol{D}$	Electric flux density	coulombs/square meter
q_{ev}	Electric charge density	coulombs/cubic meter
q_{mv}	Magnetic charge density	webers/cubic meter
Q_e	Total electric charge	coulombs
Q_m	Total magnetic charge	webers
j	Imaginary term	$\sqrt{-1}$

Table 3-2. Field quantity terms used in Maxwell's equations. Boldface italic font denotes instantaneous field vectors.

For the sake of completeness, the electromagnetic constitutive relationships are also presented. When materials are subjected to electromagnetic fields, charged particles within the material interact with the electromagnetic vector fields, in turn producing currents and affecting wave propagation in the material [31]. To account for these effects, and relating them to the electromagnetic vectors, these relationships can be mathematically expressed as

$$\boldsymbol{J}_c = \sigma \boldsymbol{E} \tag{3.2}$$

$$\boldsymbol{D} = \varepsilon \boldsymbol{E} \tag{3.3}$$

$$\boldsymbol{B} = \mu \boldsymbol{H}\ , \tag{3.4}$$

where ε is the permittivity of the medium (farads/meter), and μ is the permeability of the medium.

Note that Maxwell's equations are coupled equations. Having coupled equations means that each equation in a set depends on the other. To demonstrate how these equations are coupled, consider the first two equations in Table 3-1, Faraday's law and Ampere's law, respectively. To solve for the vector fields $\boldsymbol{E}$ and $\boldsymbol{H}$, it is necessary to uncouple these equations by increasing their order from first-order partial differential equations to second-order partial differential equations [31]. In order to put these equations into an uncoupled second-order differential equation form, the curl of both sides Faraday's law and Ampere's law, respectively, is taken in differential form, stated as

$$\nabla \times \nabla \times \boldsymbol{E} = -\nabla \times \boldsymbol{M}_i - \mu \nabla \times \left(\frac{\partial \boldsymbol{H}}{\partial t} \right) = -\nabla \times \boldsymbol{M}_i - \mu \frac{\partial}{\partial t} (\nabla \times \boldsymbol{H}) \tag{3.5}$$

$$\nabla \times \nabla \times \boldsymbol{H} = \nabla \times \boldsymbol{J}_i + \sigma \nabla \times \boldsymbol{E} + \varepsilon \nabla \times \left(\frac{\partial \boldsymbol{E}}{\partial t} \right) = \nabla \times \boldsymbol{J}_i + \sigma \nabla \times \boldsymbol{E} + \varepsilon \frac{\partial}{\partial t} (\nabla \times \boldsymbol{E}) \ . \tag{3.6}$$

Using the vector identity

$$\nabla \times \nabla \times \mathbf{V} = \nabla (\nabla \cdot \mathbf{V}) - \nabla^2 \mathbf{V} \ , \tag{3.7}$$

Equation 3.6 can be re-written as

$$\begin{aligned} \nabla (\nabla \cdot \boldsymbol{E}) - \nabla^2 \boldsymbol{E} &= -\nabla \times \boldsymbol{M}_i - \mu \frac{\partial}{\partial t} \left[\boldsymbol{J}_i + \sigma \boldsymbol{E} + \varepsilon \frac{\partial \boldsymbol{E}}{\partial t} \right] \\ &= -\nabla \times \boldsymbol{M}_i - \mu \frac{\partial \boldsymbol{J}_i}{\partial t} - \mu \sigma \frac{\partial \boldsymbol{E}}{\partial t} - \mu \varepsilon \frac{\partial^2 \boldsymbol{E}}{\partial t^2} \end{aligned} \ . \tag{3.8}$$

Another relation from Gauss's law can be stated as

$$\nabla \cdot \boldsymbol{D} = \varepsilon \nabla \cdot \boldsymbol{E} = q_{ev} \ , \tag{3.9}$$

or, equivalently,

$$\nabla \cdot \boldsymbol{E} = \frac{q_{ev}}{\varepsilon} \ . \tag{3.10}$$

Rearranging terms and substituting Equation 3.10 into Equation 3.9, the resultant equation is

$$\nabla^2 \boldsymbol{E} = \nabla \times \boldsymbol{M}_i + \mu \frac{\partial \boldsymbol{J}_i}{\partial t} + \frac{1}{\varepsilon} \nabla q_{ev} + \mu\sigma \frac{\partial \boldsymbol{E}}{\partial t} + \mu\varepsilon \frac{\partial^2 \boldsymbol{E}}{\partial t^2} \quad . \tag{3.11}$$

The same method can be applied to Ampere's law, stated as

$$\begin{aligned} \nabla(\nabla \cdot \boldsymbol{H}) - \nabla^2 \boldsymbol{H} &= \nabla \times \boldsymbol{J}_i + \sigma\left(-\boldsymbol{M}_i - \mu \frac{\partial \boldsymbol{H}}{\partial t}\right) + \varepsilon \frac{\partial}{\partial t}\left(-\boldsymbol{M}_i - \mu \frac{\partial \boldsymbol{H}}{\partial t}\right) \\ &= \nabla \times \boldsymbol{J}_i - \sigma \boldsymbol{M}_i - \mu\sigma \frac{\partial \boldsymbol{H}}{\partial t} - \varepsilon \frac{\partial \boldsymbol{M}_i}{\partial t} - \mu\varepsilon \frac{\partial^2 \boldsymbol{H}}{\partial t^2} \end{aligned} \quad . \tag{3.12}$$

Additionally Gauss's law for magnetism can be expressed as

$$\nabla \cdot \boldsymbol{B} = \mu \nabla \cdot \boldsymbol{H} = q_{mv} \quad , \tag{3.13}$$

or, the equivalent as

$$\nabla \cdot \boldsymbol{H} = \frac{q_{mv}}{\mu} \quad . \tag{3.14}$$

Equation 3.14 can be substituted into 3.12 to receive the following:

$$\nabla^2 \boldsymbol{H} = -\nabla \times \boldsymbol{J}_i + \sigma \boldsymbol{M}_i + \frac{1}{\mu} \nabla q_{mv} + \varepsilon \frac{\partial \boldsymbol{M}_i}{\partial t} + \mu\sigma \frac{\partial \boldsymbol{H}}{\partial t} + \mu\varepsilon \frac{\partial^2 \boldsymbol{H}}{\partial t^2} \quad . \tag{3.15}$$

Relevant to this thesis, these equations can also be expressed in time-harmonic (or frequency domain) form, which requires some explanation. Up until now, the instantaneous field vectors in these equations are assumed to be time-varying (or in the time domain), where each of these quantities has a value defined at every point in space and time. But in many systems involving electromagnetic waves the time variations are cosinusoidal and are referred to as time-harmonic [31]. Time-varying and time-harmonic forms can be related to each other as linear combinations of single-frequency solutions through the use of Fourier transform pairs [40]. This transform pair is expressed as [41]

$$\mathcal{F}\{f(t)\} = \hat{f}(\omega) = \int_{-\infty}^{\infty} f(t) e^{-j\omega t} \, dt \tag{3.16}$$

$$\mathcal{F}^{-1}\{\hat{f}(\omega)\} = f(t) = \frac{1}{2\pi} \int_{-\infty}^{\infty} \hat{f}(\omega) e^{j\omega t} \, d\omega \quad , \tag{3.17}$$

where $\mathcal{F}$ indicates the Fourier transform. Additionally, if expressing equations in time-harmonic form from time-varying, then, in general

$$\frac{\partial}{\partial t} <=> j\omega \ , \tag{3.18}$$

and vice versa. Providing an example here, the electric field intensity can be transformed using an inverse Fourier transform, stated as

$$\boldsymbol{E}(x,y,z;t) = \int_{-\infty}^{\infty} \mathbf{E}(x,y,z;\omega) e^{j\omega t} \frac{d\omega}{2\pi} \ , \tag{3.19}$$

where $e^{j\omega t}$ is the time dependence of the fields [40]. The bold non-italic font of the electric field intensity on the right-hand side of Equation 3.19 denotes time-harmonic form.

To demonstrate the relationship shown in Equation 3.18, as well as using the electric field intensity again, consider as an example the following time-varying field:

$$\boldsymbol{E} = |\boldsymbol{E}| \cos(\omega t + \phi) = \mathrm{Re}\left[\boldsymbol{E}_{ph} e^{j\omega t} \right] \ , \tag{3.20}$$

where

$$\boldsymbol{E}_{ph} = |\boldsymbol{E}| e^{j\phi} \ , \tag{3.21}$$

and represents the phasor field. This result is possible from Euler's identity [42]

$$e^{j\phi} = \cos\phi + j\sin\phi \ . \tag{3.22}$$

Now, if the partial derivative of $\boldsymbol{E}$ in Equation 3.20 is taken with respect to time t, it leads to

$$\frac{\partial \boldsymbol{E}}{\partial t}\left(|\boldsymbol{E}| \cos(\omega t + \phi)\right) = -\omega |\boldsymbol{E}| \sin(\omega t + \phi) \ . \tag{3.23}$$

Equivalently,

$$\frac{\partial \boldsymbol{E}}{\partial t} = \left(\frac{\partial}{\partial t}\right) \mathrm{Re}\left[\boldsymbol{E}_{ph} e^{j\omega t} \right] \tag{3.24}$$

$$\frac{\partial \boldsymbol{E}}{\partial t} = \mathrm{Re}\left[\left(\frac{\partial}{\partial t}\right)\boldsymbol{E}_{ph}e^{j\omega t}\right] \tag{3.25}$$

$$\frac{\partial \boldsymbol{E}}{\partial t} = \mathrm{Re}\left[j\omega \boldsymbol{E}_{ph}e^{j\omega t}\right] = j\omega\,\mathrm{Re}\left[\boldsymbol{E}_{ph}e^{j\omega t}\right] \ , \tag{3.26}$$

and Equation 3.18 can generally be used.

Unless otherwise indicated, the following equations will use time-harmonic form, and the vector quantities will be in bold non-italic font. Therefore, Equations 3.11 and 3.15 can be rewritten as

$$\nabla^2\mathbf{E} = \nabla\times\mathbf{M}_\mathbf{i} + j\omega\mu\mathbf{J}_\mathbf{i} + \frac{1}{\varepsilon}\nabla q_{ev} + j\omega\mu\sigma\mathbf{E} + \omega^2\mu\varepsilon\mathbf{E} \tag{3.27}$$

$$\nabla^2\mathbf{H} = -\nabla\times\mathbf{J}_\mathbf{i} + \sigma\mathbf{M}_\mathbf{i} + \frac{1}{\mu}\nabla q_{mv} + j\omega\varepsilon\mathbf{M}_\mathbf{i} + j\omega\mu\sigma\mathbf{H} + \omega^2\mu\varepsilon\mathbf{H} \ . \tag{3.28}$$

In trying to relate the previous equations to the historical definition of apparent conductivity as shown in Equation 3.1, it is useful to explain an important concept, that of Schelkunoff potentials [39]. Schelkunoff potentials define the electromagnetic field by pairs of vector functions to a superposition of sources of electric type and magnetic type, and are used to solve wave equations in a space comprised of homogenous regions [37]. Schelkunoff potentials also use the concept of vector potentials from electromagnetic theory, where vector potentials in electromagnetics are used as aids in obtaining solutions for the electric and magnetic fields. The introduction of vector potentials often simplifies the solution, even though it may require the determination of additional functions. This process generally requires two steps: the first step, the vector potentials defined as magnetic (**A**) and electric (**F**), are found once the specific boundary-value problem is specified, and the second step quantifies the electric and magnetic fields after the vector potentials are determined.

In order to begin the discussion of Schelkunoff potentials in a mathematical sense, the following equations are used:

$$\mathbf{E} = \mathbf{E}_m + \mathbf{E}_e \tag{3.29}$$

$$\mathbf{H} = \mathbf{H}_m + \mathbf{H}_e \ , \tag{3.30}$$

where $\mathbf{E}_m$ is the electric field intensity produced by magnetic currents, $\mathbf{E}_e$ is the electric field intensity produced by electric currents, $\mathbf{H}_m$ is the magnetic field intensity produced by magnetic currents, and $\mathbf{H}_e$ is the magnetic field intensity produced by electric currents. Since the end goal is to ultimately derive to Equation 3.1, the focus here will be on using $\mathbf{E}_m$ and $\mathbf{H}_m$. To start here, the Schelkunoff potential $\mathbf{F}$ can be used in the following manner,

$$\mathbf{E}_m = -\nabla \times \mathbf{F} \ . \tag{3.31}$$

Additionally, it is also necessary to introduce the term ϕ_m, which is an arbitrary magnetic scalar potential [31]. This term is introduced since the equality of the curls of two vectors does not require that the vectors be identical [37]. Using this arbitrary scalar potential, where the following vector identity can be used:

$$\nabla \times \left(-\nabla \phi_m\right) = 0 \ . \tag{3.32}$$

To see how the Schelkunoff vector potential $\mathbf{F}$ and ϕ_m can be used, Ampere's law with $\mathbf{E}_m$ and $\mathbf{H}_m$ terms are used in time-harmonic form, stated as

$$\nabla \times \mathbf{H}_m = \mathbf{J}_i + \sigma \mathbf{E}_m + j\omega\varepsilon \mathbf{E}_m \, . \tag{3.33}$$

Assuming for now a source-free region (i.e., $\mathbf{J}_i = 0$), equation 3.33 can be rewritten as

$$\nabla \times \mathbf{H}_m = \left(\sigma + j\omega\varepsilon\right)\mathbf{E}_m \tag{3.34}$$

where subtracting terms leads to

$$\nabla \times \mathbf{H}_m - \left(\sigma + j\omega\varepsilon\right)\mathbf{E}_m = 0 \ , \tag{3.35}$$

where the quantity of $\sigma + j\omega\varepsilon$ is referred to as admittivity [43]. Admittivity is defined as the admittance per unit length [43], where admittance is a measure of electrical conduction in a system. Admittance can also be described as how well current flows in

a circuit from circuit theory [44]. But also note the quantity of $\sigma + j\omega\varepsilon$. The real component σ is referred to be "in-phase" with the electric field intensity. The imaginary component $j\omega\varepsilon$ is referred to be in "quadrature" with the electric field intensity for real ε [37].

Equation 3.31 can then be substituted into Equation 3.35 to receive the following:

$$\nabla \times \mathbf{H}_m - (\sigma + j\omega\varepsilon)(-\nabla \times \mathbf{F}), \tag{3.36}$$

where, by factoring out the minus signs leads to

$$\nabla \times \mathbf{H}_m + (\sigma + j\omega\varepsilon)(\nabla \times \mathbf{F}) \ . \tag{3.37}$$

Using the vector identity

$$\nabla \times \mathbf{A} + \nabla \times \mathbf{B} = \nabla \times (\mathbf{A} + \mathbf{B}) \ , \tag{3.38}$$

Equation 3.37 can now be restated as

$$\nabla \times (\mathbf{H}_m + (\sigma + j\omega\varepsilon)\mathbf{F}) = 0 \ . \tag{3.39}$$

Invoking the vector identity established in equation 3.32, such that

$$(\mathbf{H}_m + (\sigma + j\omega\varepsilon)\mathbf{F}) = -\nabla\phi_m \ , \tag{3.40}$$

solving for $\mathbf{H}_m$ leads to

$$\mathbf{H}_m = -\nabla\phi_m - (\sigma + j\omega\varepsilon)\mathbf{F} \ . \tag{3.41}$$

Substituting Equation 3.41 into Faraday's law, complete with the source term $\mathbf{M}_i$, leads to the following:

$$\nabla \times \mathbf{E}_m = -\mathbf{M}_i - j\omega\mu\mathbf{H}_m \tag{3.42}$$

$$\nabla \times \mathbf{E}_m = -\mathbf{M}_i - (j\omega\mu)(-\nabla\phi_m - (\sigma + j\omega\varepsilon)\mathbf{F}) \ , \tag{3.43}$$

where the quantity $j\mu\omega$ is referred to as the impedivity [43]. Impedivity is defined as impedance per unit length [43], where physically, impedance is, the measure of current flow impediment in a circuit (from circuit theory) [44]. When the curl-curl of

the vector potential **F** is used with Equation 3.41, the following relationship can be stated

$$\nabla \times \nabla \times \mathbf{F} = \mathbf{M}_i - (\sigma + j\omega\varepsilon)(j\omega\mu) - (j\omega\mu)\nabla\phi_m \ . \tag{3.44}$$

Using the vector identity established in Equation 3.7, and applying to the left-hand side of Equation 3.44 leads to

$$\nabla(\nabla \cdot \mathbf{F}) - \nabla^2\mathbf{F} = \mathbf{M}_i - (\sigma + j\omega\varepsilon)(j\omega\mu) - (j\omega\mu)\nabla\phi_m \ . \tag{3.45}$$

Since the term ϕ_m is arbitrarily defined, the divergence of **F** can also be defined, such that

$$\nabla \cdot \mathbf{F} = -(j\mu\omega)\phi_m \ . \tag{3.46}$$

Called the Lorenz gauge, Equation 3.46 allows the inhomogeneous wave equation, also referred to as the Helmholtz equation or complex wave equation, to be expressed as

$$\nabla^2\mathbf{F} + k^2\mathbf{F} = -\mathbf{M}_i \ , \tag{3.47}$$

where k, the wavenumber, is defined as

$$k^2 = \mu\varepsilon\omega^2 - j\mu\sigma\omega \ . \tag{3.48}$$

3.1.2 HCP Configuration

To begin with the HCP derivation, a general case of a source-free region is presented first. The following equation is introduced here:

$$\mathbf{F} = F\mathbf{u}_z \ , \tag{3.49}$$

where $\mathbf{u}_z$ is the unit vector in the z-direction. Equation 3.49 is known as the transverse electric (TE) vector potential. This equation is possible due to Equation 3.31 and the fact that, in a source-free region, the vector potential **F** due to magnetic sources does not need to be considered [43, 37]. Hence, a source-free Helmholtz wave equation using scalar potentials can now be written as

$$\nabla^2 \mathbf{F} + k^2 \mathbf{F} = 0 \ . \tag{3.50}$$

Equation 3.50 can be converted into an ordinary differential equation by way of a double Fourier transform pair that looks like

$$\tilde{F}\left(k_x, k_y, z\right) = \int_{-\infty}^{\infty}\int_{-\infty}^{\infty} F\left(x, y, z\right) e^{-j(k_x x + k_y y)}\, dx\, dy \tag{3.51}$$

$$F\left(x, y, z\right) = \frac{1}{4\pi^2}\int_{-\infty}^{\infty}\int_{-\infty}^{\infty} \tilde{F}\left(k_x, k_y, z\right) e^{j(k_x x + k_y y)}\, dk_x\, dk_y \ . \tag{3.52}$$

The resulting ordinary differential equation is then

$$\frac{d^2 \tilde{F}}{dz^2} - u^2 \tilde{F} = 0 \ , \tag{3.53}$$

where u is defined as

$$u = \sqrt{k_x^2 + k_y^2 + k^2} \ . \tag{3.54}$$

The solution to Equation 3.53 is

$$\tilde{F}\left(k_x, k_y, z\right) = F^{+}\left(k_x, k_y\right) e^{-uz} + F^{-}\left(k_x, k_y\right) e^{+uz} \ , \tag{3.55}$$

where $\tilde{F}$ is the Fourier transformed TE potential, and the "+" and "–" symbols represent downward and upward attenuations (decaying) waves [37].

In an N-layered system, the decaying solutions, both upward (F^{+}) and downward (F^{-}), can be determined by incorporating a particular solution F_p. The particular solution is defined as the sum of any possible solution [43], therefore in this case it represents both F^{+} and F^{-}. Since there will now be a source present with both VCP and HCP cases in a homogeneous earth, these source terms, along with the particular solution F_p, are accounted for now in the following equations. For the HCP configuration, the solution between the source and the earth's surface can be expressed in Fourier transform space as

$$\tilde{F} = F_p e^{-u_0 h}\left(e^{-u_0 z} + r_{TE} e^{+u_0 z}\right) \tag{3.56}$$

where, if some terms are rearranged such that the exponential is inside the parenthesis, results in

$$\tilde{F} = F_p\left(e^{-u_0(h+z)} + r_{TE}e^{+u_0(h+z)}\right) , \tag{3.57}$$

where F_p represents the particular solution between the source and the earth (as well as the decaying solutions aforementioned), u_0 is u but the subscript of 0 indicates the zeroth layer (i.e., the surface), h represents the carry height of the EM induction instrument, z represents the thickness of the layers, and r_{TE} is the reflection coefficient for the TE mode.

To derive individual field components for a homogeneous earth set, the field components of a layered system are expressed first since some terms will go to zero in the homogenous set case. Therefore, for this case in transform space,

$$\tilde{F} = \frac{j\omega\mu_0 m}{2u_0}e^{-u_0 h}e^{-u_0 z} , \tag{3.58}$$

where

$$F_p = \frac{j\omega\mu_0 m}{2u_0} . \tag{3.59}$$

Additionally, m represents the infinitesimal magnetic dipole moment [37] and is expressed mathematically as

$$m = IS \tag{3.60}$$

where I is a small loop of current at the origin and S is the area of the loop. Recall then Equation 3.56, and substituting that into Equation 3.52 results in the following equation

$$F = \frac{1}{4\pi^2}\int_{-\infty}^{\infty}\int_{-\infty}^{\infty} F_p e^{-u_0 h}\left(e^{-u_0 z} + r_{TE}e^{+u_0 z}\right)e^{j(k_x x + k_y y)}\, dk_x\, dk_y , \tag{3.61}$$

where now Equation 3.59 can also be substituted into Equation 3.61 to receive the following result of

$$F(x,y,z)=\frac{j\omega\mu_0 m}{8\pi^2}\int_{-\infty}^{\infty}\int_{-\infty}^{\infty}\left(e^{-u_0(z+h)}+r_{TE}e^{+u_0(z-h)}\right)\frac{1}{u_0}e^{j(k_x x+k_y y)}\,dk_x\,dk_y \quad . \tag{3.62}$$

Since the integral is a function of $k_x^2+k_y^2$ because of the u_0 term, the double Fourier transform can be converted to a Hankel transform using the relation described in [45]

$$\int_{-\infty}^{\infty}\int_{-\infty}^{\infty}F\left(k_x^2+k_y^2\right)e^{j(k_x x+k_y y)}\,dk_x\,dk_y=2\pi\int_0^{\infty}F(\lambda)\lambda J_0(\lambda\rho)\,d\lambda \quad , \tag{3.63}$$

where

$$\lambda^2=k_x^2+k_y^2 \quad , \tag{3.64}$$

J_0 is the Bessel function of order 0, and

$$\rho^2=x^2+y^2 \quad . \tag{3.65}$$

With this transform, Equation 3.62 can be recast into

$$F(\rho,z)=\frac{j\omega\mu_0 m}{4\pi}\int_0^{\infty}\left(e^{-u_0(z+h)}+r_{TE}e^{+u_0(z-h)}\right)\frac{\lambda}{u_0}J_0(\lambda\rho)\,d\lambda \quad , \tag{3.66}$$

where

$$u_0=\sqrt{\left(\lambda^2-k_0^2\right)} \quad . \tag{3.67}$$

Since cylindrical coordinates are being used, due to symmetry there will only be a ϕ component in the electric field

$$E_\phi=-\frac{j\omega\mu_0 m}{4\pi}\int_0^{\infty}\left(e^{-u_0(z+h)}+r_{TE}e^{+u_0(z-h)}\right)\frac{\lambda^2}{u_0}J_1(\lambda\rho)\,d\lambda \quad , \tag{3.68}$$

which is possible through the relations of [37]

$$E_\phi=-\frac{y}{\rho}E_x+\frac{x}{\rho}E_y \tag{3.69}$$

and

$$\frac{\partial J_0(\lambda\rho)}{\partial x}=-\lambda\frac{x}{\rho}J_1(\lambda\rho) \quad , \tag{3.70}$$

where J_1 is the Bessel function of order 1. Using the same approach, the horizontal magnetic field will only have a ρ (or radial) component, which can be expressed as [37]

$$H_\rho = \frac{x}{\rho} H_x + \frac{y}{\rho} H_y \ , \tag{3.71}$$

and in integral form

$$H_\rho = \frac{m}{4\pi} \int_0^\infty \left(e^{-u_0(z+h)} + r_{TE} e^{+u_0(z-h)} \right) \lambda^2 J_1(\lambda\rho) d\lambda \ . \tag{3.72}$$

Lastly, the vertical magnetic field can be given by the relation [37]

$$\frac{\partial^2}{\partial z^2} + k_0^2 = u_0^2 + k_0^2 = \lambda^2 \ , \tag{3.73}$$

and in integral form

$$H_z = \frac{m}{4\pi} \int_0^\infty \left(e^{-u_0(z+h)} + r_{TE} e^{+u_0(z-h)} \right) \frac{\lambda^3}{u_0} J_0(\lambda\rho) d\lambda \ . \tag{3.74}$$

Now since Equation 3.1, as shown in [6], is only concerned with a homogenous earth, all z and h terms in Equations 3.68, 3.72, and 3.74 are set to zero. In order to derive the vertical magnetic field, the electric field is defined first, as

$$E_\phi = -\frac{j\omega\mu_0 m}{2\pi} \int_0^\infty \frac{\lambda^2}{\lambda + u} J_1(\lambda\rho) d\lambda \ . \tag{3.75}$$

Equation 3.75 can also be transformed with the following approach from [37]. First, since

$$k^2 = \lambda^2 - u^2 \ , \tag{3.76}$$

and multiplying the numerator and denominator of the integrand by $\lambda - u$, Equation 3.75 can be restated as

$$E_\phi = \frac{j\omega\mu_0 m}{2\pi k^2} \frac{\partial}{\partial\rho} \left[\int_0^\infty \lambda^2 J_0(\lambda\rho) d\lambda - \int_0^\infty \lambda u J_0(\lambda\rho) d\lambda \right] . \tag{3.77}$$

Using the Lipschitz integral relation [46]

$$\int_0^\infty e^{-\lambda z} J_0(\lambda\rho)\, d\lambda = \frac{1}{r} \ , \tag{3.78}$$

where

$$r = \sqrt{\rho^2 + z^2} \ , \tag{3.79}$$

while including the Sommerfeld integral relation [47]

$$G(\rho, z) = \frac{1}{4\pi} \int_0^\infty \frac{\lambda}{u} e^{-u|z|} J_0(\lambda\rho)\, d\lambda \ , \tag{3.80}$$

and, using the following from [48]

$$G(r) = \frac{e^{-jkr}}{4\pi r} \ , \tag{3.81}$$

where G is the three-dimensional scalar electromagnetic Green's function, the relation of

$$\int_0^\infty \frac{\lambda}{u} e^{-uz} J_0(\lambda\rho)\, d\lambda = \frac{e^{-jkr}}{r} \ , \tag{3.82}$$

can be applied to the electric field, such that

$$E_\phi = -\frac{m}{2\pi\sigma} \frac{\partial}{\partial\rho} \left[\frac{\partial^2}{\partial z^2}\left(\frac{1}{r}\right) - \frac{\partial^2}{\partial z^2}\left(\frac{e^{-jkr}}{r}\right) \right]_{z=0} \ , \tag{3.83}$$

where finally

$$E_\phi = -\frac{m}{2\pi\sigma\rho^4} \left[3 - \left(3 + 3ik\rho - k^2\rho^2\right) e^{-jk\rho} \right] \ . \tag{3.84}$$

Then the vertical magnetic field can be derived from Faraday's law and expressed as [37]

$$H_z = -\frac{1}{j\omega\mu_0} \frac{1}{\rho} \frac{\partial}{\partial\rho}\left(\rho E_\phi\right) \ , \tag{3.85}$$

with the final result being

$$H_z = \frac{m}{2\pi k^2 \rho^5} \left[9 - \left(9 + 9jk\rho - 4k^2\rho^2 - jk^3\rho^3\right) e^{-jk\rho} \right] \ . \tag{3.86}$$

H_z can also be expressed in mutual impedance ratios, Z/Z_0, where Z is the mutual impedance of small loops at the surface, and Z_0 is the mutual impedance of the same loops albeit in free space. The ratios are obtained by dividing H_z by the fields measured in free space ($-m/4\pi\rho^3$), which results in the following for HCP

$$Z / Z_0 = \frac{2}{k^2\rho^2}\left[-9 + \left(9 + 9jk\rho - 4k^2\rho^2 - jk^3\rho^3\right)e^{-jk\rho}\right] \ . \tag{3.87}$$

3.1.3 VCP Configuration

Now, for VCP, the approach is similar, but the equations naturally change because of the different orientation. The Fourier transformed TE potential is now

$$\tilde{F} = \frac{j\omega\mu_0 m}{2u_0} e^{-u_0(z+h)}\mathbf{u}_x \ . \tag{3.88}$$

F_p is obtained by equating the vertical magnetic field in Fourier transform space

$$\tilde{H}_z^p = \frac{1}{j\omega\mu_0}\frac{\partial^2 \tilde{F}_x}{\partial x \partial z} = -jk_x \frac{m}{2} e^{-u_0(z+h)} \tag{3.89}$$

with

$$H_z = \frac{1}{j\omega\mu_0}\left(\frac{\partial^2}{\partial z^2} + k^2\right)F_z \tag{3.90}$$

to receive

$$F_p = -\frac{j\omega\mu_0 m}{2}\frac{jk_x}{k_x^2 + k_y^2} \ . \tag{3.91}$$

Substituting Equation 3.91 into Equation 3.61 produces the following relationship

$$F(x,y,z) = -\frac{j\omega\mu_0 m}{8\pi^2}\int_{-\infty}^{\infty}\int_{-\infty}^{\infty}\left(e^{-u_0(z+h)} + r_{TE}e^{+u_0(z-h)}\right)\frac{jk_x}{k_x^2 + k_y^2}e^{j(k_x x + k_y y)}\,dk_x\,dk_y \ , \tag{3.92}$$

where, from Equation 3.63, can be converted from a Fourier to Hankel transform, which results in

$$F(\rho,z) = -\frac{j\omega\mu_0 m}{4\pi}\frac{\partial}{\partial x}\int_0^{\infty}\left(e^{-u_0(z+h)} + r_{TE}e^{+u_0(z-h)}\right)\frac{1}{\lambda}J_0(\lambda\rho)\,d\lambda \ . \tag{3.93}$$

When the derivatives of Equation 3.93 are taken by the following formulas

$$H_x = \frac{1}{j\omega\mu}\frac{\partial^2 F_z}{\partial x \partial z} \tag{3.94}$$

$$H_y = \frac{1}{j\omega\mu}\frac{\partial^2 F_z}{\partial y \partial z} \ , \tag{3.95}$$

and Equation 3.90, the resulting magnetic field components are

$$H_x = \frac{m}{4\pi}\frac{\partial^2}{\partial x^2}\int_0^\infty \left(e^{-\lambda(z+h)} + r_{TE}e^{+\lambda(z-h)}\right)J_0(\lambda\rho)\,d\lambda \tag{3.96}$$

$$H_y = \frac{m}{4\pi}\frac{\partial^2}{\partial x \partial y}\int_0^\infty \left(e^{-\lambda(z+h)} + r_{TE}e^{+\lambda(z-h)}\right)J_0(\lambda\rho)\,d\lambda \tag{3.97}$$

$$H_z = \frac{m}{4\pi}\frac{\partial}{\partial x}\int_0^\infty \left(e^{-\lambda(z+h)} + r_{TE}e^{+\lambda(z-h)}\right)\lambda J_0(\lambda\rho)\,d\lambda \ . \tag{3.98}$$

Again, since the focus is with a homogenous earth, and since the dipole is horizontally oriented, the focus is on the H_x and H_y components, where now z and h of the H_x and H_y components can be expressed as

$$H_x = -\frac{m}{4\pi}\frac{\partial}{\partial x}\left(\frac{x}{\rho}\Psi\right) \tag{3.99}$$

$$H_y = -\frac{m}{4\pi}\frac{\partial}{\partial y}\left(\frac{x}{\rho}\Psi\right) \ , \tag{3.100}$$

where

$$\Psi = 2\int_0^\infty \frac{\lambda u}{\lambda + u} J_1(\lambda\rho)\,d\lambda \ . \tag{3.101}$$

Further refinements to Equation 3.101 can be made, such as multiplying the numerator and denominator of the integrand by $\lambda - u$ leads to Ψ_{total}, stated as

$$\Psi_{total} = \frac{2}{k^2}\int_0^\infty (\lambda - u)\lambda u J_1(\lambda\rho)\,d\lambda \tag{3.102}$$

Equation 3.102 can be recast in the following form

$$\Psi_{total} = \Psi_1 + \Psi_2 + \Psi_3 \ , \tag{3.103}$$

where

$$\Psi_1 = \frac{2}{k^2}\int_0^\infty \lambda^2 u J_1(\lambda\rho)\,d\lambda \tag{3.104}$$

$$\Psi_2 = -\frac{2}{k^2}\int_0^\infty \lambda^3 J_1(\lambda\rho)\,d\lambda \tag{3.105}$$

$$\Psi_3 = 2\int_0^\infty \lambda J_1(\lambda\rho)\,d\lambda \ . \tag{3.106}$$

Using the Sommerfeld integral relation [47] discussed with Equation 3.82 and the Lipschitz integral relation [46] discussed with Equation 3.78, Equations 3.104-3.106 can be restated as

$$\Psi_1 = \frac{2}{k^2\rho^4}\left(k^2\rho^2 - 3jk\rho - 3\right)e^{-jk\rho} \tag{3.107}$$

$$\Psi_2 = \frac{6}{k^2\rho^4} \tag{3.108}$$

$$\Psi_3 = \frac{2}{\rho^2} \ , \tag{3.109}$$

where, combining terms leads to

$$\Psi_{total} = \frac{2}{k^2\rho^4}\left[3 + k^2\rho^2 - \left(3 + 3jk\rho - k^2\rho^2\right)\right] \ . \tag{3.110}$$

Substituting Equation 3.110 into the horizontal field components of Equations 3.99 and 3.100 leads to

$$H_x = -\frac{m}{4\pi\rho^3}\left[y^2\Psi_{total} + x^2\rho\frac{\partial\Psi_{total}}{d\rho}\right] \tag{3.111}$$

$$H_y = -\frac{m}{4\pi\rho^3}\left[xy\Psi_{total} + xy\rho\frac{\partial\Psi_{total}}{d\rho}\right] , \tag{3.112}$$

where

$$\frac{\partial\Psi_{total}}{\partial\rho} = \frac{2}{k^2\rho^5}\left[-2k^2\rho^2 - 12 + \left(-jk^3\rho^3 - 5k^2\rho^2 + 12jk\rho + 12\right)e^{-jk\rho}\right] \ . \tag{3.113}$$

Putting Equation 3.111 into mutual impedance ratio form, as discussed with Equation 3.87, when $x = 0$, leads to

$$Z / Z_0 = \frac{2}{k^2\rho^2}\left[3 + k^2\rho^2 - \left(3 + 3jk\rho - k^2\rho^2\right)e^{-jk\rho}\right] . \tag{3.114}$$

If the effects of displacement currents are neglected [38], such that k can be recast into the following equation

$$k = \gamma = \sqrt{j\omega\mu_0\sigma} \ , \tag{3.115}$$

and equating the radial components in Equations 3.87 and 3.114 to the coil separation such that $\rho = r$, then Equations 3.87 and 3.114 can be expressed in secondary-to-primary magnetic field ratios as stated in [6]

$$\left(\frac{H_s}{H_p}\right)_{HCP} = \frac{2}{\gamma^2 r^2}\left[-9 + \left(9 + 9j\gamma r - 4\gamma^2 r^2 - j\gamma^3 r^3\right)e^{-j\gamma r}\right] \tag{3.116}$$

$$\left(\frac{H_s}{H_p}\right)_{VCP} = \frac{2}{\gamma^2 r^2}\left[3 + \gamma^2 r^2 - \left(3 + 3j\gamma r - \gamma^2 r^2\right)e^{-j\gamma r}\right] . \tag{3.117}$$

Equations 3.116 and 3.117, coming from mutual impedance ratios per Equations 3.87 and 3.114, can be greatly simplified with the following process per [6]. Taking into account the electrical skin depth as defined in Equation 2.1 and recast here in the following form

$$\delta = \sqrt{\frac{2}{\omega\mu_0\sigma}} = \frac{\sqrt{2j}}{\gamma} \ . \tag{3.118}$$

Equation 3.120 can be restated as

$$\gamma r = \sqrt{2j}\,\frac{r}{\delta} \tag{3.119}$$

where the ratio of r/δ can be expressed as

$$\gamma r = \sqrt{2j}B \tag{3.120}$$

and B is the induction number. If B is much less than unity, the field ratio can reduce to

$$\left(\frac{H_s}{H_p}\right)_{HCP} \simeq \left(\frac{H_s}{H_p}\right)_{VCP} \simeq \frac{jB^2}{2} = \frac{j\omega\mu_0 r^2}{4} \tag{3.121}$$

For B to be less than unity such that it is referred to as a "low-induction number", r must be much less than δ such that

$$\omega \ll \frac{2}{\mu_0 \sigma r^2} \tag{3.122}$$

Therefore, the apparent conductivity to which the instrument reads is defined as Equation 3.1, shown here for completion

$$\sigma_a = \frac{4}{\omega\mu_0 r^2}\left(\frac{H_s}{H_p}\right)_{\substack{quadrature\\component}}, \tag{3.123}$$

where "quadrature" denotes the imaginary component of a signal, whereas the real component is labeled "in-phase" [49, 50].

3.2 Relating Maxwell's Equations to a 3D Full-Physics Heterogeneous Model

Chapter 4 applies a 3D full-physics heterogeneous model to a sea ice environment. This model, termed Project APhiD [51], is a 3D finite-volume discretization of Maxwell's equations, where APhiD stands for magnetic vector potential **A** and electric scalar ϕ ("**Phi**") **D**ecomposition. While Chapter 4 looks at this model in depth, this section derives the matrix equations used in [51] from first principles. Section 3-1 used Maxwell's equations presented in Table 3-1 to derive the equations for apparent conductivity as per Equation 3.1. In that derivation, the concept of auxiliary vector potentials was discussed, but the electric vector potential **F** was used in that section. Since the APhiD model is based on the magnetic vector potential **A** as well as the scalar function ϕ (ϕ_e in this derivation), this section focuses on the

magnetic vector potential **A** and how it is used to derive the background equations for the model. The derivation starts by using Gauss' law for magnetism as expressed in Equation 3.13. However, since the magnetic flux density is solenoidal because magnetic monopoles do not exist, Equation 3.13 can be restated as the following relationship [31]:

$$\nabla \cdot \mathbf{B} = 0 \ . \tag{3.124}$$

Using the vector identity

$$\nabla \cdot \left(\nabla \times \mathbf{A} \right) = 0 \tag{3.125}$$

the magnetic flux density **B** can now be stated as

$$\mathbf{B} = \mu \mathbf{H} = \nabla \times \mathbf{A} \tag{3.126}$$

or, equivalently,

$$\mathbf{H} = \frac{1}{\mu} \nabla \times \mathbf{A} \ . \tag{3.127}$$

To find the electric field at this point, it can be stated from Faraday's law that

$$\nabla \times \mathbf{E} = -j\omega\mu\mathbf{H} \tag{3.128}$$

where, by using Equation 3.126 results in

$$\nabla \times \mathbf{E} = -j\omega\mu\mathbf{H} = -j\omega\nabla \times \mathbf{A} \ . \tag{3.129}$$

Combining terms from Equation 3.129 leads to

$$\nabla \times \left[\mathbf{E} + j\omega\mathbf{A} \right] = 0 \ . \tag{3.130}$$

The vector identity (similar to Equation 3.32) involving an arbitrary electric scalar potential ϕ_e can be stated as

$$\nabla \times \nabla \phi_e = 0 \ , \tag{3.131}$$

which allows

$$\mathbf{E} + j\omega\mathbf{A} = \nabla \phi_e \ , \tag{3.132}$$

or alternatively, by subtracting terms,

$$\mathbf{E} = \nabla\phi_e - j\omega\mathbf{A} \ . \tag{3.133}$$

When the following assumption is made

$$\phi_e = j\omega\phi \ , \tag{3.134}$$

Equation 3.133 can be recast into the following form found in [51] by substituting Equation 3.134 into Equation 3.133 as

$$\mathbf{E} = -j\omega\left(\mathbf{A} - \nabla\phi\right) \ . \tag{3.135}$$

Using the following form of Ampere's law, which is Equation 3.35 with a source term and the admittivity included,

$$\nabla\times\mathbf{H} - \left(\sigma + j\omega\varepsilon\right)\mathbf{E} = \mathbf{J}_i \ , \tag{3.136}$$

Equation 3.135 can also be substituted into Equation 3.136. The substitution leads to the following expression:

$$\nabla\times\mathbf{H} + j\omega\hat{\sigma}\left(\mathbf{A} - \nabla\phi\right) = \mathbf{J}_i \ , \tag{3.137}$$

where

$$\hat{\sigma} = \sigma + j\omega\varepsilon \ . \tag{3.138}$$

Applying Equation 3.127 to Equation 3.137 leads to the following relationship:

$$\nabla\times\nabla\times\mathbf{A} + j\omega\mu_0\hat{\sigma}\left(\mathbf{A} - \nabla\phi\right) = \mu_0\mathbf{J}_i \ , \tag{3.139}$$

When using the vector identity from Equation 3.7, Equation 3.139 can be expressed as

$$-\nabla^2\mathbf{A} + \nabla\left(\nabla\cdot\mathbf{A}\right) + j\omega\mu_0\hat{\sigma}\left(\mathbf{A} - \nabla\phi\right) = \mu_0\mathbf{J}_i \ . \tag{3.140}$$

When the Lorenz gauge, originally introduced with Equation 3.32, but in this case, set to the following

$$\nabla\cdot\mathbf{A} = j\omega\mu_0\hat{\sigma}\phi \ , \tag{3.141}$$

and, assuming that the impedivity is included in the wavenumber k such that

$$\nabla\cdot\mathbf{A} = k^2\phi \ , \tag{3.142}$$

Equation 3.140 can now be expressed as

$$-\nabla^2\mathbf{A}+k^2\mathbf{A}+\nabla\left(k^2\phi\right)-k^2\phi=\mu_0\mathbf{J}_i \ . \tag{3.143}$$

The Lorenz gauge, when compared to other gauges, such as the Coulomb gauge, allows one to uncouple the Helmholtz wave equation (refer to Equation 3.47) such that the scalar and vector potentials can be described as symmetrical equations [52]. Using this gauge paves the way for an alternative formulation that is sparse and symmetric, in matrix form, to allow computation of inhomogeneous structures while maintaining minimum computational resources [51]. As shown, Equation 3.143 is now a set of three scalar equations with four unknowns, where another equation is needed to complete the system. Per [51], Equation 3.137 implies that the divergence of **J** (i.e., the total electric current density $\mathbf{J}_{ic}$ from Table 3-2) to be zero, but that condition is lost in Equation 3.143. However, the following equation allows the recovery of the total current density from taking the divergence of Equation 3.139 and substituting in Equation 3.142, stated as [51]

$$\nabla\cdot\left[k^2\left(\mathbf{A}-\nabla\phi\right)\right]=\mu_0\nabla\cdot\mathbf{J}_i \ . \tag{3.144}$$

When the first term on the left side of Equation 3.144 is expanded, and also enforcing the Lorenz gauge from Equation 3.141 to be applied now leads to the scalar equation of [51]

$$-\nabla\cdot\left(k^2\phi\right)+k^4\phi+\nabla\cdot\left(k^2\mathbf{A}\right)-k^2\nabla\cdot\mathbf{A}=\mu_0\nabla\cdot\mathbf{J}_i \tag{3.145}$$

Equation 3.145 is important since it is a first-order equation relating the potentials to current density, and has one solution. Equation 3.145 can now be expressed in matrix form

$$\begin{pmatrix} -\nabla^2+k^2 & \nabla k^2-k^2\nabla \\ \nabla\cdot k^2-k^2\nabla\cdot & -\nabla\cdot k^2\nabla+k^4 \end{pmatrix}\begin{pmatrix}\mathbf{A}\\ \phi\end{pmatrix}=\begin{pmatrix}\mu_0\mathbf{J}_i \\ \mu_0\nabla\cdot\mathbf{J}_i\end{pmatrix}, \tag{3.146}$$

which is the key system equation for the 3D model presented in the next chapter since it demonstrates a sparse and symmetric system when expanded [51]. While the

majority of Equations 3.124 through 3.146 are found in [51], they must be presented here for completeness to show how they relate to the first principles of Maxwell's equations, as they show the magnetic and electric potential produced by the current density.

3.3 Relating Maxwell's Equations to Response Functions for EM induction Instruments

Section 3.1 derived the historical definition of apparent conductivity found in [6] from first principles, i.e., Maxwell's equations. In that derivation were expressions based on a homogenous half space, where the earth underneath is homogenous and isotropic. Some of the aforementioned equations will be used to define the relative and cumulative responses for EM induction instruments, introduced in Chapter 2 and used extensively in Chapter 5 as well as Appendix D. However, the equations will be applied to individual layers since the focus is on sea ice and seawater.

The equations for the cumulative and response curves depend on the induction number B. To start the derivation, and for brevity since Maxwell's equations were previously defined, Equation 3.87 can be expanded into a power series, stated as

$$\left(Z/Z_0\right)_{HCP} = \frac{2}{x^2}\left[-9+\left(9+9x-4x^2-x^3\right)\sum_{n=0}^{\infty}(-1)^n\frac{x^n}{n!}\right], \tag{3.147}$$

where $x = k\rho$. According to [21], Equation 3.147 can be recast into the following form

$$\left(Z/Z_0\right)_{HCP} = 1+2\sum_{n=4}^{\infty}\frac{(-1)^n}{n!}(n-1)(n-3)^2\,x^{n-2}, \tag{3.148}$$

where retaining the higher order terms leads to

$$\left(Z/Z_0\right)_{HCP} = 1+\frac{2\times1^2\times3}{4!}x^2-\frac{2\times2^2\times4}{5!}x^3+\frac{2\times3^2\times5}{6!}x^4-\frac{2\times4^2\times6}{7!}x^5. \tag{3.149}$$

Substituting the induction number B in Equation 3.171 yields

$$\left(Z/Z_0\right)_{HCP} = 1 + \frac{jB^2}{2} - \frac{4}{15}\left(2j\right)^{3/2} B^3 - \frac{1}{2}B^4 - \frac{4}{105}\left(2j\right)^{5/2} B^5 \ , \tag{3.150}$$

where, by expanding B, Equation 3.150 can be expressed as

$$\begin{aligned}\left(Z/Z_0\right)_{HCP} = 1 + \frac{j\sigma\mu_0\omega s^2}{4} - \frac{4}{15}\left(j\sigma\mu_0\omega\right)^{3/2} s^3 - \\ \frac{1}{8}\left(j\sigma\mu_0\omega\right)^2 s^4 - \frac{4}{105}\left(j\sigma\mu_0\omega\right)^{5/2} s^5\end{aligned} \ . \tag{3.151}$$

With low induction numbers, $B << 1$, therefore, for both HCP and VCP configurations [21]

$$\left(Z/Z_0\right)_{HCP,VCP} = 1 + \frac{j\sigma\mu_0\omega s^2}{4} \ , \tag{3.152}$$

where the general case can be written as

$$\left(Z/Z_0\right)_{HCP,VCP} = 1 + \frac{j\sigma\mu_0\omega s^2}{4}\sum_{m=1}^{N}\sigma_m Q_m \ , \tag{3.153}$$

where Q_m is the geometric factor that depends on the coil geometry, layer thickness, and coil spacing of the EM instrument, where the mutual impedance ratio depends on the layer conductivities and the geometric factor [21]. The geometric factor also gives the cumulative response of the various layers as a function of layer depth normalized by the coil spacing, and can also be used to estimate the depth of exploration of the HCP and VCP configuration [21]. With that, the geometric factors for the HCP and VCP configurations match the cumulative responses given by Equations 2.7 and 2.8 respectively, as well as those stated in [6]. They are stated again here for completeness:

$$Q_{HCP} = R\left(\zeta\right)_{HCP} = \frac{1}{\sqrt{4\left(\zeta\right)^2 + 1}} \tag{3.154}$$

$$Q_{VCP} = R\left(\zeta\right)_{VCP} = \sqrt{4\left(\zeta\right)^2 + 1} - 2\left(\zeta\right) \ . \tag{3.155}$$

Additionally, the derivative of the geometric factor with respect to ζ give the relative response as discussed in [6] and given by Equations 2.3 and 2.5, and expressed here for completion:

$$\frac{dQ_{HCP}}{d\zeta} = \phi(\zeta)_{HCP} = \frac{4\zeta}{\left(4\zeta^2+1\right)^{3/2}} \tag{3.156}$$

$$\frac{dQ_{VCP}}{d\zeta} = \phi(\zeta)_{VCP} = 2 - \frac{4\zeta}{\sqrt{4\zeta^2+1}} \ . \tag{3.157}$$

As noted in Chapter 2 and [6], if the coil spacing is much less than the skin depth (Equation 2.1) in all of the layers, the relative contribution to the apparent conductivity from all material below the EM induction instrument can be summed independently. To clarify, for a two-layer system, the relative contribution from the first layer is given by

$$\sigma_a = \sigma_1\left[1 - R(\zeta)_{HCP,VCP}\right] , \tag{3.158}$$

where again, σ_1 is the material conductivity of the first layer. The contribution from the second layer is given by

$$\sigma_a = \sigma_2 R(\zeta)_{HCP,VCP} , \tag{3.159}$$

where σ_2 is the material conductivity of the second layer, and ζ is the thickness z over the coil spacing r (Equation 2.4). In total, the sum of Equations 3.158 and 3.159 is the apparent conductivity reading for a two-layer system, and is the same as Equation 2.6, which is repeated here:

$$\sigma_a = \sigma_1\left[1 - R(\zeta_1)_{HCP,VCP}\right] + \sigma_2 R(\zeta_1)_{HCP,VCP} \ . \tag{3.160}$$

To provide a brief discussion of how Equations 3.158-1.60 are possible, and using Figure 2-5 as a reference, one can deduce the contribution to the secondary magnetic field based on the thickness of the layer divided by the coil spacing (i.e., ζ). For example, if ζ has a value of 1, then it can be stated that the material below the

device contributed approximately 25% to the secondary field, and therefore 25% to the apparent conductivity reading. To automate this process of determining the level of contribution to the apparent conductivity registered on the instrument based on an arbitrarily layered earth, the cumulative contribution from each layer can be added together independently as per the conditions previously stated. Equation 3.158 is possible since, at the top layer, the contribution from all of the material below is 100% of the meter reading. Subsequent layers add their own contribution (Equation 3.159), and adding them together produces Equation 3.160. The same process can be extended for a three-layer system, albeit in the following form,

$$\begin{aligned}\sigma_a = \sigma_1\left[1 - R(\zeta_1)_{HCP,VCP}\right] + \\ \sigma_2\left[R(\zeta_1)_{HCP,VCP} - R(\zeta_2)_{HCP,VCP}\right] + \sigma_3 R(\zeta_2)_{HCP,VCP}\end{aligned}, \tag{3.161}$$

where the subscripts next to the response functions indicate that particular layer's response function.

3.4 Chapter Summary

This chapter provided the necessary mathematical background needed for conducting the research in this dissertation. First, the historical definition for apparent conductivity was derived from first principles, i.e. Maxwell's equations, to relate terms used in sea ice geophysics to electrical engineering, thus demonstrating that this work is truly interdisciplinary. Second, the equations used in the 3D full-physics heterogeneous model presented in Chapter 4 were also derived from Maxwell's equations. Finally, the equations that will be used in Chapter 5 (and briefly introduced in Chapter 2) to develop a co-calibration routine among multiple EM induction instruments were also derived from first principles. These equations are based on low-induction number theory, and are dependent on the relative contributions from each

independent layer to provide an apparent conductivity number, which in turn translates to ice thickness. Therefore, the highlight here, as with any original work, is that the results achieved can be traced back to mathematical theory, and in this case the results can be mathematically derived from Maxwell's equations. The next two chapters use the mathematical premise presented here as a background to meet the objectives specified in Chapter 1.

Chapter 4

TESTING A 3D FULL-PHYSICS HETEROGENEOUS NUMERICAL MODEL AS AN ANALYSIS TOOL

This chapter, as presented in [53] and reprinted with permission of the International Glaciological Society per Appendix A, explores simulated responses of electromagnetic signals and quantifies the effects of their responses when using materials that have a different conductivity makeup. Overall, the motivating question for this objective is the following:

How sensitive is an instrument footprint to a material conductivity change when a low-conductive material is surrounded by a stronger conductive material?

This question is answered in three hierarchical steps. First, to provide electromagnetic responses of various ice types, the input characteristics are described for a full-physics heterogeneous computational model called APhiD. The model computes the fields everywhere, where each grid cell acts as a receiver within the model volume, and captures the complete, coupled interactions between air, snow, sea ice, and seawater as a function of their conductivity. Second, visualizations of the modeled simulations are defined as the results are presented in 2D-sliced renderings of their associated electromagnetic fields at discrete frequencies. Third, interpretations of the results present the most important new finding, where conductivity changes affect the EM field response by modifying the magnitude and spatial patterns of current density and magnetic fields. These effects are demonstrated through a visual feature defined as “null lines, ” and are shown in the 2D-sliced visualization output. As a

result, these visualization outputs encourage the use of null lines as a planning tool for better ground truth field measurements near deformed ice types.

4.1 Description of Numerical Model – APhiD

The electromagnetic response of a generalized 3D air/snow/ice/ocean system is modeled here using a finite volume heterogeneous solution to Maxwell's equations, which fully accounts for both ohmic conduction (σ) and displacement current (**J**) effects [51]. The model domain is composed of a rectilinear grid. The cells of this grid are each assigned a particular conductivity (σ)/permittivity (ε) pair of material properties. Magnetic permeability (μ) variations are expected to be negligible in sea ice/water systems and thereby safely ignored [51].

Model cells with defined electric properties are used to describe each material within the model domain. Specific model inputs to consider for a sea ice environment are: 1) definition of grid geometry (cell shape and size) and 2) electric properties of each grid cell. A Cartesian Yee grid cell [54] describes the location and direction of electromagnetic field components. Figure 4-1 displays this grid cell, configured for use in APhiD. The transmitter is approximated in the model by a set of four points along a chosen cell face within the model domain. In this way it comprises a loop antenna, which is representative of the coils found in EM induction instruments. This model can use either HCP or VCP modes as discussed in Chapter 2. With the source and conductivity properties at each grid cell thus defined, electromagnetic potentials throughout the model domain are computed. By inverting the finite volume system of equations with a matrix-free iterative scheme, these calculations are possible. The iterative scheme is differentiated to yield estimates of the observable fields [51]. The quasi-minimum-residual (QMR) method with a Jacobi preconditioner is used with

APhiD for smooth convergence to a solution given a certain tolerance, vice using a biconjugate gradient method for positive definite systems since biconjugate gradient is susceptible to numerical instabilities [55]. This iterative method provides a possible target residual factor τ (i.e., accuracy) of 10^{-12} [51]. Since each grid cell behaves like a receiver within the model volume, each receiver point is a distance r (Figure 2-1) from the transmitter, similar to the coil separation defined in Chapter 2. From this perspective, the responses of many receivers in the model volume, depending on grid size, relative to one transmitter can be visualized from each steady state solution.

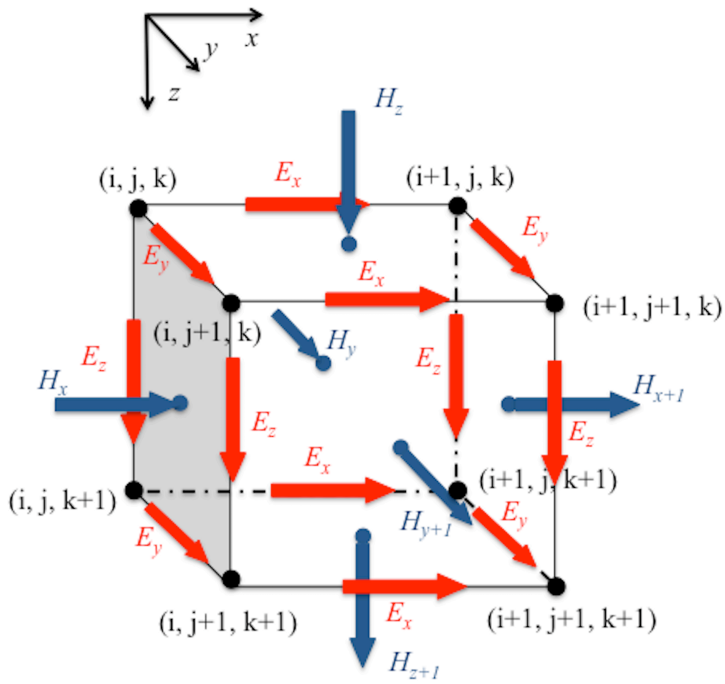

Figure 4-1. Yee grid cell configuration for APhiD. *H* and *E* represent the magnetic and electric field intensities (in units of amperes/meter and volts/meter), and their direction. The black and blue dots indicate nodes where grid corners and faces align. Indices *i*, *j*, *k* relate Cartesian space along *x*, *y*, and *z* directions, respectively.

The goal is to apply APhiD to a sea ice environment as shown in Figure 4-2. The specific parameters of grid geometry and the properties of each cell are discussed here. Since the computation of results depends on both the size of the model volume and overall computation runtime, the geometry of the volume needs careful planning. For this study, a 100x100x150 cell grid is set up with resolution of uniform size 0.5-meter-cubed cells is chosen. Out of this cell grid, 100 vertical cells are attributed with either snow, ice, or water properties, and the remaining 50 vertical cells contain air properties. The electrical properties that comprise each cell, as well as four specific simulation cases used with this setup, are presented in Table 4-1. For simplicity, the air-ice boundary is level across the entire horizontal surface at $z = 0$ m. With this particular configuration, the simulation runtimes average approximately 30 minutes per run. Therefore, multiple runs can be attempted within a reasonable amount of time to analyze visualization results.

Now that the model geometry and the electrical properties of the cells are defined, the transmitter characteristics also need to be determined. As presented in Chapters 2 and 3, EM induction instruments contain both a transmitter and receiver coil, where the transmitter produces an alternating current at a particular frequency in order to produce primary and secondary magnetic fields needed to make apparent conductivity measurements. With this knowledge, a source is chosen that shares the characteristics of a typical EM induction instrument, such as the Geonics EM31 [26, 33]. For example, the operating frequency of the EM31 is 9.8 kHz, which is also the frequency used in the APhiD model runs. Model simulation runs in this study are configured with the transmitter positioned 0.5 meters above the surface of the snow to mimic typical carry heights in the field. Additionally, all simulations reported in Table

4-1 are in the HCP mode, but the VCP configuration is also easily adapted, and shown later in this chapter.

Simulation Cases	Thickness (h) of Snow and Ice Layers	Conductivity (σ) of Ice
1.) Air-Water Only*,***	N/A	N/A
2.) Add Level Ice***	0.5 m (snow) 3 m (level ice)	0.020 S/m*
3.) Consolidated Multiyear Ice Ridge	0.5 m (snow) 3 m (level ice) 10 m (ridge ice)	0.020 S/m* (both level and ridged ice)
4.) Unconsolidated First-Year Deformed Ice Ridge	0.5 m (snow) 3 m (flat ice) 10 m (ridge ice)	0.170 S/m** (level ice) 0.5 S/m** (ridged ice)

* Conductivity (σ) of air/snow is 1.0 x 10^{-8} S/m and seawater is 2.5 S/m throughout as per [1].
** Values per [56].
*** Control runs.

Table 4-1. Simulation types and material properties.

In an actual sea ice environment, however, the conductivity of the sea ice and the seawater are in a constant state of change. But the purpose of these simulations is to look at a snapshot of material conductivities to see how they affect the footprint. Control runs are initially run to provide a reference relative to the existing literature for well-known level sea ice situations. In these cases, such as those discussed in [1], the air, sea ice, and seawater each have their respective bulk conductivity values assigned as though each were an individual layer of material. In an actual sea ice environment, however, the conductivity of the sea ice and the seawater are in a

constant state of change. But the purpose of these simulations is to look at a snapshot of material conductivities to see how they affect the footprint.

The first control run contains air and seawater layers only, such that it provides a base case to simulations that involve more layers. The second control run includes the previous two layers with 0.5 meters of snow added above a three-meter layer of level ice in a configuration matching traditional level-earth models, and is shown in Figure 4-2a. The transmitter for these control runs is located in the center of the horizontal face of a grid cell just above the surface (at z = 0.5 m, Table 4-1).

After running the two control runs, an ice ridge (Figure 4-2b) is added to the model volume to study the effects that geophysical features have on instrument footprint. An ice ridge is represented by adding a simple triangular shape, without surface deformation, to the bottom of the ice layer in the model volume such that the apex of the ridge is in the center. The simulations are run for each ridge scenario to evaluate responses to different positions of the transmitter relative to the ridge. For the first position run in each ridge scenario, the transmitter is located halfway between the start of the model domain and the beginning of the ridge. For the second position run, the transmitter is located at the beginning of the ridge where it just starts to deepen below the level ice. For the final position run, the transmitter is located above the apex of the ridge.

4.1.1 Initializing Conditions

To simulate a ridge in APhiD, a mask file is created, which describes the dimensions of the ridge as well as material layers. This mask file is also based on two criteria. First, the size of the mask is determined by ΔX_1, ΔX_2, and ΔX_3 (Figure 4-2b), where ΔX_1 is the distance from the left edge of the model to the start of the ridge (i.e.,

15 m across given 0.5 m resolution of each cell), ΔX_2 is the width of the ridge (20 m), and ΔX_3 is the distance from the right side of the ridge to the right edge of the model (15 m). Second, an integer value is assigned to each grid cell to discriminate which material corresponds to that cell, such that a mask value of "0" corresponds to a cell with air, "1" is a cell with ice, "2" is snow, and "3" is air. Each mask value is subsequently matched with appropriate conductivity values of a particular material layer.

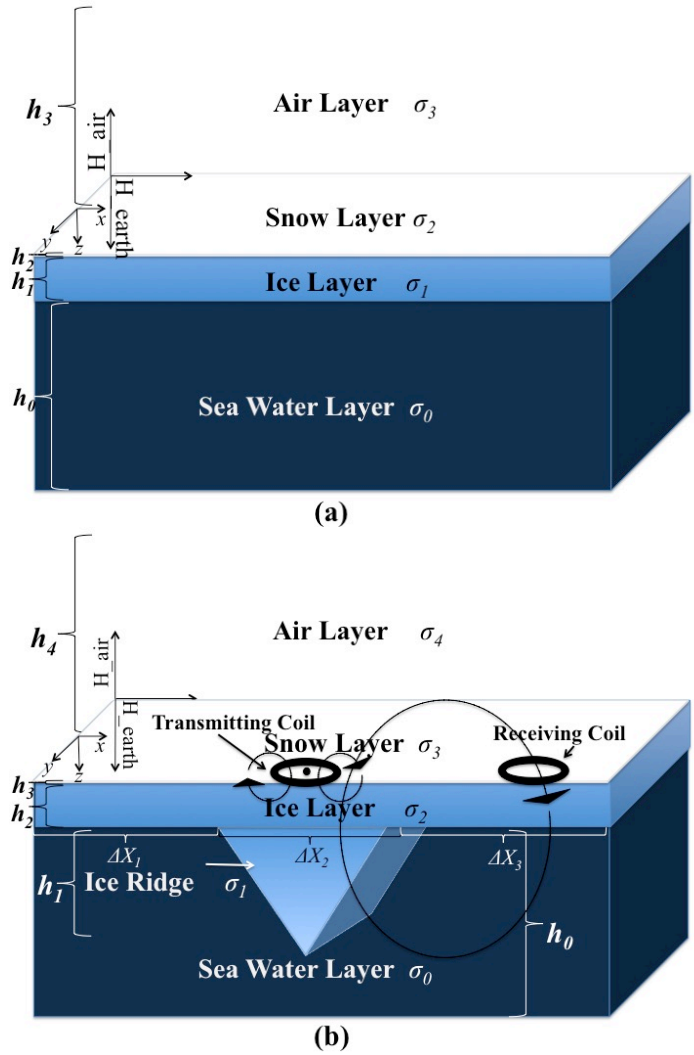

Figure 4-2. Model geometry. Panel (a) is the level ice case configured to match the solution (Figure 2-1) but expanded to a 3D grid. Panel (b) is a deformed ice case involving a simple triangular ridge below sea level (no surface deformation). The *z* direction is positive downward, opposite of that shown in Figure 2-1 Additionally, *H_air* and *H_earth* show the direction of the magnetic field pulse (A/m) through the respective media, and *Transmitting Coil* shows the direction of the position of the transmitter at certain locations as described in the text along the ridge during sequential model runs with the center of the coil shown by the black dot. The *Receiving Coil* is each grid cell in the model volume, with the receiver coil located in the center of each cell and being a distance *r* from the transmitter.

4.2 Characteristics

Using the control runs listed in Table 4-1, the output from APhiD is exported into an open-source, multiplatform data analysis, and visualization software called ParaView [57]. Four specific features are visualized in Figure 4-3 using 2D profile slices to represent the entire volume under study. These four specific features begin with two well-known electromagnetic parameters of (1) electric current density lines, and (2) magnetic flux density lines. Additionally, two parameters are defined to communicate visually interesting characteristics in the field. These two features are (3) color map of magnetic flux density quadrature component in the vertical direction (B_Z*), and (4) effects called "null lines" which manifest as concentrated gradients in the color map of magnetic flux density quadrature each time the polarity of the pulse changes. The purpose of these particular outputs is to demonstrate an electromagnetic response to an excitation of a source through its interaction between a low conductive medium against a stronger conductive medium. Additionally, physiographic features, such as an ice ridge, affect the electromagnetic response. In turn, the changes in these features highlight the differences of footprint based on conductivity changes.

<u>(1) Electric Current Density Lines</u>

By Faraday's Law, a time varying magnetic field induces an electromotive force, which produces an electric current density in a media. White colored semi-circles in the tilted *x*-*y* horizontal slice (Figure 4-3) represent the normalized real component of these current flow lines. These electric current density lines can be related mathematically by Ohm's law, as stated by Equation 3.2.

(2) Magnetic Flux Density Lines

The magnetic flux density (and for our purposes, the normalized imaginary component of the magnetic flux density) is represented by yellow curves emanating from the origin in the *x*-*z* plane (Figure 4-4a). Generally, magnetic flux density is expressed mathematically as Equation 3.4. In electromagnetic theory, the magnetic flux density is also related to the electric field intensity, and, in turn, electric current density, by way of Faraday's law and Ohm's law just described above in subsection (1), and where Faraday's law is expressed as the first equation in Table 3-1.

In a physical sense, what Faraday's and Ohm's laws are saying is that the electric current density lines and magnetic flux density lines are related to each other since their respective fields are transverse waves, where they are mutually perpendicular and also perpendicular to the direction of propagation [58]. Additionally, magnetic flux density **B** has in-phase and quadrature components of

$$\mathbf{B} = \left(B_x + B_x^*\right)\hat{i} + \left(B_y + B_y^*\right)\hat{j} + \left(B_z + B_z^*\right)\hat{k} \ , \tag{4.1}$$

where * indicates the quadrature (imaginary) components produced by the induced eddy currents, and terms without asterisk are the in-phase or real components produced by the transmitter [6, 49, 50].

The strength of the quadrature component of the magnetic flux density in the *z*-direction (i.e., B_z*) is scaled on the color map (Figure 4-3a) with red indicating strongest magnetic flux density. The values of the color map are stated mathematically as

$$C = \log_{10}\left|B_z^*\right| \ . \tag{4.2}$$

It is also important to note that the higher values of magnetic flux density occur at the location of the strongest conductivity response (refer to Appendix B).

(3) Color map

As stated previously, the color map in Figure 4-3 represents the strength of the magnetic flux density's quadrature component in the *z*-direction (B_z*). A change in color shows the exponential decay of the transmitter pulse as it travels through the sea ice and seawater.

(4) Null Lines

When B_z* on the right hand side of Equation 4.2 equals zero (i.e., $C = \log_{10}|0|$), the magnetic field changes polarity during positive and negative cycles as the alternating current transmitter signal travels in the downward (positive) *z*-direction. These polarity changes are referred to as "null lines" because the absolute value of an oscillating signal creates strong gradients, which manifest as strong horizontal lines from a vertically transmitting oscillating pulse of the magnetic field. For illustration purposes, a 1D heuristic example is provided (Figure 4-4) in the form of the well-known damped oscillator of an alternating normalized current sine wave (i.e., what the EM31 generates from the transmitter coil). Assuming a 1D travelling wave propagating downward in the *x*-z plane, a typical decaying (or attenuating) travelling wave within a lossy medium, such as sea ice and seawater, has the general solution form of

$$A(z,t) = A_0 e^{-\alpha z} \sin(\beta z - \omega t + \phi), \tag{4.3}$$

where A is the amplitude (m), A_0 is the initial wave amplitude (m), α is the attenuation constant (Np/m), z is the direction the wave is travelling in, t is the time (s), β is the phase constant (rad/m), and ϕ is the reference phase (rad). It should be noted that

$$\beta = \frac{2\pi}{\lambda} \quad , \tag{4.4}$$

where λ is the spatial wavelength (m) of the wave. Sine dependence is chosen to express the imaginary component as per Euler's identity (and as per Equation 3.22),

$$e^{j\theta} = \cos\theta + j\sin\theta \quad , \tag{4.5}$$

where θ refers to the phase angle [42].

For our study, this general form reduces to the steady state solution for a z-directed wave, with A_0=0.5 m, α=5 Np/m, f = 10 Hz, λ = 0.2 m, t=0 s, and ϕ_0 = 0 rad. Hence, the waveform and its respective envelopes are described mathematically as

$$x_1 = 0.5e^{-5z}\sin\left(10\pi z\right) \tag{4.6}$$

$$x_2 = -0.5e^{-5z} \tag{4.7}$$

$$x_3 = +0.5e^{-5z} \quad , \tag{4.8}$$

where the envelopes show the decrease in amplitude with distance [58].

As the wave travels through a material, the signal attenuates, but still maintains the waveform. When the absolute value of the waveform is taken in Equation 4.3, the waveform shape is no longer represented in negative space (i.e., retaining only positive values – Figure 4-4b). When the waveform intersects zero amplitude, the polarity changes. When the logarithm of zero is taken as per Equation 4.3, strong gradient lines asymptotically approach -∞. In equation form (Figure 4-4c), it can be stated mathematically that

$$x_4 = \log\left|0.5e^{-5z}\sin\left(10\pi z\right)\right| \quad . \tag{4.9}$$

When the absolute value of either envelope is taken in Equations 4.7 or 4.8, and then followed by taking the logarithm, the result forms a straight line of the maximums of the logarithm of the decaying waveform. This equation is expressed as

$$x_5 = \log\left|-0.5e^{-5z}\right| \tag{4.10}$$

$$x_6 = \log\left|+0.5e^{-5z}\right| \tag{4.11}$$

for the envelope in Equations 4.7 and 4.8. Note that with these equations, "spikes" occur each time the waveform amplitude (Figure 4-4a) equals zero, which indicate a change in polarity; thus, a null line is defined. From a geophysical perspective, null lines appear near material boundaries where transmitted signals refract off the sharp material gradient interface.

Another important relationship to describe with the characteristics of this model is skin depth. Skin depth describes the effective penetration depth of an emitted signal through each material, and is expressed as Equation 2.1. It is important to note here that skin depth is not only a vertical penetration parameter, but also a measure of horizontal penetration such that skin depth means the penetration depth through a material in any direction. To provide a numerical example, the skin depth of the sea ice for all simulation cases is shown in Table 4-2 as provided by Equation 2.1, where it can be shown that increasing conductivity leads to less depth of penetration. The ability of APhiD to resolve 3D structure makes it possible to explore horizontal issues that traditional 1D level-earth models could not (Figure 2-1). Most importantly, the mapping of skin depth patterns through the location and visualization of null lines provides us with an effective tool to characterize material conductivities, which are presented next.

Sea Ice Cases	Conductivity (σ) of Ice	Skin Depth (δ) of Ice
1.) Level Ice	0.020 S/m	35.9494 m
2.) Consolidated Multiyear Ice Ridge	0.020 S/m (both level and ridged ice)	35.9494 m (both level and ridged ice)
3.) Unconsolidated First-Year Deformed Ice Ridge	0.170 S/m (level ice) 0.5 S/m (ridged ice)	12.3306 m (level ice) 7.1899 m (ridged ice)

Table 4-2. Comparison of skin depth of all ice types in the simulation cases for a frequency f of 9.8 kHz.

4.3 Simulation Results

To highlight the initial conditions of the electromagnetic response without changing material conductivities, the first control run of the air-water interface only is shown in Figure 4-3a. Here, null lines form a kink at the air-water interface. This feature is subsequently labeled a "kink" because of the pronounced bend in the null line shape at the material discontinuity between the air and water layers. Another important shape to these null lines is their width relative to the coil spacing r. Null line width L, which as presented herein is a visual reference to footprint [35] (term introduced in Chapter 1) or spot size from beam optics [59], defines the footprint size of each polarity change at each depth. Comparing L (Figures 4-3a and 4-3b), footprint is definitely sensitive to each material's conductivity, which is important for showing the relationship between material conductivity and the scale of the electromagnetic field response to different materials.

For the second control run of an air-sea ice-water solution (Figure 4-3b), the magnetic flux density lines also show the kink at the ice-water interface, three meters

below sea level. Notice that the kink here is at a sharper angle in the air-ice-water case than the air-water case (Figure 3-3a). Accordingly, this simulation shows that the footprint L of the magnetic field widens with the inclusion of a layer of level sea ice, compared with the initial case for no sea ice. This result is something unanticipated in prior 1D level-earth models.

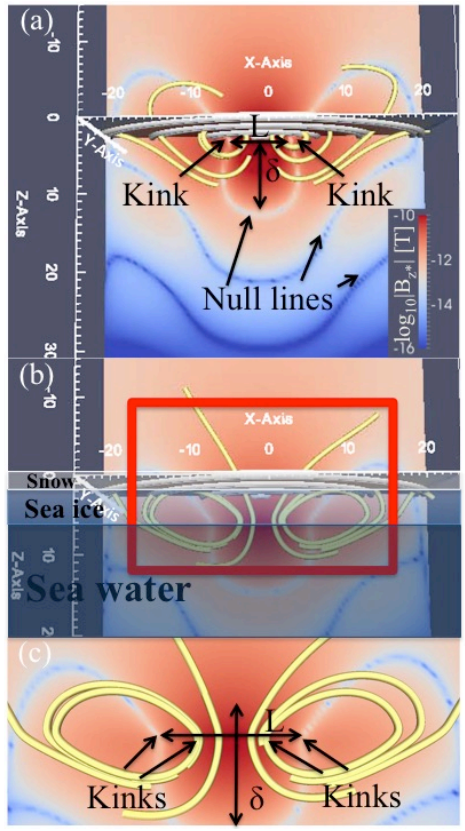

Figure 4-3. Control runs showing simulated field responses from APhiD. Axes shown are in dimensionless grid coordinates with each grid value equivalent to a half-meter resolution. Representative slices of the 50x50x75 m^3 volume provided along the vertical *x-z* slice and tilted horizontal *x-y* slice between induction instrument transmitter source and: (a) an air and water layer; and (b) of air, 0.5 meters of snow, 3 meters of flat level sea ice, and seawater. In the tilted horizontal *x-y* slice, the white colored semi-circles are a half-cut representation of the normalized real component of the electric current density (**J**) in the media as induced by the transmitter magnetic field. The yellow curves emanating from the origin represent the normalized imaginary component of the magnetic flux density (**B**). The color map of the quadrature component of the magnetic flux density in logarithmic space is shown along *x-z* and tilted *x-y* slices (axes in meters). Null lines (highlighted in panel (a) by black arrows) are defined as polarity changes in traveling direction of the transmit signal. These null lines indicate the shape of the magnetic field interaction into the (a) water, and (b) ice then water. Kinks in the null lines and magnetic flux density lines indicate a material discontinuity. In panel (a) and (c), *L* represents the extent/width (spot size) of the magnetic field at the points of polarity reversal. In panel (b), layers of snow, sea ice, and seawater are indicated for clarity. Panel (c) is a close-up of the boxed region of interest from panel (b) to emphasize kinks, skin depth, and footprint size.

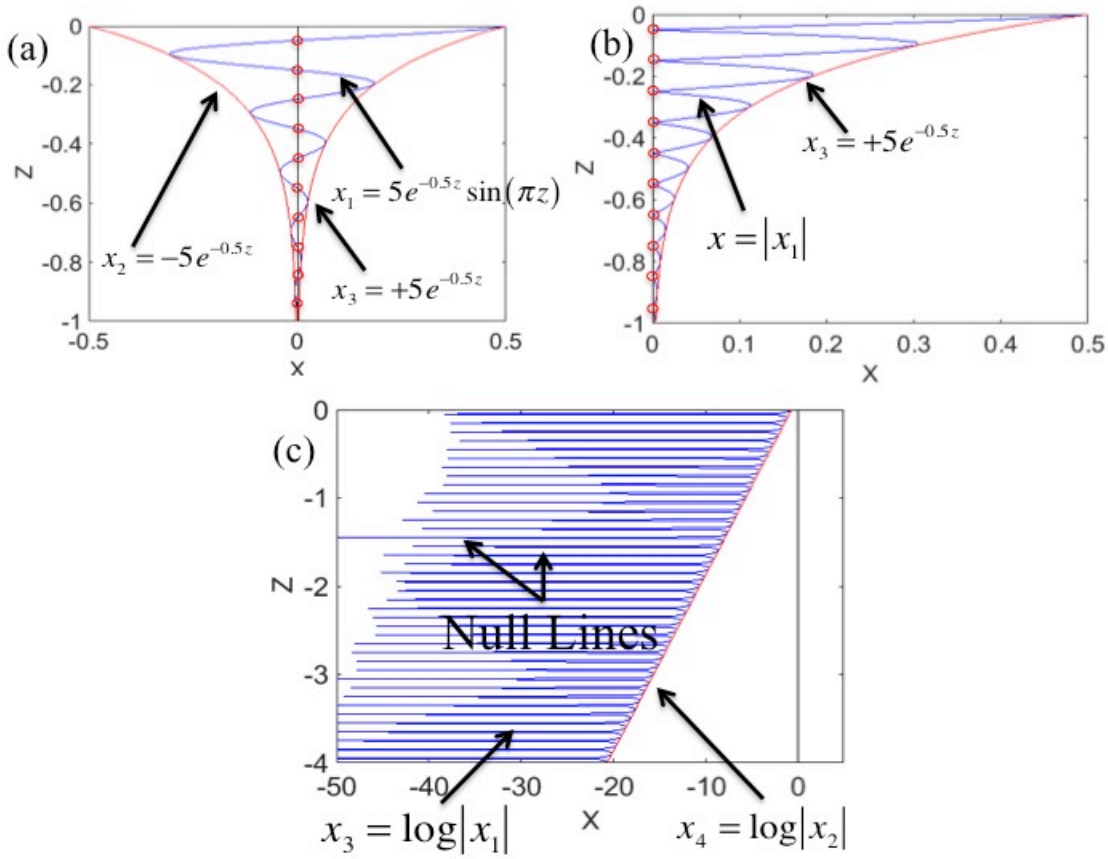

Figure 4-4. Decaying sinusoidal wave. Panel (a) represents a typical sinusoidal wave as it decays when penetrating through a material. Null lines occur at polarity reversals, as denoted by the red circles on the zero line of the amplitude. Panel (b) represents the absolute value of the decaying waveform in panel (a), and also denotes where the null lines/polarity reversals occur at the red circles. The positive envelope is shown for clarity. Panel (c), plotted in logarithmic space, shows how the actual null lines occur when the log is taken of the decaying waveform. Here, the blue waveform (*x5*) possesses "spikes" when the logarithm approaches -∞, thus resulting in a null line. The logarithm of the envelopes (Figure 4-4a) forms a straight line of the maximums of the logarithm of the decaying waveform.

When a simple triangular ridge is added with the same conductivity as the ice in the control run (Figure 4-5), the resulting electromagnetic field pattern gets complicated. First, depending on the location of the transmitter, the current density lines (Figure 4-5; white lines, normalized real component of **J**) outline the ridge structure. Meanwhile, null lines are skewed in various directions depending on the location of the transmitter, with kinks appearing within homogeneous layers. Furthermore, results (Figure 4-6) show variations due to differences in sea ice conductivity for two different ridge cases. The level and ridged ice have two different conductivities (Figure 4-6) following the observations of [56]. These differences impact the current density lines such that they are more flat in shape than the previous simulation (Figure 4-5), and the null lines take on a different shape. Additionally, when the transmitter is directly over the apex of the ridge, the footprint (L) is narrower than in the previous results (Figure 4-5).

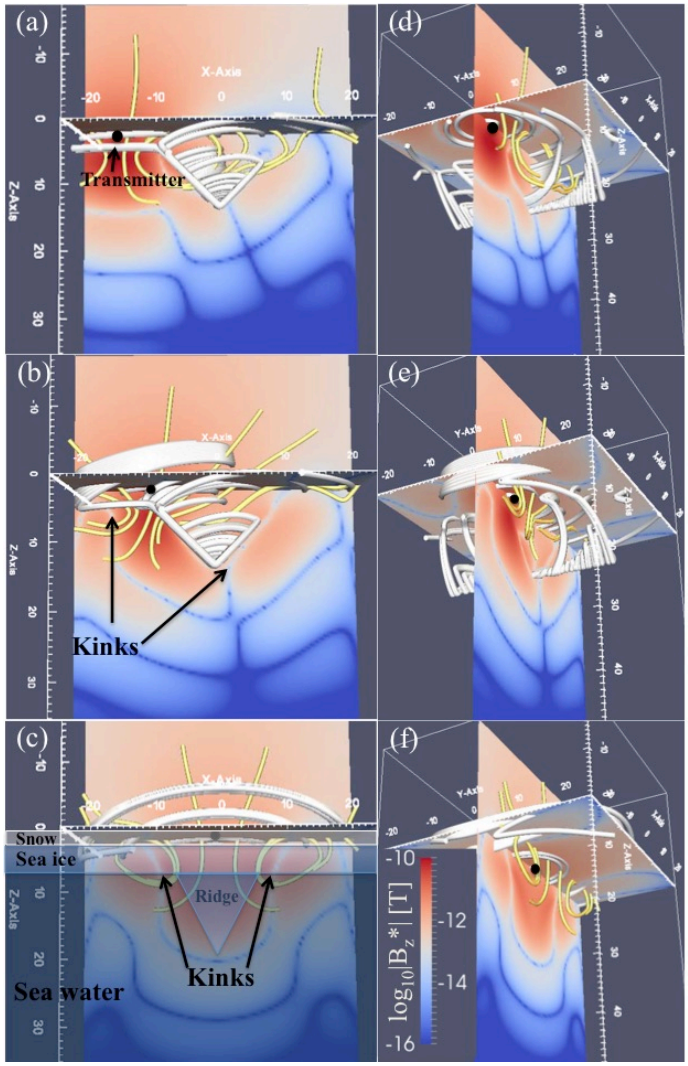

Figure 4-5. Simulated current density lines (normalized real component), magnetic flux density lines (normalized imaginary component), and color map of the quadrature component of the magnetic flux density in logarithmic space for multilayer structure with a multiyear (MY) ice ridge, values as listed in [1] (0.020 S/m for both level and ridged ice). Axes shown are in dimensionless grid coordinates with each grid value equivalent to a half-meter resolution. This configuration has air, 0.5 meters of snow, 3 meters of level sea ice, a MY ridge, and seawater, scaled (Figure 4-3) with the transmitter loop as a black "source" dot shown in an approximate horizontal location for clarity. In panel (c), the layers of snow, sea ice, seawater, and an ice ridge are labeled for clarity. Field line results are shown from two perspectives with source at three locations. Properties of simulation described in Table 4-1, listed as simulation number 3.

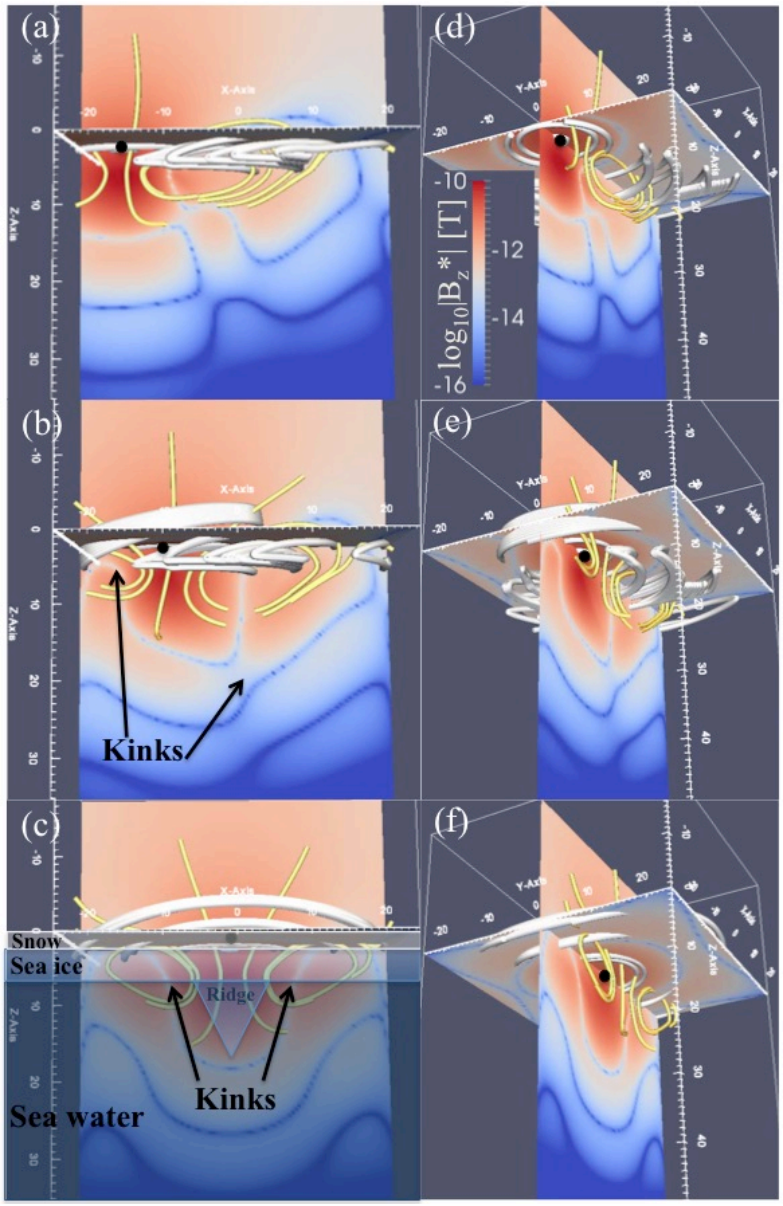

Figure 4-6. Unconsolidated first-year deformed ridge using conductivity values (0.170 S/m for flat ice, and 0.5 S/m for ridged ice) from [56], following Figures 4-3 and 4-5 — simulation number 4 as listed in Table 4-1. Axes shown are in dimensionless grid coordinates with each grid value equivalent to a half-meter resolution. Panels (a), (b), and (c) show a front view of the electromagnetic field mapping of a ridge structure with different conductivity, and panels (d), (e), and (f) show a perspective view from below the seawater/ice interface. Note that the magnetic flux density lines (normalized imaginary component) are more compressed relative to those in Figure 4-5 since the ice is more conductive in this scenario.

As a direct comparison of the various simulation outcomes, the ridge effect (R.E.) differences of the imaginary component of vertical **B** is plotted in Figure 4-7, i.e., B_z*, at each grid cell between the level ice control case (Figure 4-3b) and both ridged cases (Figures 4-5 and 4-6), and cast the absolute value of the difference into logarithmic form. In a mathematical sense,

$$\text{R.E.} = \log_{10}\left| B^*_{z,ridge} - B^*_{z,no\ ridge} \right| . \tag{4.12}$$

The impact of a ridge is more apparent in the consolidated multiyear (MY) ice ridge case (Figure 4-7; left panels) since the ice in the ridge is less conductive compared to the unconsolidated first-year ridge case. For clarification, MY ice is defined as ice that has survived two or more summer melt seasons [3]. Therefore, the R.E. has a larger difference when compared to the control run in the cases where the ridged ice is less conductive since the skin depth has a larger value (Table 4-2). As an additional feature note, the null lines change as the position of the transmitter moves, relative to the deformed ice position, across the *x*-axis.

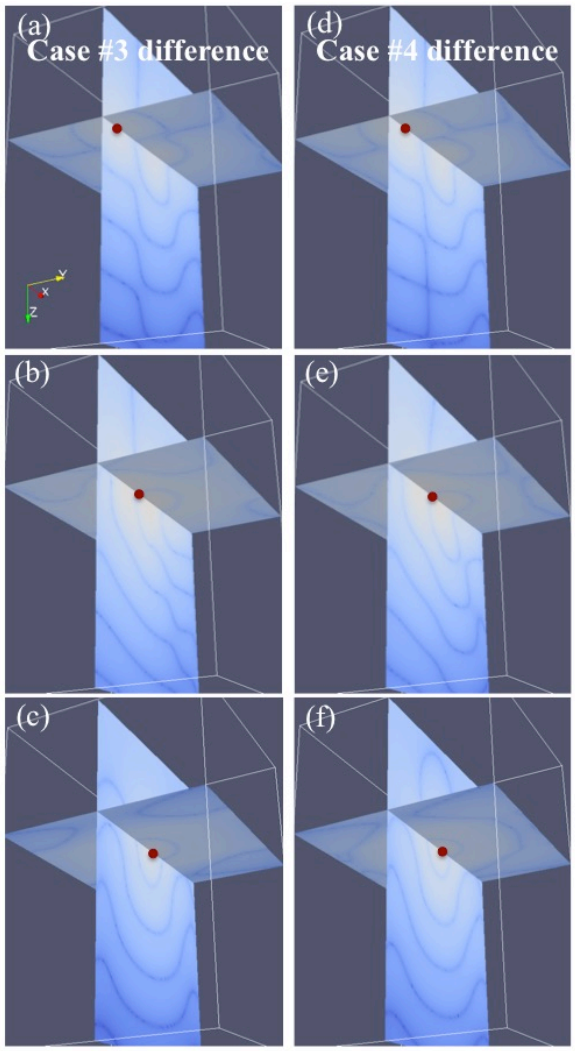

Figure 4-7. Ridge effect differences in null line shape due to the difference between the imaginary components of vertical **B** (*Bz**) cast into logarithmic form. Axes shown are in dimensionless grid coordinates with each grid value equivalent to a half-meter resolution. Results of imaginary vertical **B** component (*Bz**) from ridged ice cases (Figures 4-5 and 4-6) are subtracted from the imaginary vertical **B** component (*Bz**) of the control run (Figure 4-3b), then cast the absolute value of the difference into logarithmic form to demonstrate change in structure of the EM field lines between simulations. Panels (a), (b), and (c) show the results from Figure 4-5 subtracted from those of Figure 4-3b, and panels (d), (e), and (f) show the results from Figure 4-6 subtracted from those in Figure 4-3b. Transmitter is shown with red outlined dot and placed in its approximate horizontal location for clarity. Note that the strongest differences occur in panels (b) and (e) with the transmitter at the edge of the ridge rather than the apex.

4.3.1 Model Results for Transmitter in VCP Orientation

Up to this point, the numerical model results are shown based on a transmitter in HCP configuration. The results of the HCP configuration study are very important as they challenge historical approximations to the layered-earth model. But the focus of this section is on the physical characteristics (such as the current density and magnetic field density lines) of the electromagnetic field response when the transmitter is in the VCP configuration and encounters the same interfaces as the first two control runs shown with the HCP configuration. The eventual goal is to relate the numerical model to field data collected in Barrow, Alaska, during March 2013, where the data was collected in the VCP configuration. To visualize the difference in dipole configurations with respect to the model, refer to Appendix C.

For a visual comparison, Figure 4-8 displays 4 cases. Panels (a) and (b) are the control runs in the vertical polarization as shown in Figure 4-3. Panels (c) and (d) are the same as panels (a) and (b), with the exception of the snow layer being omitted since it has the same conductivity as air in these modeling scenarios. However, the rest of the parameters are the same in terms of material conductivities, operational frequency, transmitter location, and 3 meters of level sea ice are the same, albeit in the VCP polarization. Panels (e) and (f) are side views of panels (c) and (d). Some of the characteristics that result have the same principle as the vertical polarization, such as the null line kink at the material boundary (refer to Figure 4-9 for a clearer aspect). There are two key differences, outside of the polarity change, between the sets of panels in Figure 4-8. First, the current density lines are remarkably different than the HCP polarization case. While the magnetic field density lines also are different due to the polarization change, and while the current density lines still exist in the *x*-*y* plane, they also possess a sharp 90° turn into the vertical direction, and also "dip" to the

ice/water interface when 3 meters of ice is present, as compared to the air/water only case. Second, the null line width L is much wider than compared to the HCP case. Like the HCP case, L increased when a material is added (in this case sea ice), proving again that even slight changes in conductivity affect the overall response. Figure 4-10 presents a numerical value attribute to L to quantify how much L does change based on polarization state, where L is wider in VCP than HCP. This widening can be attributed to the relative response to the secondary magnetic field, where the relative contribution from the material near the surface is large, but falls off with depth as discussed in [6] and shown in Figure 2-3. In summation, it is key to have a proper visualization aid of the field responses based on the configuration of the instrument at the time of data collection. This visualization tool displays what is physically taking place in the electromagnetic realm when the user of the EM induction instrument presses the button on the device to take a measurement. Simply put, a lot of interesting physical interactions take place in this environment, with more to be explored beyond the scope of this work.

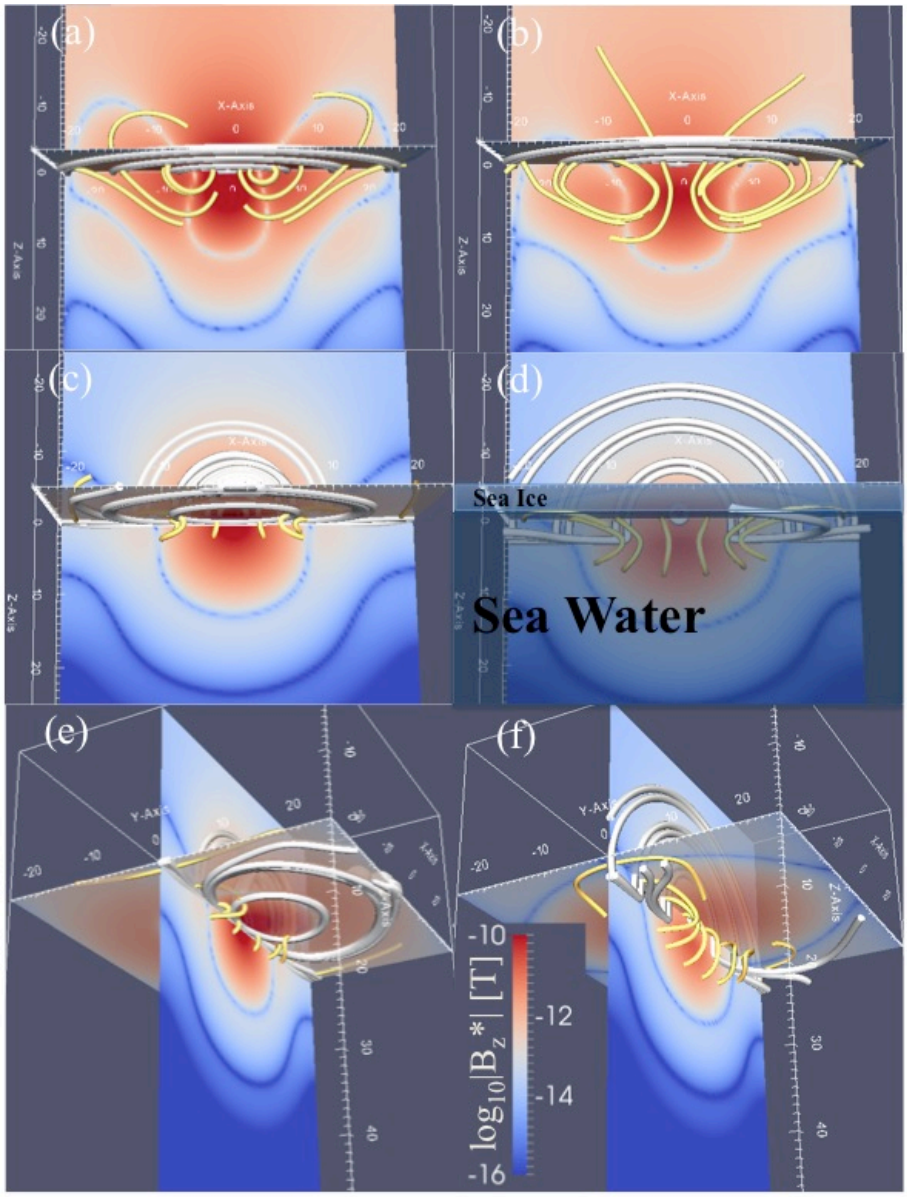

Figure 4-8. HCP configuration control runs versus VCP configuration control runs. Axes shown are in dimensionless grid coordinates with each grid value equivalent to a half-meter resolution. Panels (a) and (b) are the air-water and air-snow-ice-water interface, respectively from Figure 4-3. Panels (c) and (d) are the same as (a) and (b) but in VCP polarity (with the exception of the snow layer being omitted since it has the same conductivity as air in these modeling scenarios) in regard to material parameters and operating frequency. Panels (e) and (f) are side views of panels (c) and (d). It should be noted that the color map shown in panel (f) is the same scale used in both HCP and VCP polarizations.

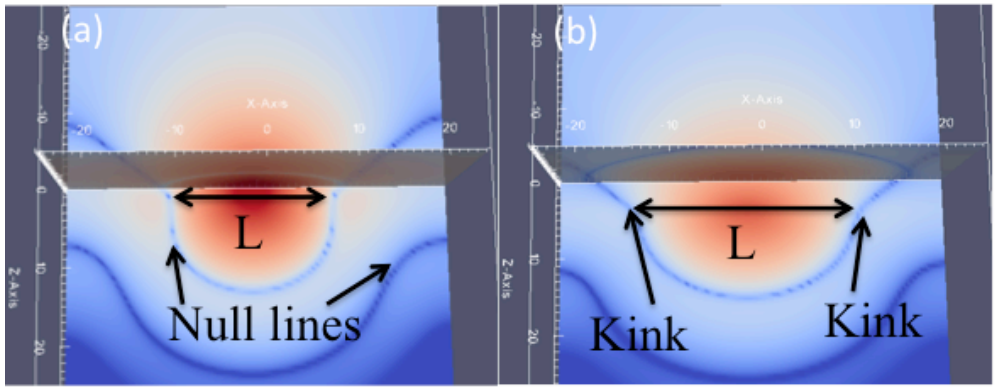

Figure 4-9. Continuation of Figure 4-8 where the field lines are removed for clarity. Panel (a) is the air/water only case, and panel (b) is the air/ice/water case, where 3 meters of level ice are added, where both cases are in VCP polarization. In this figure, the null line width *L* is much wider than those of their respective counterparts in HCP in Figure 4-8 panels (a) and (b). Axes shown are in dimensionless grid coordinates with each grid value equivalent to a half-meter resolution.

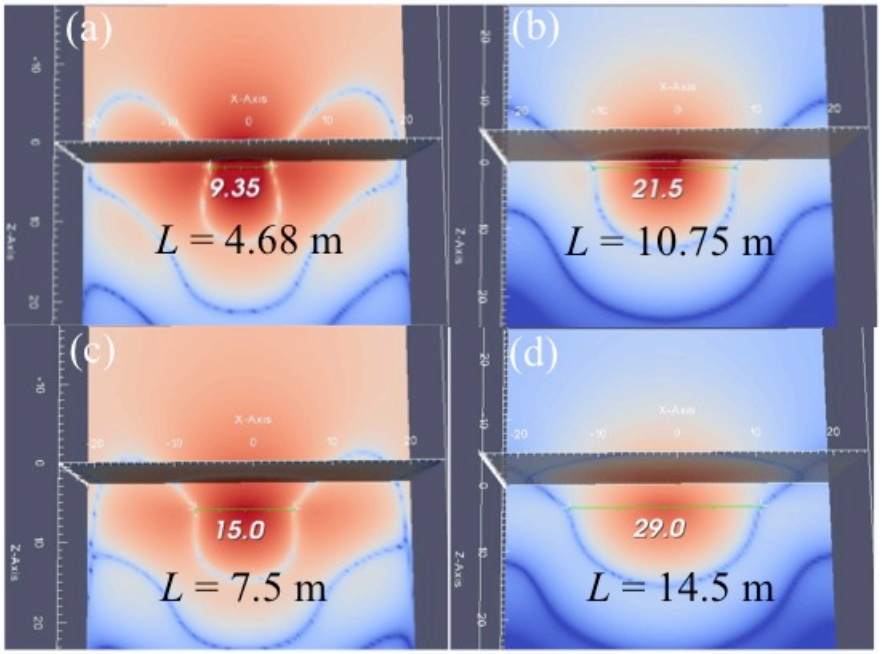

Figure 4-10. Demonstration of numerical value of *L* based on polarization change (field lines removed for clarity). *L* is the length of the green horizontal line. Panels (a) and (b) represent the air/water only case of the control runs established in Table 4-1, where panel (a) is in HCP and panel (b) is in VCP. Axes, as well as the numbers in white reported underneath the green horizontal line, are in dimensionless grid coordinates with each grid value equivalent to a half-meter resolution. Accounting for half-meter resolution, actual numbers for *L* are reported within the plots. Panels (c) and (d) represent the 3 meters of level ice added as part of the control runs established in Table 4-1, where panel (c) is in HCP and panel (d) is in VCP. It is important to note that the only case where *L* is numerically close to *r* of 3.67 meters (as used with the Geonics EM31 [26]) is panel (a) in HCP, since VCP is more sensitive at the surface when compared to HCP.

4.4 Simulation Discussion, Insights, and Impacts

Low-frequency induction results examined here identify the ice-water interface through the exponential decay of long-wavelength secondary-eddy-field responses in the near field, i.e., distances much less than a wavelength. This exponential decay generates a system of eddy currents induced within each material layer. The result is a

sensitive measure of distance between the receiving antenna and material conductivity along any direction. As such, the sensitivity of eddy-field responses is comparable to ground penetrating radar (GPR) responses since both concepts are based on the detection of a signal through a medium from a transmitting device [58]. However, as stated previously, when compared to EM induction instruments, GPR has difficulties with high salinity ice (brine inclusive ice) as it will attenuate the signal and cause scattering [20, 60, 61]. In line with this thought, it seems that EM induction, through the results of these simulations, may also be affected from scattering, perhaps more so than first thought. Hence, this study is only beginning to simulate a number of new and interesting responses of EM systems when explored as 3D responses.

Some of the positive outcomes of the model results are as follows. First, pending a number of graphical improvements, the modeling results shown herein can be used to plan more effective field experiments before making expensive excursions to the Arctic; specifically seasonal and regional sensitivities related to strong conductivity gradients as well as site selection, line survey selection methods, and approaches to physiographic features. In particular, model simulators such as APhiD provide a capability to numerically test novel sensor packages that measure the complete, three-component induction field for a given transmitter antenna. These novel packages can be designed either through a range of fixed frequencies, or preferably as a transient pulse. Historically, such an approach was adopted in the early 2000s by service providers in the hydrocarbon well-logging industry, such as Schlumberger, Baker Atlas, and Halliburton [62-64], when it became apparent that geological anisotropy confounded traditional methods of well-log data analysis. Several years later, deployment of 3-component, multi-sensor induction logging tools

are the standard in difficult drilling environments, geo-steering and measurement-while drilling, although the tools are still proprietary. Therefore, the results of this study can be seen as potentially leading to a similar shift in sea ice measurement technologies, thus inviting future mapping work and analysis on the full 3D nature of climate/sea ice dynamics.

Second, airborne 3D modeling work in sea ice was attempted before [65], but after extensive and advanced computing only minor improvements were made in analyzing field data [29]. Since computers have increased in processing power over time, a new capability now exists with APhiD to produce 3D electromagnetic models. As per the results here, the output produces interesting results that not only show the current density lines and the magnetic flux density lines, but they also show how the entire field reacts as a function of 3D distributed material conductivities, as well as the footprint changes based on material makeup and instrument polarization. As shown in Appendix B, the relationship between the model output and material conductivities provides an opportunity to increase understanding between geophysical properties, such as material conductivity, and instrument responses, such as apparent conductivity. When the field encounters level sea ice instead of an air-water interface (such as Figure 4-3), the footprint size increases along the horizontal, even more so when using VCP configuration. This footprint is important because the instruments used in the field assume a footprint based primarily on the carrying height of the instrument [35]. Conversely, in these findings, the footprint of a pulse varies considerably based on the conductivity of the material outside of instrument polarization, which means that the footprint of the instrument is going to be sensitive to ice type, season of year, temperature, and other environmental variables not

currently formulated in any EM models. Further studies are underway to quantify how L varies as a function of sea ice conductivity, with the intention to develop an algorithm characterizing these changes from parameterized physical properties.

Third is the potential use of APhiD as a planning tool for positioning instruments in the vicinity of sea ice ridges to improve ground truth data collection best practices. There are considerable patterns (Figures 4-5 and 4-6) that are reminiscent of refraction and physiographic interference at the beginning of the ridge. A postulate here is that the physiographic feature —i.e., the ice ridge — induces both refraction and interference patterns depending on the ridge shape and conductivity of the ice. To explain, both of these patterns are based on Huygens-Fresnel principle. Refraction is where the electromagnetic waves "bend" — visually similar to the appearance of a pencil in a glass of water — due to the wave speed change across the boundary of two different media dependent on its material properties, such as conductivity [58]. Interference is the result of the spherical wave generated by the wavefront — in our case, the wavefront is the transmitter coil — where the envelope of the spherical waves constitutes a new wavefront via superposition [59]. The only time that these patterns do not occur is when the transmitter is above the ridge apex, in which case ridge symmetry matches the field shape waveform symmetry.

Hence, the beginning of the ridge may be a promising area for an EM refractive and interference process study, while the peak of the ridge is more important to EM calibration. APhiD also provides a means to rethink instrument designs for in situ measurements to capture 3D data by leveraging understanding about changing footprints (ΔL) as a function of sea ice conductivities (or lack of conductivity in the associated snow layer – which also impacts footprint size). The magnetic flux density

lines bend away from the vertical when a pressure ridge is present since the ridge is less conductive then the surrounding seawater. The MY ice (Figure 4-5) is less conductive than the unconsolidated ridges (Figure 4-6), hence the magnetic flux density lines are further away from the vertical in Figure 4-5. The tendency for these lines to appear further away provides potential insight when interpreting airborne EM responses due to spatial resolution such as NASA's IceBridge program [66] and a multi-sensor airborne sea ice explorer (MAiSIE) [56]. A benefit to using APhiD is that it is a tool that can be modified for any number of scenarios, as shown with the polarity change in Figures 4-8 and 4-9.

4.5 Conclusion

A set of simulations of the electromagnetic response of various sea-ice types has been discussed here in order to demonstrate how variable footprint is to conductivity changes within materials of low conductivity, such as sea ice, which are surrounded by stronger conductive materials, such as seawater. These simulations mimic an environment where an electromagnetic induction instrument, as commonly used in sea ice field studies, interacts with different conductivity values within different media to display the footprint sensitivity in the visualizations shown throughout this chapter. Current approximations using the 1D layered-earth solution assume that material layers above the conductive seawater are essentially negligible in terms of conductivity. However, with the results presented in this chapter, changes in conductivity, especially at the sea ice/seawater interface, do have an effect on the overall 3D electromagnetic field response in both polarizations, thus answering the scientific question posed in the introduction of this chapter. A simple change of the location of the transmitter, with respect to deformed ice, also leads to interesting

electromagnetic field responses as demonstrated in the visualizations of the deformed ice simulation cases.

In summation, four key findings are identified. First, using a full-physics, heterogeneous finite volume EM model demonstrates through a qualitative visualization how the inherent assumptions in existing 1D model approximations are violated when physiographic features are present. Second, APhiD modeled EM parameters can be combined to show where null lines, or polarity reversals of the magnetic field, are located. Third, these null lines constitute kinks at different material interfaces with different conductivity makeup. Null line kinks also develop uniquely through field patterns when physiographic features are present. While these patterns are more pronounced when they encounter the beginning of a ridge as per the simulation cases described in the text, further study is warranted to explore if these patterns can aid in determining the shape of the ridge in addition to the thickness. Finally, the most important outcome is that sea ice conductivity has an important role to play in the horizontal extent of EM footprint sizes, as shown in null line width L, and therefore is a key parameter for interpreting EM thickness retrievals from field campaigns. These simulation results can be explored further to develop new in situ instruments, improve ground truth calibration, and validate airborne, spaceborne, and underwater instruments.

4.6 Future Considerations

Work with the APhiD model can continue in several ways. Even though the simulations focus on a particular defined scenario of ridged ice where there is a singular ridge, the reality is, that for an actual Arctic environment, there are multiple ridges, with different sizes and different conductivities. The sizes of the ridges depend

on many factors, such as the water currents underneath the ice, as well as the surrounding environment on the topside of the ice, such as the changing of the seasons, weather storms, etc. Sheets of ice can also collide with one another to form ridges. As far as the conductivity of the sea ice is concerned, again, many factors come into play with that as well. Some examples include brine intrusions, air pockets, and repeated melt/freeze cycles within the ice itself.

As far as modeling these different scenarios with the model discussed in Chapter 4 are concerned, it is possible, but must be limited to a reasonable volume size so that simulation results can be achieved in a practical amount of time. Another possibility would be to run the simulations in "batch mode" on a cluster. The results in Chapter 4 were based on running one simulation at a time. Running "batch mode" allows several simulations to be run at once on a cluster of high-performance computers. This action can potentially allow more complex scenarios to be defined within the model volume and still finish within a finite time window (vice running several days).

One possible scenario for running in batch mode is to analyze two ice ridges coming into contact with one another. This contact would ultimately lead into a collision that would form a singular ridge of different shape and structure. An interesting result would be to analyze the electromagnetic field responses that result in this collision to see what effects it produces in an electromagnetic sense. Additionally, the transmitter can also be placed in different positions to visualize the field from a different perspective in these scenarios. In short, there are multiple possibilities that still exist with the APhiD modeler.

The accuracy of the model can also be improved. Currently, the target residual τ is 10^{-12} as previously mentioned. This factor can be decreased (i.e., less than 10^{-12}) in APhiD to increase the accuracy of the simulated solutions, but would result in longer runtimes of the simulation, and also lead to having the maximum amount of iterations increased. Even though the τ in APhiD is low, one possible alternative method to improve the accuracy further, independent of APhiD, is to use a direct solver to compare solution accuracy. Direct solvers are methods that solve linear systems by a finite sequence, unlike iterative solvers that update "guesses" and converge to a solution. Hence, direct solvers are more robust as they can provide an exact solution. Even though direct solvers (such as LU factorization used in matrix operations) can provide an exact answer, they are typically more computationally expensive then iterative solvers [67]. This problem alone does not affect APhiD, but is a common issue in numerical computing.

While the results presented here are based on numerical simulations, the ultimate goal would be to adapt current instrumentation to extract more information from the sea ice and seawater than just 1D apparent conductivity measurements. One possible approach would be to have an EM induction instrument that has one transmitter and many receivers. This approach would mimic the simulation scenario because each grid cell in the APhiD volume can be considered its own receiver. However, instead of being confined to just software, the actual EM induction hardware would capture the information over the sea ice directly. The receivers could be configured in such a way on the ice so that the full 3D response would be received. Additional configurations could have software integrated into this prototype EM

induction instrument that provides the information that APhiD does, albeit in real time.

Chapter 5

FIELD EXPERIMENT AND CO-CALIBRATION ALGORITHM

In order to address the improvement in the accuracy of sea ice thickness measurements by way of magnetic-dipole type EM induction instruments, one of the objectives in this dissertation is to develop a co-calibration algorithm for these types of instruments to improve best field practices. In order to meet this objective among these types of EM induction instruments, several steps need to occur, and are discussed in this chapter as follows. First and foremost, a field experiment is needed to collect the necessary apparent conductivity data among physically different EM induction instruments. This experiment enables a direct comparison of data collected by two different instruments over the same material, which, in this case is sea ice. Second, a historical calibration routine is presented, and concludes with the reason of why an alternative routine needs to be developed. Third, the co-calibration routine is developed from solving a linear set of two equations that have two unknowns. Fourth, conditions are implemented to establish valid solution pairs, which are used in the inversion solution for ice thickness, which also concludes that section.

5.1 Field Experiment

During March 2013, a field campaign was established to collect data from Barrow, Alaska. Barrow is situated inside the Arctic Circle and contained vast amounts of ice for study. In order to determine ice thickness in Barrow, two EM induction units were used to collect the apparent conductivity readings of the sea ice:

the Geonics EM31-MK2, and the GSSI EMP-400 (refer to Figure 2-3). The apparent conductivity readings were collected using data loggers, set up in a manual configuration in which the user of the instrument presses a trigger button to record the data at a pre-determined location. The data loggers consisted of the Allegro Field PC used with the Geonics EM31-MK2 and the Trimble GeoXH used with the GSSI EMP-400. Additionally, Global Positioning System (GPS) data was also logged where both use World Geodetic System-84 datum operating in the "Fix Data" sequence [68], along with the time of the reading, and the survey leg number. The Trimble GeoXH was connected to the Allegro Field PC to provide GPS data, since the Allegro Field PC alone does not have that capability, and the Trimble GeoXH itself has a Wide Area Augmentation System (WAAS) built into it along with the software for the GSSI EMP-400.

Overall, data was collected with the EM induction instruments over two days on a survey line, where one day used the EM31, and the other day used the EMP-400. On this survey line, calibration points, which are drilled holes in the sea ice, are established at 25-meter increments with their measured ice thicknesses recorded. The length of the survey line was approximately 400 meters long over mostly flat ice along the shoreline in Barrow, where the collected apparent conductivity samples were collected at one-meter intervals. Included in these intervals are 16 calibration points, since, as stated previously, the calibration points were drilled at every 25 meters, including the start point of the survey line. Both instruments collected data in VCP mode. The Geonics EM31-MK2, with an operating frequency of 9.8 kHz, not only logs apparent conductivity values, but also in-phase readings, and GPS information. However, it should be noted for completeness that the in-phase readings were not

recorded properly with the EM31, even during instrument testing before Barrow, possibly due to damage beforehand (due to it being a rental unit). The GSSI EMP-400 logs more information compared to the Geonics EM31-MK2, in that it has a built-in accelerometer for tilt error and an altimeter for the altitude above mean sea level. Additionally, the GSSI EMP-400 also logs the multi-frequency data of the in-phase, quadrature, and apparent conductivity values, as well as the calibration data when the instrument is calibrated to the ground and the approximate height it will be carried. It is noted here that since the objective for using the GSSI EMP-400 was to collect apparent conductivity data, one of the transmit frequencies needs to be set at 15 kHz per the user manual [69]. Therefore, the transmit frequencies of 1, 10, and 15 kHz were used in the field experiment. Table 5-1 shows some of the physical characteristics of both instruments.

Specification	Geonics EM31-MK2	GSSI EMP-400
Operating Frequency [kHz]	9.8	1,10,15
Coil Separation [m]	3.67	1.219
Weight [lbs.]	10	25
Instrument Carry Height on Survey Line [m]	0.9 (West), 0.95 (East)	0.22

Table 5-1. Physical characteristics attributed to the Geonics EM31-MK2 and GSSI EMP-400.

There are benefits and drawbacks to using a multi-frequency unit such as the GSSI EMP-400. Recall that the skin depth, per Equation 2.1, tells us how far a signal can penetrate into a given medium based on certain parameters, such as the frequency used and the conductivity of the medium. At the frequencies stated, and using a bulk

conductivity parameter of 20 mS/m from the literature [1], the multi-frequency instrument would not be skin depth limited, and would still meet the low-induction number standard since the coil spacing (1.219 m for the EMP-400) is much less than the skin depth. An advantage here would be to use a lower frequency (1 kHz) to look at thicker ice since it can penetrate further via the skin depth relationship, and thus improve the resolution capability for determining sea ice thickness over ridges. Additionally, since the EMP-400 has a shorter coil spacing then the EM31, the expectation for the instrument is that it would deliver improved resolution over ridged ice [70]. In this same vein, higher frequencies (such as 15 kHz) could also provide better resolution for shallower ice cases since the penetration depth required is much less than thicker ridged ice. However, [71] does raise the issue of having a multi-frequency instrument accurately setting and maintaining zero-point calibrations (i.e., instrument zeros) among the multiple frequencies. To counter this point, GSSI commissioned a field study on sea ice that compares both the Geonics instrument and the EMP-400. The results achieved with both instruments show that there is no difference in derived ice thicknesses over flat ice, and with ridged ice there are slight differences at different frequencies but are insignificant [70].

As mentioned previously, the raw data imported from the loggers used to a local machine for analysis was recorded in the fix data sequence. In order to use this data for further calculations, another routine needed to be developed in order to post-process the data. Post-processing of the data makes the measured apparent conductivity values easier to develop into codes to determine ice thickness. This particular routine was written in PV-Wave, which is an array-based programming language that has routines based on the International Mathematics and Statistics

Library (IMSL) [72]. Therefore, data post-processing was a necessary first step, not only for the purpose of this dissertation (and starting with the following section), but also for archiving in the National Science Foundation's Arctic Data Repository [73]. Tables 5-2 and 5-3 shows a "cut-away" of what the raw data looks like, and what the data looks like after post-processing, respectively.

```
@,235051.00,7119.963154,N,15640.819460,W,2,09,1.0,15:50:38.91
SH10      1.000   222.750    20.478 15:50:39.19
@,235052.00,7119.963153,N,15640.819483,W,2,09,1.0,15:50:39.74
@,235103.00,7119.962785,N,15640.820648,W,2,09,1.0,15:50:50.78
@,235103.00,7119.962785,N,15640.820648,W,2,09,1.0,15:50:50.78
SH10      2.000   222.250    20.478 15:50:51.49
@,235104.00,7119.962781,N,15640.820656,W,2,09,1.0,15:50:51.76
@,235111.00,7119.962351,N,15640.821861,W,2,09,1.0,15:50:58.68
SH10      3.000   221.250    20.478
15:50:59.51@,235112.00,7119.962354,N,15640.821875,W,2,09,1.0,15:50:59.78
```

Table 5-2. Typical representation of raw data collected in the field from an EM induction instrument. This example data is from the Geonics EM31-MK2.

Index #	σ_a	Latitude	Longitude	HH Alaska Local	MM Alaska Local	Sec Alaska Local
1	222.75	71.33271923	156.68032446	15	50	39.19
2	222.25	71.33271304	156.68034423	15	50	51.49
3	221.25	71.33270589	156.68036453	15	50	59.51

Table 5-3. A sample of post-processed data derived from the points in Table 5-2 ready for calculation purposes and archiving.

5.2 Relating Field Collected Apparent Conductivity to Sea Ice Thickness via a Non-linear Regression Approach

The last section detailed how the apparent conductivity information was collected on sea ice using EM induction instruments. Now, the apparent conductivity

data collected with the Geonics EM31-MK2 is used in order to develop a relationship between the apparent conductivity data itself and actual ice thickness data from the calibration points along the survey line. One method that can be used here is an exponential best-fit curve. In a mathematical sense, this exponential fit used to describe the aforementioned relationship, as shown in [35], is stated as

$$\sigma_a = A + Be^{(-Cz)} \tag{5.1}$$

where A, B, and C are the modeled coefficients, and z, which is the distance between the instrument and the highly conductive seawater, is the inverse of Equation 5.1, stated as

$$z = z_{ref} - \ln(\sigma_a - A) / C \tag{5.2}$$

where

$$z_{ref} = \ln(B) / C \ . \tag{5.3}$$

Since z is now determined, the actual sea ice thickness z_i can be determined through the following equation as

$$z_i = z - z_0 - z_s \tag{5.4}$$

where z_0 is the distance between the instrument and the top surface, otherwise known as the instrument carry height (see Table 5-1), and z_s is the snow thickness, which, for the purposes of this dissertation, is assumed to be 5 cm on the survey leg.

The modeled coefficients are necessary pieces to these equations. But in order to establish their final values, an initial guess has to be made. The initial guess chosen for this data set was based off of values from another ice experiment in the Arctic [74], which are correlated values determined from [33]. The values from [74] are from the Barrow area during April of 2007, and these values were chosen as an initial guess since the excursion took place at roughly the same time during the year (March).

These values for the initial guess are as follows: A = 54.7, B = 1178.4084, and C = 0.872.

Based on the further analysis of the initial guess, the values for A, B, and C are more refined by using a non-linear regression routine found in PV-Wave software, where the solved coefficients used herein are A = 26.48, B = 1049.40, and C = 0.7624 [35]. With these coefficients, a plot is cogenerated along with the drill hole thickness measurements at calibration points, and apparent conductivity collected at those particular calibration points, on a single plot shown in Figure 5-1. The plot shown in Figure 5-1 allows visualization of all apparent conductivity points collected to be translated into a total thickness as defined by Equation 5.2. In this data set, the uncertainty is +/- 0.1442 meters.

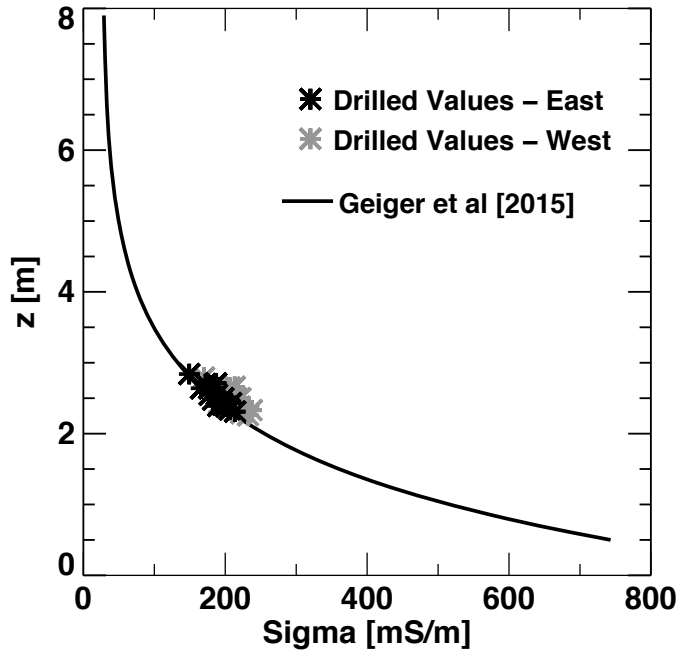

Figure 5-1. Plot of exponential relationship between vertical distance (z) of instrument height combined with total snow and ice thickness versus apparent conductivity values (where here in the x-axis, "Sigma" is equal to σ_a) of strongest source (seawater beneath sea ice). Also shown are drilled calibration points. Because most of the sea ice along transects were from flat and level first year (FY) ice, the coefficients chosen are of those found in [35].

In order to visualize how these numbers are able to report just the ice thickness of the transect, Figure 5-2 shows a MATLAB plot of the ice thickness profiles of the Geonics EM31 data in two directions, east and west, where west is heading away from the center of the survey array, and east is heading back towards the center. Additionally, the thickness of the calibration holes is also shown as green circles on the plot along with the thickness data of the EM31.

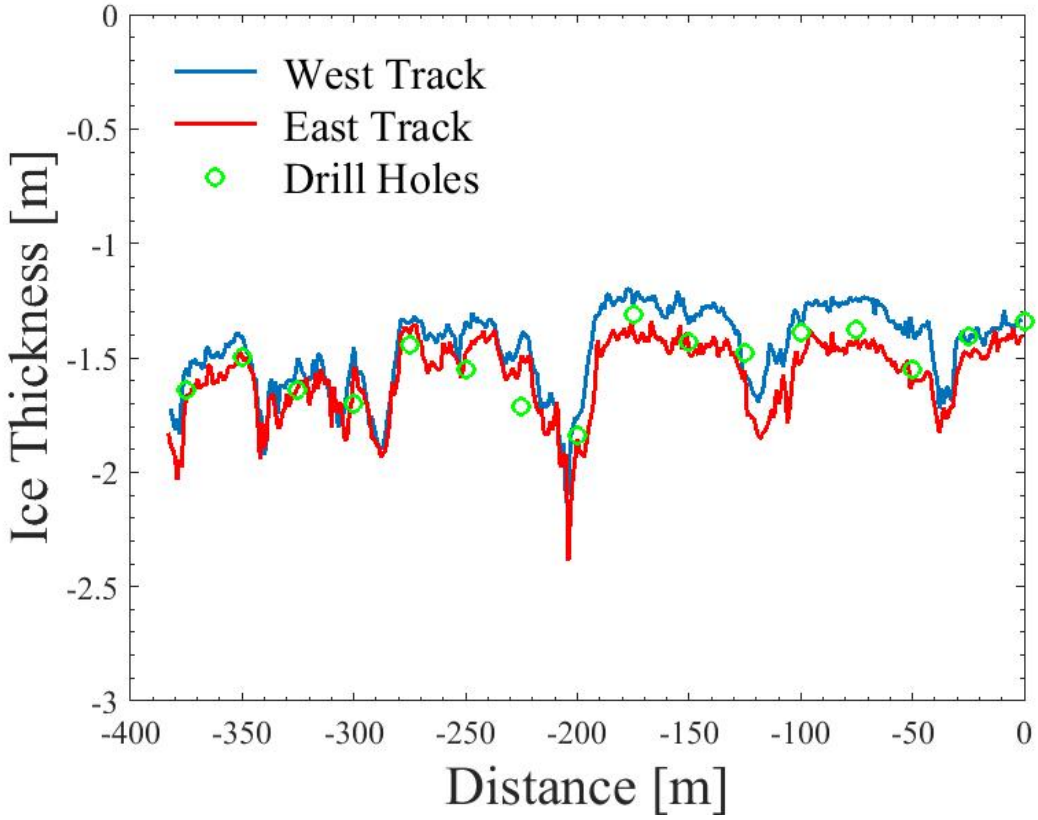

Figure 5-2. MATLAB plot of ice thickness profiles along survey line. In this plot, the modeled coefficients were used to develop ice thickness values from calculated Geonics EM31 values for the west and east directions along the survey line. This plot also displays drill hole thickness at the calibration points (green circles) along the survey line to serve as a comparison.

But there is a drawback to this non-linear regression method. As discussed in Chapter 2, this exponential fit, along with the modeled coefficients that have no geophysical meaning, are only valid for one instrument at a time. In other words, a whole new fit needs to be established for a different instrument that traversed the same path. Therefore, the next section focuses on a recently developed calibration approach to the non-linear method described in this section in order to provide an alternative path for calibrating more than one EM induction instrument of the magnetic-dipole type.

5.3 Alternative Calibration Method for EM Induction Instruments

As the previous section highlighted some of the shortcomings with an established calibration routine, this section explores an alternative calibration method that is purely based on electrical engineering, as well as geophysical, properties. Additionally, this alternative method has the ability to calibrate instruments in a consistent way to compare results between instruments with the same calibration procedure and dipole construct. To demonstrate how these properties can aid in the development calibration routine, the following information is given. First and foremost, the EM induction instruments measure apparent conductivity, which is comprised of the material conductivities below the instrument. Second, the EM induction instruments also have a measured coil spacing. Third, ice thickness is a measured quantity at drill hole calibration points. Fourth, the cumulative response functions are the multi-layer response to the secondary magnetic field from all material below a certain distance, and also account for the coil spacing. Additionally, as shown in Equation 2.6 and Equation 3.160, if the coil spacing is less than the skin

depth of the cumulative layers, then the contribution from each layer can be added independently [6]. Therefore, in a mathematical sense, expanding Equation 2.6 for a *n*-layered system can be expressed as

$$\begin{aligned}\sigma_a &= \sigma_1\left[1 - R(\zeta_1)_{HCP,VCP}\right] + \sigma_2\left[R(\zeta_1)_{HCP,VCP} - R(\zeta_2)_{HCP,VCP}\right] \\ &+ \sigma_n\left[R(\zeta_1)_{HCP,VCP} - \ldots - R(\zeta_{n-1})_{HCP,VCP} - R(\zeta_n)_{HCP,VCP}\right] + \sigma_{n+1}R(\zeta_n)_{HCP,VCP}\end{aligned}, \quad (5.5)$$

where σ_a is the apparent conductivity recorded by the EM induction instrument, all σ on the right-hand side of the equation represents the material conductivity at each layer, and $R(\zeta_n)$ is the cumulative response as a function of the *n*-th layer depth *z* divided by coil separation *r*, which is dependent on instrument configuration (HCP or VCP). Since the focus is on determining the thickness of sea ice, *n* in this case can be 2 because the investigation focuses on the responses from sea ice and seawater. Therefore, Equation 5.5 can be reduced to the following two-layer form:

$$\sigma_a = \sigma_1\left[R(\zeta_0)_{HCP,VCP} - R(\zeta_1)_{HCP,VCP}\right] + \sigma_2 R(\zeta_1)_{HCP,VCP}\ , \quad (5.6)$$

where $R(\zeta_0)$ is the cumulative response function for the space between the bottom of the instrument to the top of the surface under study (i.e., the carry height) divided by the coil spacing. Note that in Equation 5.5 that $R(\zeta_0)$ is equal to 1, but not in Equation 5.6. When $R(\zeta_0)$ is equal to 1, the instrument is placed directly on the surface under study. To translate Equation 5.5 physically, referring to Figure 2-5, and referring to the statements made about Equations 3.158-3.160, the material underneath the EM induction instrument is yielding 100% relative contribution to the secondary field at the receiver coil. However, when the instrument is at a certain carry height above the surface, it requires the use of its own response function since the relative contribution percentage will now be less than that compared to having the instrument placed on the surface.

Up to this point, the measured quantities for Equation 5.6 are known. The unknowns are the material conductivities at each layer, as well as the ice thickness itself. In order to address the calculation of the unknown material conductivities, a system of two equations, based on Equation 5.6, needs to be established to solve for two unknowns, such as

$$\begin{aligned} \sigma_a &= \sigma_1\left[R_{a0} - R_{a1}\right] + \sigma_2 R_{a1} \\ \sigma_b &= \sigma_1\left[R_{b0} - R_{b1}\right] + \sigma_2 R_{b1} \end{aligned} , \tag{5.7}$$

where σ_1 and σ_2 are the sea ice and seawater conductivities, respectively, R_{a0} and R_{b0} represent the height of the bottom of the instrument to the top of the ice (including snow thickness) divided by the respective instrument's coil spacing and are considered weighting terms, R_{a1} and R_{b1} represent the total thickness divided be the instrument's coil spacing, and σ_a and σ_b represent the apparent conductivity collected at different calibration points locations along the survey line.

At this point, one can define σ_2 as a function of σ_1 and vice versa since the set of equations in Equation 5.7 is linear. While the full solution of defining σ_1 and σ_2 is presented in Appendix D, the approach is outlined here. First, σ_2 is found by re-arranging terms such that σ_1 is in terms of σ_2. This arrangement allows σ_1 to be substituted back into the first equation in the set of Equation 5.7, combine terms, and solve for a final σ_2 solution. The same process occurs for defining a final equation for σ_1, but σ_2 is defined first. The final solutions for σ_1 and σ_2 can be stated as

$$\sigma_1 = \frac{\sigma_a R_{b1} - \sigma_b R_{a1}}{R_{a0} R_{b1} - R_{b0} R_{a1}} , \tag{5.8}$$

and

$$\sigma_2 = \frac{\sigma_a\left[R_{b0} - R_{b1}\right] - \sigma_b\left[R_{a0} - R_{a1}\right]}{\left[R_{a1} R_{b0} - R_{b1} R_{a0}\right]} . \tag{5.9}$$

Even though this outline is brief, and the detailed mathematics are in Appendix D, it begs the question of what do these relationships signify, and what is the difference between this approach and historical approaches, such as in [6]? First, notice that the solutions to these equations are paired solutions and require the use of location pairs. Location pairs represent the comparison of one instrument reading versus another instrument reading for apparent conductivity over a calibration point. Location pairs can be from either the EM31 or the EMP-400 at different points, the EM31 against itself (albeit in different directions on the survey line), or the EMP-400 against itself (again, in different directions on the survey line). With this ability, solutions can be developed while accounting for variability in instrument footprint among two physically different instruments such as the EM31 and EMP-400. Second, since the material conductivities are found, more than one EM induction instrument can be calibrated, which is an improvement over historical routines where only one instrument can be calibrated at a time. Third, these equations use all geophysical parameters in order to relate experimentally measured apparent conductivities from these instruments, as well as calibration point ice thickness and instrument carry height simultaneously to achieve material conductivity. Even though the material conductivities are defined here, the next section describes the conditions that need to be implemented to achieve valid numbers for both σ_1 and σ_2.

5.4 Establishing Valid Conditions

The last section defined material conductivities based on a linear system of two equations solved for two unknowns. This section details the process of determining if a particular material conductivity solution is valid or not. Before this process is started, many possible combinations exist for σ_1 and σ_2. To further explain these possible

combinations, there are 16 calibration points along the survey line as mentioned previously. A total of 4 transects were traversed: 2 for the EM31 in both directions (east and west), and 2 for the EMP-400 (east and west). From this information, there are a total of 64 calibration data points here (16 * 4 = 64) where measured apparent conductivity, as well as measured ice thickness, are known values. But since Equation 5.7 is an Equation set, comparison cases need to be made, such as EM31 "West" versus EMP-400 "West", EM31 "East" versus EMP-400 "West", etc. for a total of 64 possible cases. If these possible cases are multiplied by the combination of calibration points, then, with this current data set collected from Barrow, there a possible 4,096 total values for both σ_1 and σ_2 (since 64 * 64 = 4,096).

Now, these values represent the total possible solutions, but there could be some instances where the result is not valid. One possible example would be to have a negative conductivity value, which does not exist in sea ice and seawater mediums. Therefore, in order for both material conductivities to have physical meaning, both σ_1 and σ_2 have to be positive definite, such that

$$\sigma_1 = \frac{\sigma_a R_{b1} - \sigma_b R_{a1}}{R_{a0} R_{b1} - R_{b0} R_{a1}} > 0 \tag{5.10}$$

and

$$\sigma_2 = \frac{\sigma_a \left[R_{b0} - R_{b1} \right] - \sigma_b \left[R_{a0} - R_{a1} \right]}{\left[R_{a1} R_{b0} - R_{b1} R_{a0} \right]} > 0 \ . \tag{5.11}$$

However, there are additional conditions (or "flags") to ensure the validity of σ_1 and σ_2. From the literature, such as [1], seawater is more conductive than sea ice. So a third condition for this algorithm is

$$\sigma_2 > \sigma_1 \ . \tag{5.12}$$

To further reduce the possibility of having invalid values, in addition to those stated in Equations 5.10-5.12, the repeat location pairs where location "a" is equal to location "b" can be omitted. As an example, in matrix mathematics, this would represent the diagonal elements of the matrix, such as a_{11}, a_{22}, a_{33}, etc. In essence, the focus would be on a unit lower triangular matrix for the valid ranges of σ_1 and σ_2 [75]. Two other flags can be stated that ensure valid material conductivity values based on location pairs as well as the definitions of σ_1 and σ_2 themselves. The first flag is that the difference in apparent conductivities are positive definite, i.e.,

$$\sigma_a - \sigma_b > 0 \ . \tag{5.13}$$

The second flag ensures the differences in the calculated response curves of the total response between the bottom of the instrument and the bottom of the ice are also positive definite, expressed as

$$R_{a1} - R_{b1} > 0 \ . \tag{5.14}$$

There are two important remarks to be addressed at this point. First, an additional flag can be set to Equation 5.14 to ensure that it is above a certain threshold value, which is considered noise in the calculations, and demonstrates the sensitivity of the response curves (to be discussed with the results presented in Chapter 6). Additionally, these equations depend on how the data is "packed" into the algorithm. To explain, while comparing location pairs, if location "a" for one instrument is held constant while each of the location "b" readings change, then the above equations are valid. For example, if location "a" is the first calibration point for the EM31 in a particular direction (assume west in this example), location "b" would be the comparison value of all the other instruments, as well as the EM31 "West" values. Now, if the reverse were true,

such that location “b” were held constant while the location “a” readings change, then Equations 5.13 and 5.14 would have to be rearranged accordingly, such as

$$\sigma_b - \sigma_a > 0 \tag{5.15}$$

and

$$R_{b1} - R_{a1} > 0 \ . \tag{5.16}$$

Tables 5-4 and 5-5 provide this example, in column view, for a visual demonstration of how data “packing” works for this particular algorithm.

Sample Number [*N*]	Location “a”	Location “b”	σ_a [mS/m]	σ_b [mS/m]
1	1	1	222.75	222.75
2	1	2	222.75	209.00
3	1	3	222.75	215.25
4	1	4	222.75	237.25
5	1	5	222.75	219.25
6	1	6	222.75	191.25
7	1	7	222.75	220.25

Table 5-4. Sample of EM31 data array on western transect without flags applied. For this sample, Location “a” is the value of the first calibration point that the EM31 encounters. Location “b” is the same instrument, but the calibration point changes. Location “a” will be held constant until all other calibration points from all other instruments have been reported in location “b”. Equations 5.13 and 5.14 are valid when the data is “packed” in this manner.

Sample Number [N]	Location "a"	Location "b"	σ_a [mS/m]	σ_b [mS/m]
1	1	1	222.75	222.75
2	2	1	209.00	222.75
3	3	1	215.25	222.75
4	4	1	237.25	222.75
5	5	1	219.25	222.75
6	6	1	191.25	222.75
7	7	1	220.25	222.75

Table 5-5. Sample of EM31 data array on western transect without flags applied. For this sample, which is opposite of Table 5-4, Location "b" is the value of the first calibration point that the EM31 encounters. Location "a" is the same instrument, but the calibration point changes. Location "b" will be held constant until all other calibration points from all other instruments have been reported in location "b". Equations 5.15 and 5.16 are valid when the data is "packed" in this manner.

It should also be noted here that there were flags developed that failed, but also proved that there is a dependence on the numerator and denominator for the definitions of σ_1 and σ_2. For σ_1 these conditions are

$$\frac{R_{b1}}{\sigma_b} > \frac{R_{a1}}{\sigma_a} \tag{5.17}$$

and

$$\frac{R_{b0}}{R_{b1}} < \frac{R_{a0}}{R_{a1}} \ . \tag{5.18}$$

For σ_2 these conditions are

$$\frac{R_{b0} - R_{b1}}{\sigma_b} > \frac{R_{a0} - R_{a1}}{\sigma_a} \tag{5.19}$$

and

$$\frac{R_{b0}}{R_{b1}} < \frac{R_{a0}}{R_{a1}} \ . \tag{5.20}$$

The next section looks at the inverse solution to find an actual ice thickness based off of the definitions of σ_1 and σ_2 and implementing the conditions as discussed in this section.

5.4.1 Inversion Solution for Determining Ice Thickness

Now that the material conductivities have been quantified as a function of known values and conditions set to develop valid values, an ice thickness (Z_1) value can also be determined from these equations to compare to other methods, such as a non-linear regression approach [32-35]. The mathematics for defining the inverse solution are located in Appendix D, where the final result, developed from the cumulative response equations and the calculated material conductivities, is stated as

$$Z_1 = \frac{r\left(1 - R(\zeta_1)^2\right)}{4R(\zeta_1)} \quad . \tag{5.21}$$

To interpret Equation 5.21, focus on the cumulative response function, and notice that $R(\zeta_1)$ is the significant weighting term here. As stated before, $R(\zeta_0)$ is the response from the bottom of the instrument to the top of the surface under study. But $R(\zeta_1)$ is the response from the bottom of the instrument to the bottom of the first layer, which in this case is the sea ice. To show this difference between $R(\zeta_0)$ and $R(\zeta_1)$ along the cumulative response curve per Figure 2-5, a heuristic example plot is provided in Figure 5-3. Note that the curve is the same as Figure 2-5, but rotated in such a way to emphasize the difference between the two response value functions. In this example, the EM31 is used in VCP mode, with a coil spacing r of 3.67 m, and a carry height of 0.95 m, which would be characteristic of the parameters used to calculate $R(\zeta_0)$. For $R(\zeta_1)$, the coil spacing remains the same, but the thickness of the ice is 2.59 m. This

example shows that there is indeed a difference between the $R(\zeta_0)$ and $R(\zeta_1)$ terms, and the reasoning behind why Equation 5.21 is weighted by it.

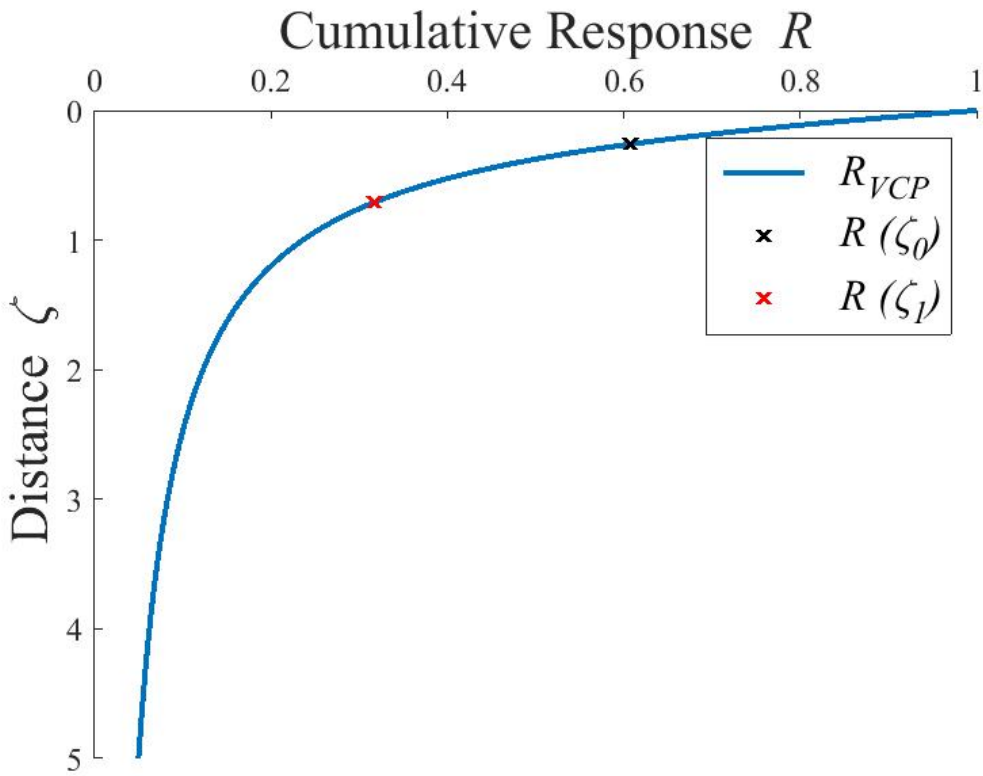

Figure 5-3. MATLAB plot the cumulative response function shown in Figure 2-5, albeit rotated for the purposes to demonstrate the differences of $R(\zeta_0)$ and $R(\zeta_1)$ terms. The black "X" is $R(\zeta_0)$, and the red "X" is $R(\zeta_1)$. Note here how the change in depth affects the response curve value, where $R(\zeta_1)$ indicates the response from the bottom of the instrument to the bottom of the sea ice.

5.5 Chapter Summary

This chapter established a co-calibration routine for magnetic dipole-type instruments based on data that was collected in a field exercise held in Barrow, Alaska. This developed routine varies from historical routines since it is based on geophysical properties, as well as enabling results to be formulated from two types of instruments that have different instrument footprints. The main premise behind the

routine is to calculate two unknowns, which are the material conductivities of sea ice and seawater, from a linear set of equations and lead to an actual thickness result. The ice thickness solution is an inverted solution developed from the cumulative response equations and the calculated material conductivities. The inversion solution depends on the response function since it is the total response from the bottom of the instrument to the bottom of the sea ice. Therefore, the theory presented in this chapter will be vital to the results achieved in Chapter 6.

Chapter 6

DEMONSTRATION OF CO-CALIBRATION ROUTINE

6.1 Central Objective

The previous chapter detailed how field collected apparent conductivity values can be related to thickness values by one method, that being a non-linear regression routine. However, this routine does have some disadvantages associated with it, such as only being able to calibrate one instrument at a time. In turn, Chapter 5 provided the mathematical basis for the development of a co-calibration routine for two magnetic dipole EM induction instruments. This routine was developed so that more than one EM induction instrument could be calibrated against known thickness values at calibration hole sites. The algorithm chosen is also based off of a two-layer system that involves the use of measured apparent conductivity values and calculated material conductivity values by way of an instrument's inherent response. Therefore, this chapter implements the theory and aims to answer the following question:

Can a co-calibration algorithm developed for two magnetic dipole EM induction instruments provide an ice thickness that is comparable to historical methods?

This question is answered by presenting a case study application of the algorithm discussed in Chapter 5 by focusing on the following areas. First, since the non-linear regression routine provided thicknesses for the EM31 instrument only, this chapter provides thicknesses for both instruments on all transects by way of using the linear regression method. Second, while the conditions set forth in Chapter 5 do

provide valid conductivity pairs, some of these answers may be affected by "noise", in a statistical sense, stemming from the sensitivity of cumulative response functions. Therefore, the concept of the signal-to-noise ratio, an important electrical engineering metric, is introduced and applied to solution pairs. Third, a statistical analysis of the valid solution pairs, after noise removal is considered, based on their geophysical traits. To clarify, even though the sea ice that was traversed in Barrow was stated to be flat, there are instances where the ice has some ridges when referring to Figure 5-2. These instances are referred to as "bumpy factors" and analyzed as such. Lastly, the co-calibration routine is used with two approaches, one using the means of the valid conductivity pairs, and the other using an error minimization scheme based on the sum of squares.

6.2 Linear Regression of Calibration Hole Ice Thickness

As stated previously, Chapter 5 provided a relationship, based on non-linear regression, that matched apparent conductivity values with ice thickness measurements at calibration hole sites for only two of the transects walked. However, in order to compare the co-calibration thickness results to the measured ice thickness at the drill hole sites of all 4 transects, a linear regression of the data was performed. Linear regression is a method to where the data is fit along a best-fit line. In the case of the transect lines walked in Barrow, each transect has there own best-fit line. The best-fit lines can be mathematically defined in slope-intercept form as

$$z_{total} = m * \sigma_a + b \tag{6.1}$$

where z_{total} is the total thickness of ice, snow thickness, and carry height of the instrument, m is the slope, σ_a is the apparent conductivity collected at the calibration hole, and b is the intercept. To find just the measured ice thickness, the snow thickness

and carry height are subtracted per Equation 5.4. To provide a best-fit line, each of the apparent conductivity values is plotted against the total thickness aforementioned at the calibration hole sites. Table 6-1 lists the equations for each of the transects. Note that the nomenclature of GSSI and EMP-400 used within this dissertation are the same instrument and are used interchangeably. Figure 6-1 shows the generated profile thickness for all 4 transects based on linear regression. Figure 6-2 shows each of the transect profile thickness with 95% confidence intervals. Note that these profile plots will show the ice thickness only, similar to Figure 5-2.

Transect	Equation
EM31 West	$z_{total} = -.0068*\sigma_a + 3.9156$
EM31 East	$z_{total} = -.0075*\sigma_a + 3.8830$
GSSI West	$z_{total} = -.0059*\sigma_a + 2.5746$
GSSI East	$z_{total} = -.0069*\sigma_a + 2.6521$

Table 6-1. Transects and their respective linear regression equations.

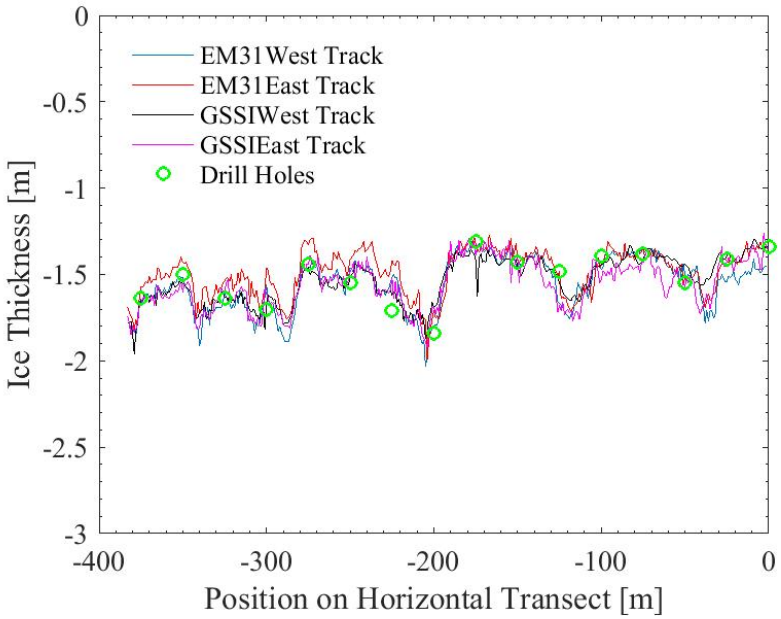

Figure 6-1. Profile thickness of all 4 transects traversed in Barrow. Plot generated using linear regression of the data. Green dots represent measured ice thickness at drill hole calibration sites.

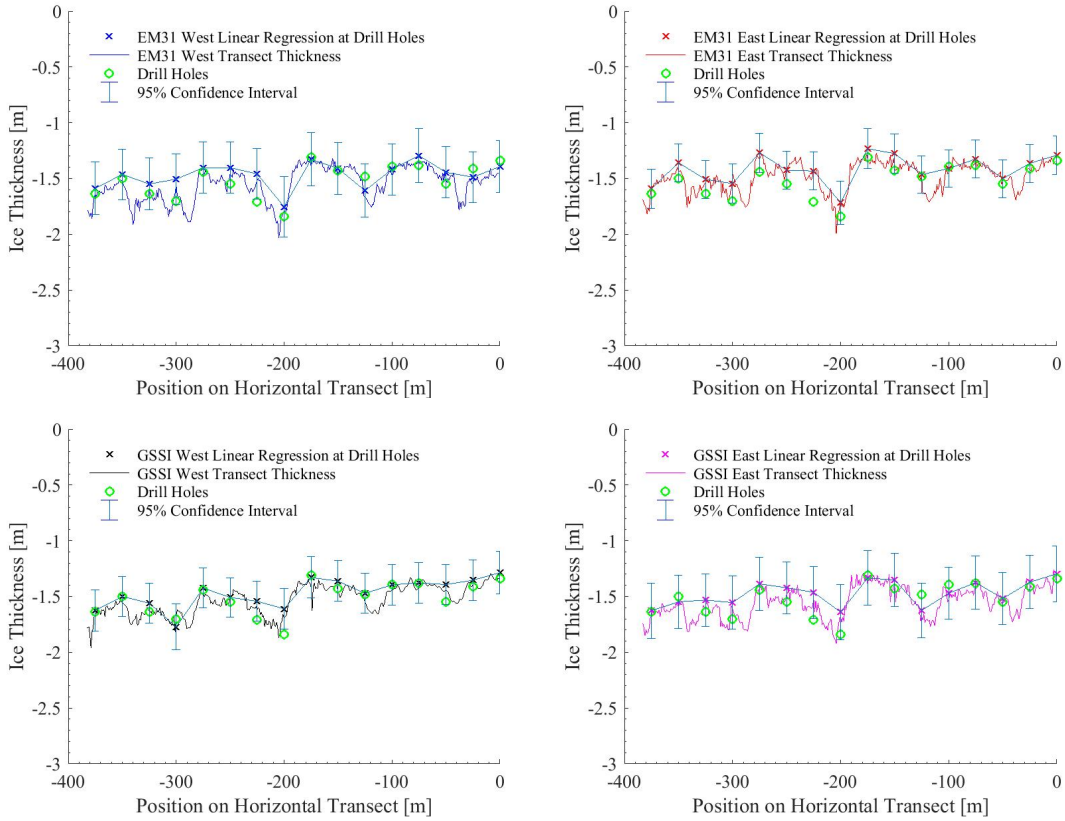

Figure 6-2. Individual transect profile thickness plots based on linear regression values and 95% confidence intervals of measured ice thickness at calibration sites. Clockwise from top left is the plot for EM31 West, EM31 East, GSSI East, and GSSI West.

6.3 Noise Analysis

To start the demonstration of the calibration routine developed in Chapter 5 between two different EM induction instruments, the noise in the solution pairs must be first considered. In Chapter 5, it was determined that the complete data set from Barrow yielded a possible 4,096 values between the data collected from the EM31 and the EMP-400. While the conditions, or "flags", defined in Chapter 5 reduce the possible combinations, the effect of noise is also present. The term noise, in a general sense, is customarily used to designate unwanted disturbances in signals [76]. Many

"noises" exist in this vein, such as atmospheric noise, thermal noise, electrical noise, and so on. In this calibration routine, the focus is on statistical noise present based on the calculated results and the conditions applied. One metric applied in the analysis of noise is the signal-to-noise ratio (SNR). The SNR is defined as the ratio of the measurement of a signal compared to the noise level of that signal. In a statistical sense, for this data set the SNR can be expressed as [77]

$$SNR = \frac{\mu_S}{\sigma_S} \ , \tag{6.2}$$

where μ_S is the sample mean and σ_S is the sample standard deviation, where both of these quantities are measured after the conditions/flags discussed in Chapter 5 are implemented. Based on Equation 6.2 and the values used per the conditions set in Chapter 5, the SNR for σ_1 is 1.82, and the SNR for σ_2 is 6.63. Typically, in an engineering environment, these numbers, since they are greater than one, indicate that there is more signal than noise for both material conductivities. For statistical analysis purposes, the higher the value of the SNR, the better quality in the data [77].

While the ratio provides a useful number to determine if there is more signal than noise, it does not say where the noise comes from. In order to determine where the noise arises, consider the differences in both cumulative response functions for the R_{a1} and R_{b1} functions against σ_1 and σ_2 separately. Recall that R_{a1} and R_{b1} are the response functions from the bottom of the instrument to the bottom of the ice, but at location "a" and location "b". When the differences between these two values are taken and plotted against each other, as shown in Figure 6-3, note that there are distinct "clusters" of data in two locations for both σ_1 and σ_2: (1) data values that range from approximately 0-0.05 on the difference scale, and (2) data values from approximately 0.1-0.2 on the difference scale. But look at the shape of the cluster. The

(1) cluster, denoted by red arrows in Figure 6-3 appears to be more random in shape when compared to the (2) cluster where the points are more concentrated and closer together. This random shape is statistical noise, and is due to the fact that the coil spacing of the comparison pairs in the (1) cluster is the same. Additionally, from Figure 6-3, one can estimate that this random shape alone would have a low SNR value because the values are approaching zero. For clarification, these "noisy" comparison cases in the (1) cluster are not part of the diagonal matrix as discussed in Chapter 5, but they are the same instrument compared against itself only at different points along the survey line. Since the points in the (1) cluster can be considered noise and since they possess a low SNR, they can be filtered out of the solution pairs below a certain threshold value (determined experimentally to be 0.12) because there is such a small difference between the results in the differences of the response functions on the cumulative response curve. When these pairs are removed, the SNR of the remaining solution pairs improves to 2.04 for σ_1 and 7.75 for σ_2. It is also noted that this noise can be shown as well when the differences of σ_a and σ_b are compared, but those results will be the same solution pairs that are affected by the cumulative response difference threshold value aforementioned.

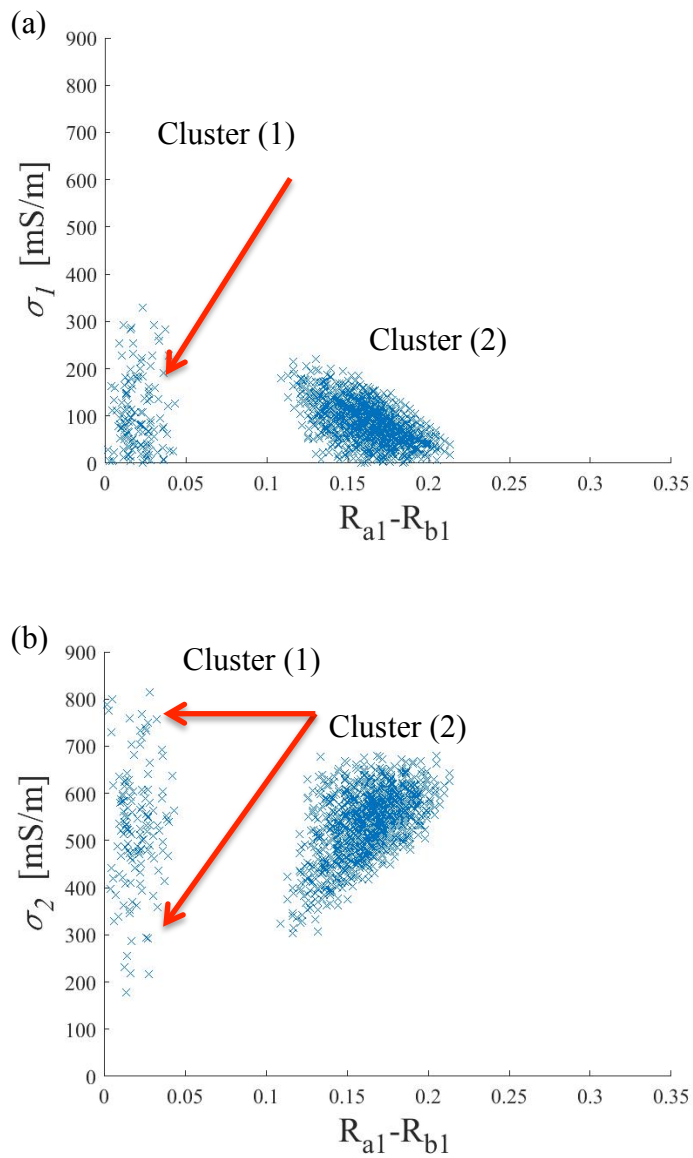

Figure 6-3. Noise analysis through the difference in response functions. R_{a1} and R_{b1} are the response functions from the bottom of the instrument to the bottom of the ice, albeit at different locations. The responses denoted by a red arrow indicate the noise present in the sample data. This noise is a result where the differences of the response curves are close to zero due to the same coil spacing being used in the solution sets. This figure shows the difference in response curves for (a) $\sigma 1$ and (b) $\sigma 2$.

6.4 Statistical Analysis of Chosen Calibration Values

To start with the statistical analysis of the values that satisfy the conditions aforementioned, consider a histogram plot shown in Figure 6-4. This particular histogram chart displays the number of occurrences for each possible solution for σ_1 and σ_2 per the conditions discussed in Chapter 5, and removing the noise as discussed in the previous section. With these histograms some insight can be made. Both histogram charts follow a general Gaussian "bell-shaped" curve, but it should be noted that the histogram for σ_2 is slightly skewed to the left under a normal distribution. To clarify, skewness is a measure of the asymmetry of a normal distribution, where the "tails" of one side of the distribution longer are than the other, such as the left tail for σ_2 distribution [78]. The histograms also report key statistical values, such as the sample mean, sample median, sample standard deviation, 25% quartile, 75% quartile, and the 95% confidence interval. The sample mean for σ_1 is 85.54 mS/m, and the sample mean for σ_2 is 536.66 mS/m. These values will be used when the ice thickness is computed. Additionally, the sample median for σ_1 is 82.90 mS/m, and the sample median for σ_2 is 543.99 mS/m.

The values achieved with the histogram chart can also be broken down by a "bumpy factor" of the ice when compared to σ_1, σ_2, and their location pairs with respect to the calculated ice thickness. Before the actual definition of the "bumpy factor" is disclosed, some geophysical clarifications need to be addressed. Recall that the measured transects in Barrow are flat ice. While that is true on the surface of the ice, underneath the ice, the structures can be very different. For example, there may exist such features like small pressure ridges and cracks, but without an underwater visual aid (such as a submarine or diver with a camera), the true structure of the ice is not known. As previously stated in Section 6.1, from Figure 5-2 it appears as though

there are some small ridges in the ice, especially in the mid-section of the survey line. Therefore, these small ridges can be characterized into a “bumpy factor” since the ice underneath the surface possesses small bumps, while exploring how the responses of σ_1, σ_2, and the location pairs are categorized based on the ice thickness of the transect. The “bumpy factor” can be broken down into four factor categories, ranging from 0 to 3 (or least “bumpy” to most “bumpy”), as shown in Figure 6-5. A factor of 0 indicates strictly flat ice without any sharp slopes or bumps. A factor of 1 indicates a slope that will result in a “bump”. A factor of 2 represents a small “bump,” where a 3 indicates a large “bump”. To explain further, the deepest point of the mid-section of the survey leg aforementioned would receive a value of 3, and the slopes on either side of that “bump” would receive a 1. Additionally, a factor of one would also be associated with the slopes of a small “bump”, or a factor of 2. Figure 6-5 shows box plots of the calculated material conductivities organized by their “bumpy factor” and their location. In the box plot, the blue rectangles represent the 25% (lower limit) and 75% (upper limit) quartile values. The red lines indicate the sample median. The red dots denote the sample mean. And the “whiskers” (black vertical dashed lines with horizontal solid lines at the end) are set to the range of the 95% confidence interval. Values outside of this range, shown with a red cross, are referred to as “outliers.”

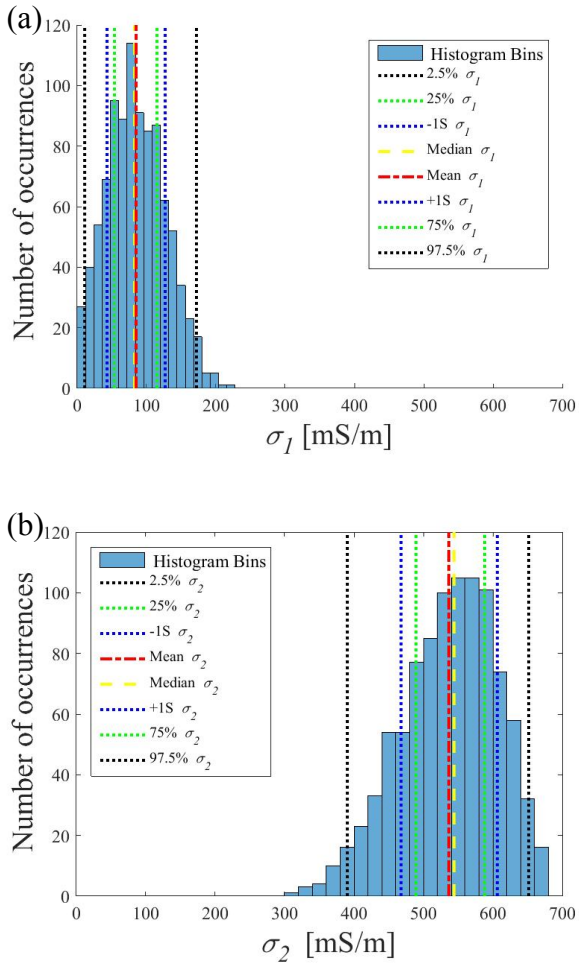

Figure 6-4. Histograms of calculated values for σ_1 and σ_2. Panel (a) shows the number of occurrences of values calculated for σ_1 based on conditions set forth in Chapter 5. Panel (b) is of the same format, but for calculated values of σ_2. In both plots the red dashed lines represent the calculated sample mean. The yellow dashed lines represent the calculated sample median. The black dotted lines represent the 95% confidence interval. The blue dashed lines represent the standard deviation, where "S" indicates a sample standard deviation. The green dashed lines represent the 25% and 75% quartile values, respectively.

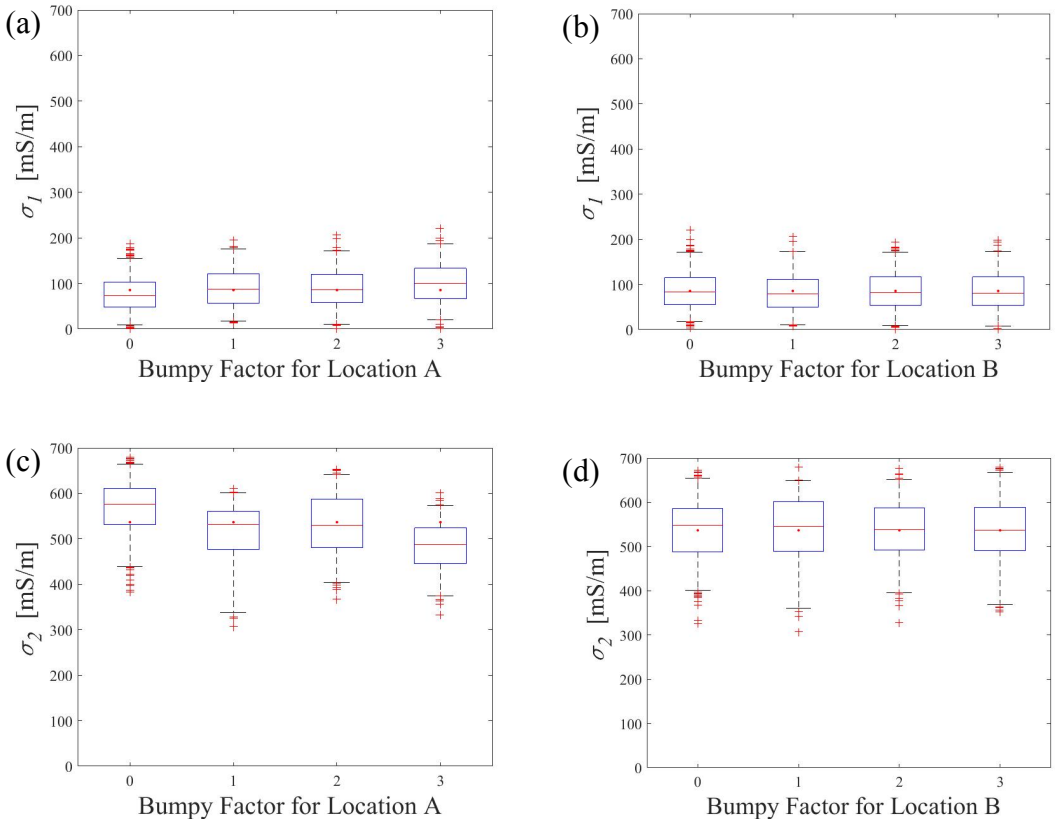

Figure 6-5. Boxplots of "bumpy factor" based on location pair and material conductivity. Here, the "bumpy factor" represents how smooth or rough the ice is based on a scale from 0 to 3, where 0 is considered smooth and 3 is rough. Panels (a) and (b) show the "bumpy factor" broken down in these categories for σ_1 based on its respective location pairing, and (c) and (d) are of the same format, but for σ_2.

6.5 Determination of Survey Line Ice Thickness with Co-Calibration Routine

6.5.1 Results Using Sample Means

Now that the results of σ_1 and σ_2 are established based on the conditions set forth in Chapter 5 and with the noise removed, one test conducted with the co-calibration algorithm was to use the sample means of the resultant data in combination with Equation 5.21 to determine absolute ice thickness. Using the mean is equivalent

to using a bulk conductivity value for sea ice and seawater, where the bulk conductivity value is provided by Archie's law. Archie's law can be stated mathematically as [33]

$$\sigma_i = \sigma_b V_b^m \ , \tag{6.3}$$

where σ_i is the bulk ice conductivity, σ_b is the brine conductivity, and V_b^m is the brine-volume fraction. Therefore, Equation 5.21 will be used four times since there were a total of 4 passes walked on the survey line. Recall though that the carry height for the Geonics EM31 is slightly different in the west and east directions. In the end, using this equation will result in an ice thickness plot similar to Figure 5-2.

However, before a plot is made, the uncertainty, or error propagation, also needs to be considered with these ice thicknesses since they are based on calculated material conductivity values. Since the sample means of σ_1 and σ_2 are already established, along with their respective sample standard deviation, the uncertainty can be calculated by the following equation [36], which is a slight modification in terminology to Equation 2.9, stated as

$$\Delta_{error} = \bar{x} \pm t * \left(\frac{s_{\sigma_{1,2}}}{\sqrt{n}} \right) , \tag{6.4}$$

where $\bar{x}$ is the sample mean, t is the t-distribution, $s_{\sigma 1,2}$ is the sample standard deviation of σ_1 and σ_2 (calculated separately), and n is the number of samples (valid values of material conductivities). The t-distribution is based on the 95% confidence interval and n-1 degrees of freedom. When Δ_{error} is calculated, it can be applied to Equation 5.21. But, Equation 5.21 also needs to have uncertainties established as well. To clarify, uncertainties exist with both the numerator and denominator of $R(\zeta_1)$, as well as Z_1. From certain relationships provided in [79, 80] the uncertainty in $R(\zeta_1)$ can be expressed mathematically as

$$\Delta R(\zeta_1) = \pm\sqrt{\left(\frac{\partial R(\zeta_1)}{\partial \bar{\sigma}_1}\Delta\sigma_1\right)^2 + \left(\frac{\partial R(\zeta_1)}{\partial \bar{\sigma}_2}\Delta\sigma_2\right)^2} \quad , \tag{6.5}$$

where

$$\frac{\partial R(\zeta_1)}{\partial \bar{\sigma}_1} = \frac{-R(\zeta_0)(\bar{\sigma}_2 - \bar{\sigma}_1) + (\sigma_a - \bar{\sigma}_1 R(\zeta_0))}{(\bar{\sigma}_2 - \bar{\sigma}_1)^2} \quad , \tag{6.6}$$

$$\frac{\partial R(\zeta_1)}{\partial \bar{\sigma}_2} = \frac{\sigma_a + \bar{\sigma}_1 R(\zeta_0)}{(\bar{\sigma}_2 - \bar{\sigma}_1)^2} \quad , \tag{6.7}$$

the Δ indicates an uncertainty of that value, and a bar above a value (i.e., $\bar{\sigma}_1$) indicates the mean of that value. Additionally, $\Delta\sigma_1$ can be defined as

$$\Delta\sigma_1 = \bar{\sigma}_1 - \Delta_{error,\sigma_1} \quad , \tag{6.8}$$

and, likewise, $\Delta\sigma_2$ can be defined as

$$\Delta\sigma_2 = \bar{\sigma}_2 - \Delta_{error,\sigma_2} \quad . \tag{6.9}$$

At this point, a "walkthrough" of these equations and results must be presented. When the uncertainty in $R(\zeta_1)$ is compared to the noise levels discovered in calculating the SNR when taking the difference of the response curves, the uncertainty here is comparable to the random noise levels. To clarify, the approximate noise levels with the difference in the response functions were stated to range between 0-0.05. The uncertainty calculations with Equation 6.4, when using information collected with both the EM31 and EMP-400 in both directions, averages a value of ±0.003, which is within the range of values in the differences of the $R(\zeta_1)$ response curve. Additionally, determining the uncertainty in $R(\zeta_1)$ also effects determining material conductivity since the material conductivity is dependent on the response functions themselves. In other words, having a low or high uncertainty at this point will affect the material conductivity result, and change the reported ice thickness determined from the

inversion solution. Taking this investigation further leads to the consideration of the uncertainties in Equations 6.8 and 6.9. Using the "means only" method, the uncertainties here are ±2.67 mS/m for σ_1 and ±4.41 mS/m for σ_2. If the noise values from Section 6.3 were left in, the uncertainties would increase to ±2.89 mS/m for σ_1 and ±4.77 mS/m for σ_2. Therefore, removing the noise does help in lowering the uncertainty in the calculated material conductivities. But do note that the uncertainty for σ_1 can have a considerable effect in calculations since the bulk conductivity of the sea ice is low per the literature.

Since the inversion solution for the ice thickness depends on $R(\zeta_1)$, which in turn depends on the calculated material conductivities as shown in Appendix D, the investigation leads to the uncertainty in the inversion solution itself. The uncertainty in Z_1 can also be expressed mathematically as

$$\Delta Z_1 = \pm\sqrt{\left(\frac{\partial Z_1}{\partial R(\zeta_1)}\Delta R(\zeta_1)\right)^2}\ , \tag{6.10}$$

where

$$\frac{\partial Z_1}{\partial R(\zeta_1)} = r\left(\frac{-R(\zeta_1)^2 - 1}{4R(\zeta_1)^2}\right)\ . \tag{6.11}$$

Based on these equations, this current "means only" approach can be visualized with all transects. Figure 6-6(a) shows the ice thickness according to an absolute calculation per equation 5.21 while subtracting the snow thickness and carry height (as does both the non-linear and linear regression routine). Table 6-2 provides the ice thicknesses at the drill hole locations only based on the transects plotted in Figure 6-6, where "old" refers to the non-linear regression method, and "new" refers to the routine developed in Chapter 5 using the means as discussed herein. From the perspective of the drill hole points, most of the data tends to be following an over/under thickness, as do both

regression methods. While some of the results overshoot considerably by 50% in ridged ice (the 200 m mark), the East direction numbers, especially with the EMP-400, overshoot drastically, even when there is no ridged ice present. Investigating this issue further, Figure 6-6(b) shows the ridged ice around the 200-meter mark (from 200 m to 210 meters), and Table 6-3 displays the thickness information for the 6 possibilities, similar to Table 6-2. Focusing on the 205-meter point, which is not a calibration point, the new method underestimates the non-linear regression method by a meter (approximately 100%), but the East overestimates this value by approximately 150% (with EM31 in the East) to nearly 375% overshoot with the EMP-400 in the East.

Again, the numbers aforementioned were absolute cases, where no uncertainty was considered. Now, the uncertainties previously discussed are added into Figure 6-7, through error bar plots, to present a more thorough answer. Both figures' results compare themselves to the Geonics EM31 transect ice thickness calculated shown in Figure 5-2 which used non-linear regression. The uncertainties ranged from approximately 0.02 m as a minimum to 59.75 m as a maximum. This large maximum uncertainty is due to a "spike" that occurs at the end of the transect shown in Figure 6-7(c). Excluding this "spike", while the absolute data, along with the uncertainties, does follow the same form as compared to the non-linear regression method and matches some of the calibration points, there is overshooting. These facts demonstrate that this routine displays a sensitivity to instrument footprint, especially at ridged locations with the EMP-400, as the results are amplified. This explanation is due to the difference in carry height used in the response functions when calculating the material conductivities (even though it was subtracted out of the final thickness result), and is also in line with what was witnessed with the simulation study in Chapter 4 with

changing geophysical parameters. However, this process is a first step in developing a robust algorithm that is based wholly on geophysical parameters.

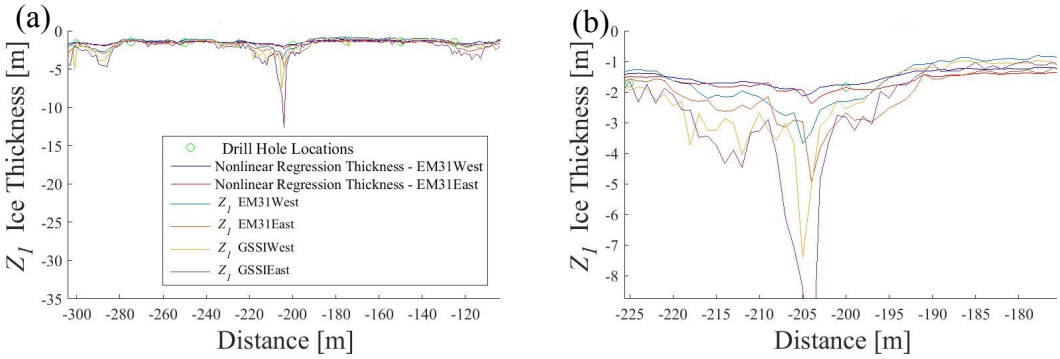

Figure 6-6. Plot of absolute ice thickness based on developed consistency routine. Panel (a) shows all transect thickness, including the transect thickness from the non-linear regression model per Figure 5-2, and panel (b) shows a "zoom-in" of panel (a) around the 200-meter mark. The "zoom-in" does show overshooting, especially with the GSSI instrument.

Drill Hole Location [m]	Measured Thickness [m]	EM31 West – Old [m]	EM31 East – Old [m]	EM31 West – New [m]	EM31 East – New [m]	GSSI West – New [m]	GSSI East – New [m]
0	1.34	1.33	1.42	1.13	1.39	0.93	1.09
25	1.41	1.43	1.54	1.37	1.7	1.04	1.9
50	1.55	1.39	1.54	1.25	1.7	1.19	1.9
75	1.38	1.24	1.45	0.91	1.47	1.11	1.46
100	1.39	1.36	1.66	1.19	2.07	1.18	2.11
125	1.48	1.57	1.43	1.74	1.42	1.59	1.89
150	1.43	1.35	1.48	1.17	1.56	1.20	1.16
175	1.31	1.27	1.38	0.98	1.29	1.11	1.25
200	1.84	1.77	1.69	2.32	2.16	2.55	2.89
225	1.71	1.40	1.51	1.29	1.64	1.95	2.28
250	1.55	1.34	1.46	1.15	1.5	1.40	1.62
275	1.44	1.34	1.77	1.15	2.42	1.25	2.99
300	1.7	1.45	1.63	1.42	1.96	2.43	3.92
325	1.64	1.50	1.81	1.55	2.52	2.04	3.69
350	1.5	1.50	1.58	1.55	1.83	2.04	2.31
375	1.64	1.55	1.83	1.67	2.6	2.14	3.42

Table 6-2. Thickness at drill hole calibration points with both calibration methods.

Distance [m]	EM31 West – Old [m]	EM31 East – Old [m]	EM31 West – New [m]	EM31 East – New [m]	GSSI West – New [m]	GSSI East – New [m]
200	1.77	1.85	2.32	2.68	2.55	2.82
201	1.76	1.94	2.31	3.00	2.28	2.77
202	1.80	2.02	2.44	3.30	2.84	3.65
203	1.85	2.16	2.59	3.85	3.11	4.86
204	2.04	2.39	3.30	4.93	5.11	12.68
205	2.13	1.93	3.68	2.97	7.42	8.38
206	1.87	1.92	2.67	2.92	3.69	7.09
207	1.90	1.98	2.77	3.14	3.02	6.10
208	1.86	1.96	2.63	3.05	3.57	4.06
209	1.78	1.69	2.38	2.16	3.23	2.89
210	1.71	1.74	2.16	2.32	2.68	3.27

Table 6-3. Thickness at ridged ice point per Figure 6-6(b).

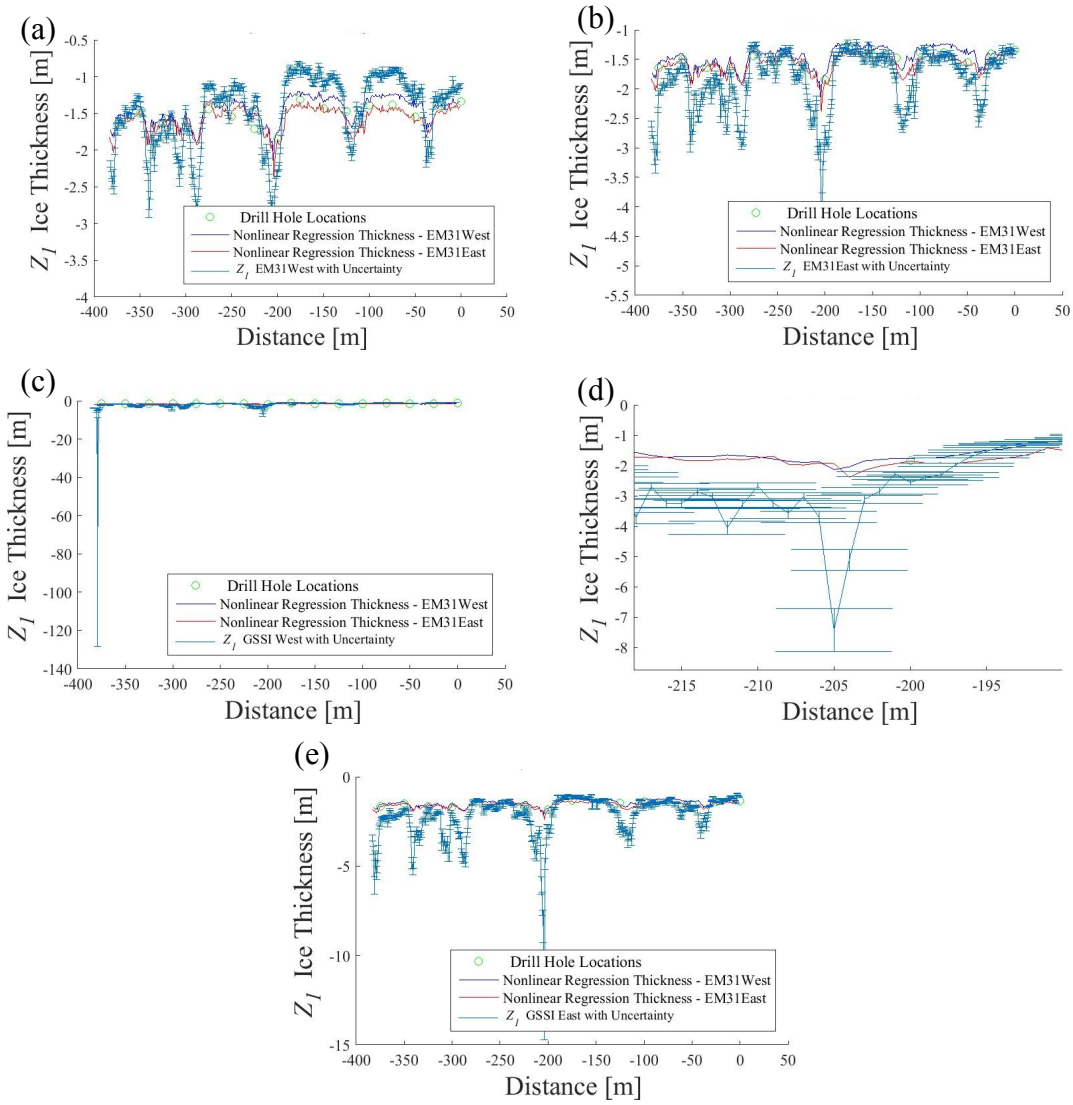

Figure 6-7. Plot of uncertainty in ice thickness for the consistency algorithm. Panels (a) and (b) are a direct comparison to the transect thickness per Figure 6-3(a) since the same instrument (Geonics EM31) is used. Panel (c) and (e) are of the GSSI, but panel (d) is a "zoom-in" of panel (c) due to a "spike" near the end of the transect in panel (c).

So what do these results mean? These results show that using just the sample means of the calculated σ_1 and σ_2 values as a sole calibration value will not result in a

viable solution. Additionally, this initial result proves that the conductivity in both the sea ice and seawater exhibits natural variability. This variability is shown in the histogram plots per Figure 6-4. This natural variability is also demonstrated in work per [81]. In this work, the study was conducted in the Antarctic using Wenner electrode arrays to measure the conductivity of ice core samples. At one part of the core sample (0.2-0.3 m), the conductivity was 31.25 mS/m. The next sample (0.3-0.4 m), the conductivity was 108.69 mS/m, which is roughly triple to the first sample reading. To put these values in perspective, Figure 6-8 takes a "cutaway" of the σ_1 histogram and highlights the values aforementioned in the work done by [81]. For this reason, the next subsection presents a minimization method based on the sum of squares method.

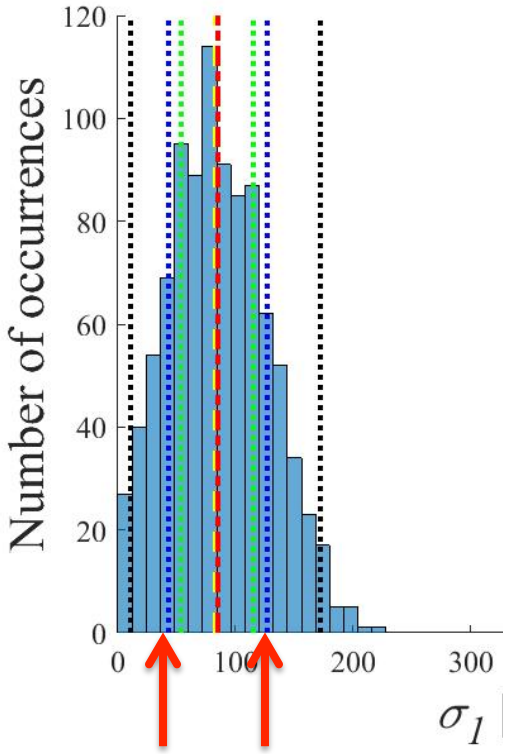

Figure 6-8. Histogram "cutaway" of Figure 6-4 to highlight conductivity values mentioned in [81]. The red arrows indicate the conductivity values of the core samples in [81] as they relate to the Barrow field data, but also highlight the fact of natural variability in conductivity levels.

6.5.2 Results Using Error Minimization

Since the usage of just the mean values of the calculated σ_1 and σ_2 values did not provide a "one size fits all" approach due to conductivity variability, another approach is to use error minimization. Here, the conductivity pairs from the conditions set forth in Chapter 5 and after noise removal (per section 6.3) are still utilized. The strategy here is to calculate the Z_1 thickness at the drill hole calibration sites per Equation 5.21 based on the valid conductivity pairs initially. Then, the next step is to

subtract the initial calculated Z_1 thickness at the drill hole locations from the physically measured ice thickness collected at the calibration hole to give the difference between the two. This result will comprise the residual sum of squares (RSS), which can be stated mathematically as [82]

$$RSS = \sum_{i=1}^{n} \left(y_i - f\left(x_i\right) \right)^2 \quad , \tag{6.12}$$

where, for this case, the predicted value y_i is the actual measured ice thickness at the drill hole sites, and the explanatory value x_i are the Z_1 thickness at the drill holes for a particular transect. The result from this formula is then applied again to Z_1, which, in turn provides a new thickness. The results of this new method are shown in Figure 6-9 for all transects compared to linear regression values.

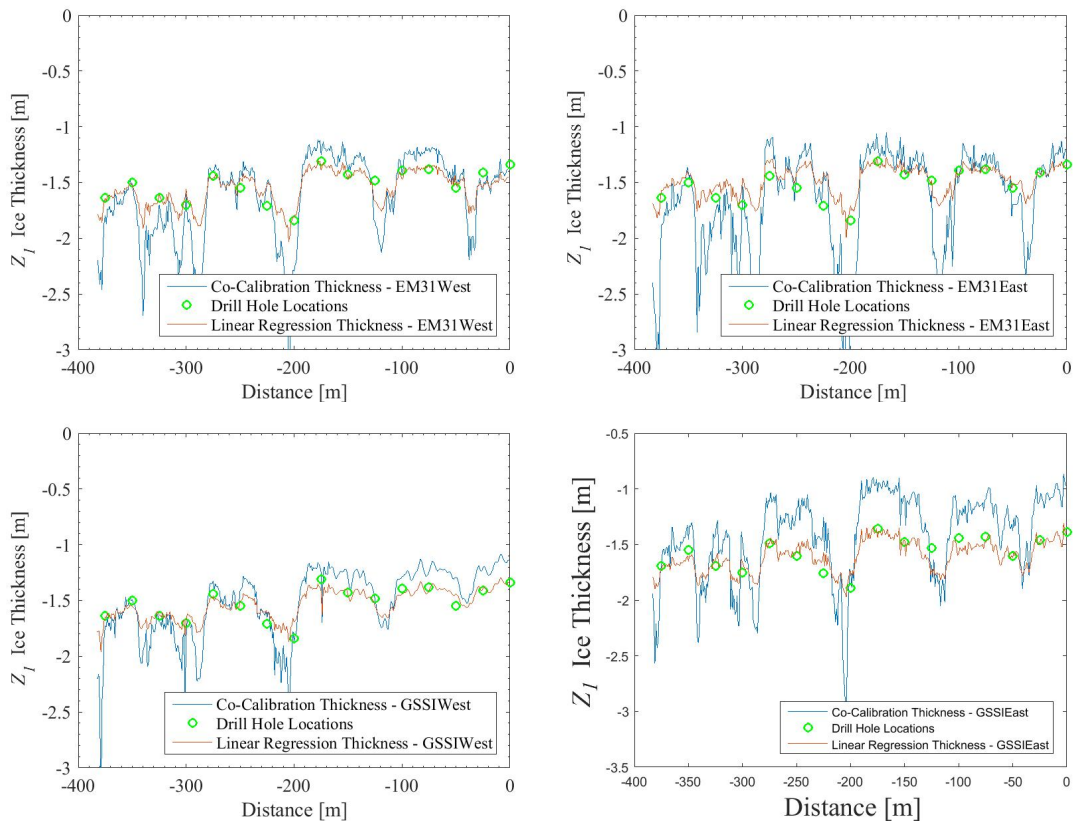

Figure 6-9. Profile thickness calculated from co-calibration algorithm based on error minimization scheme. Clockwise from top left are the following transects, EM31 West, EM31 East, GSSI East, and GSSI West. Green dots in each plot denote measured ice thicknesses at drill hole locations.

Given these plots are based on absolute values (i.e., no uncertainties yet), the relative error for this method can also be calculated. Relative error can be defined mathematically as [83]

$$\delta x = \frac{\Delta x}{x} \quad , \tag{6.13}$$

where Δx is the absolute error, and x is the actual value. Δx can also be expressed as a percentage, expressed as

$$\%\delta x = \overline{\delta x} * 100 \quad , \tag{6.14}$$

where $\overline{\delta x}$ is the mean of the relative error. Table 6-4 lists the relative errors for each of the transects based on the co-calibration routine. The instruments used in the West directions have less than 10% relative error, but the East directions have significant relative error, even though most of the drill hole quantities are closely aligned with the co-calibration thickness profile quantities.

Transect	Relative Error (%)
EM31 West	9.58%
EM31 East	33.40%
GSSI West	9.64%
GSSI East	22.27%

Table 6-4. Relative errors for all 4 Barrow transects.

In order to further explore the uncertainty based on this minimization scheme, the approach presented in Section 6.5.1 is used, but slightly adjusted. Equations 6.5-6.10 can now be stated as

$$\Delta R(\zeta_1) = \pm\sqrt{\left(\frac{\partial R(\zeta_1)}{\partial \sigma_{1,\min}}\Delta\sigma_1\right)^2 + \left(\frac{\partial R(\zeta_1)}{\partial \sigma_{2,\min}}\Delta\sigma_2\right)^2} \quad , \tag{6.15}$$

where

$$\frac{\partial R(\zeta_1)}{\partial \sigma_{1,\min}} = \frac{-R(\zeta_0)(\sigma_{2,\min} - \sigma_{1,\min}) + (\sigma_a - \sigma_{1,\min} R(\zeta_0))}{(\sigma_{2,\min} - \sigma_{1,\min})^2} \tag{6.16}$$

$$\frac{\partial R(\zeta_1)}{\partial \sigma_{2,\min}} = \frac{\sigma_a + \sigma_{1,\min} R(\zeta_0)}{(\sigma_{2,\min} - \sigma_{1,\min})^2} \ , \tag{6.17}$$

and

$$\Delta\sigma_1 = \sigma_{1,\min} - \Delta_{error,\sigma_1} \tag{6.18}$$

$$\Delta\sigma_2 = \sigma_{2,\min} - \Delta_{error,\sigma_2} \ , \tag{6.19}$$

where $\sigma_{1,min}$ and $\sigma_{2,min}$ are based on the minimum error calculated with Equation 6.12. Additionally, for this minimization scheme, Equation 6.4 can be restated as

$$\Delta_{error} = \delta x \pm t * \left(\frac{s_{\sigma_{1,2}}}{\sqrt{n}} \right) . \tag{6.20}$$

The uncertainties using the minimization method ranged from 0.25 m at a minimum to 5.41 m at a maximum, once again occurring in the East direction with the large "spike" occurring at about the center of the transect. Figure 6-10 displays all 4 transects with their respective Z_1 uncertainties, based on Equation 6.10, plotted. Table 6-5 compares the measured ice thickness at the drill hole calibration points to the values calculated with the minimization scheme at those same locations at all 4 transects.

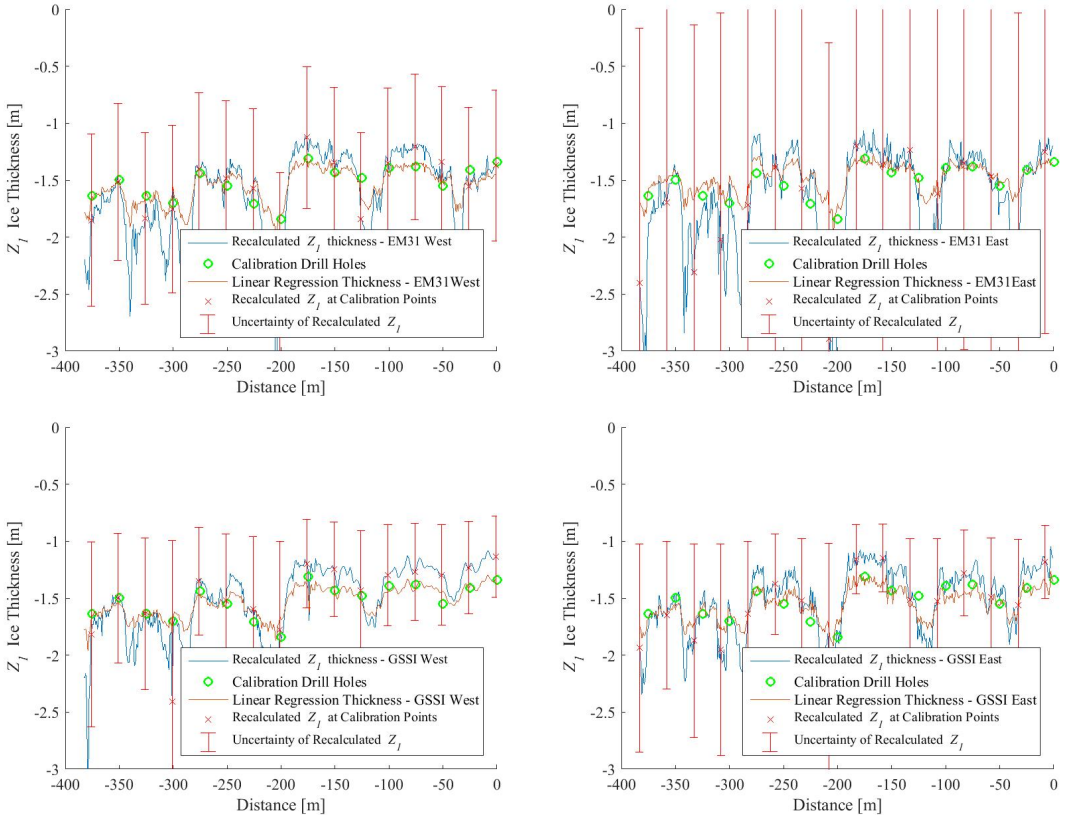

Figure 6-10. Uncertainty plots of all 4 transects using minimization. Clockwise from top left are the plots of the following transects: EM31 West, EM31 East, GSSI East, and GSSI West. These plots contain the profile thickness of the co-calibration routine that uses minimization and the respective uncertainties at calibration sites as error bars, as well as the linear regression profile thickness as a reference. Green circles represent actual measured ice thickness at calibration points.

Calibration Hole Location [m]	Measured Ice Thickness [m]	EM31 West [m]	EM 31 East [m]	GSSI West [m]	GSSI East [m]
0	1.34	1.37	1.20	1.14	1.15
25	1.41	1.56	1.40	1.21	1.26
50	1.55	1.47	1.69	1.29	1.51
75	1.38	1.19	1.24	1.24	1.26
100	1.39	1.42	1.49	1.29	1.42
125	1.48	1.85	1.58	1.50	1.75
150	1.43	1.40	1.38	1.30	1.23
175	1.31	1.25	1.16	1.25	1.20
200	1.84	2.29	2.49	1.87	1.79
225	1.71	1.50	1.40	1.65	1.40
250	1.55	1.39	1.38	1.41	1.33
275	1.44	1.39	1.18	1.33	1.28
300	1.70	1.60	1.53	1.83	1.58
325	1.64	1.70	1.77	1.69	1.53
350	1.50	1.51	1.42	1.50	1.57
375	1.64	1.80	1.88	1.73	1.76

Table 6-5. Comparison of the minimization ice thickness values versus the measured ice thickness at drill hole sites.

Even though the minimization scheme does improve the results from the "means only" approach, there are still differences overall, which can be attributed to both instrument footprint and variability in conductivity. Based on the results of the "means only" approach, the error minimization scheme, and the work per [81], highlighted in Table 6-6, the ice conductivity is still highly variable for a "one size fits all" approach.

Co-Calibration Method/Calculated Conductivity Pairs	Wenner array as per [81]
Mean σ_1 of all calculated pairs – 85.54 mS/m	σ_{ice} at 0.2-0.3 m core depth – 31.25 mS/m
σ_1 in minimization for EM31 West – 77.51 mS/m	σ_{ice} at 0.3-0.4 m core depth – 108.69 mS/m

Table 6-6. Example of variability in sea ice conductivity of various methods.

6.6 Chapter Summary

This chapter demonstrated an analytical study based on the co-calibration routine that was developed in Chapter 5. This study consisted of a noise analysis, a statistical analysis, and a comparison of two approaches to use with the co-calibration routine. The results demonstrate two key points: calibration of this instrument is affected by instrument footprint, and material conductivity exhibits natural variability such that using a bulk conductivity number like the "means only approach" will not be a good fit. Additionally, using the same instruments for generating valid conductivity pairs contributes to statistical noise in the algorithm, and are not considered in the final results.

To summarize, calibration to one number does not provide the thickness results that one expects in a real-world environment. As a best field practice, two different instruments with different footprints need to be used to address the natural variability of material conductivity in geophysical composites such as sea ice and seawater. Another possible best field practice would be that apparent conductivity data should be collected when the instrument is on the ground in addition to carrying the EM induction normally, as this would compare the effects of variable carry height with

regard to the response functions. While this new approach does need to be improved, it is on its way to becoming more robust so that it can be implemented as a new best field practice in Arctic environments to aid in measuring sea ice thickness.

6.7 Future Considerations

This chapter establishes that the co-calibration routine can be developed into a robust algorithm given some fine-tuning and further study into the variability of material conductivity. Beyond that, there are more possibilities. Even though the survey leg used in Barrow was considered to be flat ice, there were some small ridges (or "bumps") in the ice, which is shown in the transect thickness plots across all methodologies. Here, optimization of the response functions could be used to better align "bumpy" ice so that the co-calibration routine increases accuracy. Optimization of the response functions can also be applied to variable carry height as the routine improves. Additionally, the co-calibration algorithm only looked at values based on the VCP configuration since this was the orientation used with the field instrument in Barrow. Therefore, in order to expand the scope of the consistency algorithm, these two possibilities (optimization over ridges/variable carry height and dipole configuration) can be further investigated.

Another possibility would be to test the consistency algorithm on magnetic dipole type EM instruments that are not ground based, i.e., airborne EM units. Airborne units, such as those found in [29], use the same concepts as EM units used on the ground. The only difference here would be the height of the instrument used in the calculations of the response functions. However, the response functions of airborne units vary to those used on the ground, such that a minor substitution of terms cannot be used. Even though this possibility would be further "down the road" when

compared to investigating how the HCP configuration compares to VCP configuration data, and how the routine behaves over true-ridged ice, it still warrants a further look to increase the applicability of the algorithm as a whole.

Chapter 7

CONCLUSION

The work presented in this dissertation used sea ice as a geophysical test material to explore how electromagnetic responses interact with low-induction-number composite materials as a function of instrument footprint size and shape. In turn, this dissertation details new, original, and interesting aspects with respect to the study of sea ice with regard to improving the accuracy of its measurement as well. While the focus with developing these new aspects centered on using EM induction instruments, more importantly, however, this dissertation answered the following scientific question:

How can different aspects of geophysical composite properties, such as material conductivity, be used to improve the accuracy of sea ice thickness measurements based on numerical-modeling techniques and electromagnetic induction field instruments?

This dissertation answered this question with two objectives, restated here:

3) Objective 1 – Simulate field excitations of level and deformed sea ice with a 3D full-physics heterogeneous model in order to analyze field responses of multiple geophysical composite materials.
4) Objective 2 – Develop a co-calibration algorithm among different EM induction instruments based on ground truth thickness data collected from a field excursion in Barrow, Alaska, during 2013.

The objectives were met in Chapter 4-6, but with necessary background information presented in Chapters 1-3. However, this conclusion chapter will focus on how the objectives were met in Chapters 4-6 since they present the most original work.

To start, Chapter 4's scientific question was stated as:

How sensitive is an instrument footprint to a material conductivity change when a low-conductive material is surrounded by a stronger conductive material? The numerical model study in Chapter 4 met Objective 1 in the following ways. First, the APhiD model is a heterogeneous three-dimensional, full-physics numerical model that allows a user to simulate various geophysical scenarios with certain excitation parameters, and computes the fields everywhere inside a model volume. The output of these electromagnetic interactions can then be visualized in 3D rendering software, such as ParaView. For the purposes of this dissertation, in order to define the model volume, several ice cases were considered. First, the control runs of air-seawater only, followed by air, 3 m of sea ice, and seawater provided a necessary background response field for the more complex model simulations, which involved ridged ice. The ridged ice scenarios involved changing the conductivity makeup of the sea ice, as well as identifying the effects of locating the transmitter, with respect to the ridge, had on the electromagnetic field responses. While these first runs were simulated in HCP mode, VCP mode was also discussed.

But is instrument footprint impacted at all from the interaction between an induction instrument and the conductivity makeup of the ice? The answer to this question is yes, and the output from the simulations clearly shows some interesting features relating to instrument footprint. The footprint width L, defined in Chapter 4, changes based on material conductivity, as first noticed when flat ice was introduced

to the air-seawater only case in the control runs. The footprint is also sensitive to the transmitter's location, as well as its orientation. As far as instrument orientation is concerned, it appears that the footprint width does increase in size when the EM induction instrument is in the VCP orientation. This result is shown in Figure 4-10, where a numerical value comparison between HCP and VCP cases is provided.

In order to visualize how null line width can change, an important aspect of the modeling study included defining "null lines". Null lines are polarity changes in the magnetic field. The shape of the null lines is also affected by transmitter position, as well as the geophysical and electromagnetic properties of the sea ice. The same can be said for the magnetic flux lines and the current density lines as well. However, the null lines help to define the shape of a "kink," where a kink is the pronounced bend in the null line shape. The kinks occur at material boundaries. Opposite of the case with the null line width L, kinks are not sensitive to instrument orientation, as they still result at a material discontinuity as shown in Figure 4-10.

To conclude, footprint size and shape of pulses from EM induction instruments are not constant over sea ice due to natural variability in the material conductivity of sea ice and seawater. As a result of this model study, a best field practice here is that the accuracy of sea ice thickness measurements will be improved by taking into account sensitivity to instrument footprint size and shape created from interactions between EM pulses and horizontal "skin depth". The model study demonstrates the need for this best since the results display unanticipated aspects when compared to prior 1D level-earth models.

Objective 2 was met in Chapters 5 and 6, where a new co-calibration algorithm was defined in Chapter 5 based on field collected quantities, and Chapter 6 provided an analytical study of the new algorithm. Chapter 6's scientific question was:

Can a co-calibration algorithm developed for two magnetic dipole EM induction instruments provide an ice thickness that is comparable to historical methods?

In order to answer this question, there were two initial steps that needed to take place before a new method could be developed. First, field collected data was needed to make a comparison between new and historical methods, which was provided from a field exercise in Barrow, Alaska. Second, in keeping with a comparison theme, the collected data needed to be translated to ice thickness with a historical routine, which, for this dissertation, was based initially on non-linear regression, then subsequently followed by linear regression to provide a profile thickness for all 4 transects.

Since the thickness results were achieved with these historical routines, a closer look at some of the disadvantages associated with these methods needs to be discussed. The regression fits used coefficients to fit the data to a curve (for non-linear regression) or a line (for linear regression). But these coefficients were not based on any geophysical parameters. Instead, they were purely guesses that could be tuned to adjust the curve so that it could better fit the data. In the case of non-linear regression, another key drawback is that it only fit one curve to a singular EM induction instrument. Different guesses, and therefore a different curve, would need to be established for each instrument used. Linear regression also needs a separate fit for each transect traversed.

Therefore, with the goal of being able to calibrate more than one EM induction instrument at a time, a closer look focused on the cumulative response functions since they are geophysically-based parameters. Even though the response functions are sensitive to instrument orientation, the curves of the response functions are the same shape regardless of the instrument used. Additionally, the response functions can be used in layered systems, and can determine values such as material conductivity or thickness if some parameters are known. So, if two equations, based off of Equation 5.6, can be considered, then the material conductivities of the sea ice and the seawater can be defined, and an ice thickness established. This set of equations inherently solves two unknowns with two equations.

There are key benefits to using the developed algorithm as compared to historical routines. First, as stated previously, all parameters are geophysically based. Second, two instruments can be calibrated to provide an ice thickness based on location pairs. These traits alone eliminate the need to adjust a best-fit curve on coefficients as per non-linear regression, as well as defining more than one curve as previously mentioned. But most importantly, the instrument footprint of both of two different EM induction instruments is accounted for when using this method. While the results of the response function calculations will be different because of the different physical characteristics, the response curve information stays constant.

Chapter 6 provided a study of this routine to see how it compared to regression models. First, a noise analysis showed that where the coil separation is the same in the resulting solution pairs generates random noise, and therefore these solutions can be removed. Second, geophysical features of the survey line were broken down into "bumpy factors" and given a statistical analysis when compared to material

conductivities. Lastly, the inversion solution to provide ice thickness was calculated and an uncertainty study conducted. Here, two approaches are presented: a “means only” approach that uses the mean value of the valid conductivity pairs calculated per the conditions established in Chapter 5, and another approach based on error minimization. The results of both methods are compared to the actual drill hole calibration points, as well as the non-linear regression thickness plot shown in Figure 5-2 (for the “means only” approach) and the linear regression profile thicknesses as well (for the error minimization approach). The results with the co-calibration routine from both approaches are comparable to those established with the regression methods in the fact that the same transect “waveform” shape was followed, i.e., when a ridge was present, both approaches used with co-calibration routine and the regression methods agreed on the result. However, the co-calibration routine tends to overshoot with both approaches. An explanation of this overshooting is due to the sensitivity of instrument footprint, as well as the variable nature of the conductivity in the sea ice and seawater. Therefore, using one number as a calibration metric does not suffice in providing thickness results.

A better field practice in this case includes using two different instruments with different footprints to address the variability in conductivity. Other possible best practices that can improve this routine are making multiple apparent conductivity measurements at the same locations (preferable at calibration points) and having the instrument sit on the surface of the ice to remove the variability in carry height for a comparison. Additionally, another key best practice is the ordering of how location pairs are entered into the algorithm, known as “packing” the data. As mentioned in Chapter 5, depending on how the data is fed into the algorithm with regard to location

pairs, both Equations 5.13 and 5.14 can be implemented, or Equations 5.15 and 5.16 can be implemented (along with Equations 5.10-5.12, regardless of the order of location pairing). These equation pairs cannot be interchanged with each other (e.g., Equation 5.13 and Equation 5.16 cannot be used together), as it will cause the algorithm to not output correct results.

As a final point to this conclusion, the hope here is that the results achieved can lead to not only the implementation of better field practices mentioned in this chapter, but also better instrumentation to measure these quantities. While EM induction instruments are only one instrument out of many that are used in the arena of measuring sea ice, they are an important component. The results presented in this dissertation, along with the future work outlined in the chapters within this dissertation, will improve the accuracy of sea ice thickness measurements and simulations.

REFERENCES

[1] C. Haas and M. Druckenmiller, "Ice thickness and roughness measurements," in *Field Techniques for Sea Ice Research*, H. Eicken, R. Gradinger, M. Salganek, K. Shirasawa, D. Perovich, and M. Leppäranta, Eds., University of Alaska Press, 2009, pp. 62-68.

[2] National Snow and Ice Data Center, " All about sea ice – Salinity and brine," https://nsidc.org/cryosphere/seaice/characteristics/brine_salinity.html, 2016.

[3] W. F. Weeks and S. F. Ackley, "The growth, structure, and properties of sea ice," in *The Geophysics of Sea Ice*, N. Untersteiner, Ed., Plenum Press, 1986, p. 72-83.

[4] C. Kemker, "Conductivity, salinity and total dissolved solids," *Fundamentals of Environmental Measurements*, Fondriest Environmental, Inc., March 2014. Available: http://www.fondriest.com/environmental-measurements/parameters/water-quality/conductivity-salinity-tds/

[5] Antarctic Climate and Ecosystems CRC, "Sea ice physics and ecosystem experiment (SIPEX) – How do electromagnetic induction devices work?" 2007. Available: http://www.sipex.aq/access/page/index.html%3Fpage=92ba0e1a-c9dc-102a-8ea7-0019b9ea7c60.html

[6] J. D. McNeill, "Technical Note TN-6: Electromagnetic Terrain Conductivity Measurement at Low Conduction Numbers," Geonics Limited, October, 1980.

[7] W. E. Wightman, F. Jalinoos, P. Sirles, and K. Hanna, "Application of geophysical methods to highway related problems," Federal Highway Administration, Central Federal Lands Highway Division, Lakewood, CO, Publication No. FHWA-IF-040-21, September 2003. http://www.cflhd.gov/resources/agm/ and http://www.epa.gov/esd/cmb/GeophysicsWebsite/pages/reference/methods/Surface_Geophysical_Methods/Electromagnetic_Methods/Frequency_Domain_Electromagnetic_Methods.htm.

[8] W. F. Weeks, *On Sea Ice*, Fairbanks, University of Alaska Press, 2010, p. 20-25.

[9] A. Kovacs, N. C. Valleau, and J. S. Holladay, "Airborne electromagnetic sounding of sea ice thickness and sub-ice bathymetry," *Cold Reg. Sci. Technol.* **14**(3), 289-311 (1987). doi: 10.1016/0165-232X(87)90021-8

[10] A. Kovacs and R. M. Morey, "Sounding sea ice thickness using a portable electromagnetic induction instrument," *Geophys.* **56**(12), 1992-1998 (1991). doi: 10.1190/1.1443011

[11] T. R. Karl, J. M. Melillo, and T. C. Peterson, Eds., *Global Change Impacts in the United States*, Cambridge University Press, 2009, p. 141-143.

[12] A. Kovacs, "A study of multi-year pressure ridges and shore ice pile up," APOA Project Report 89, Hanover, NH, 1975, 45 p.

[13] A. Kovacs and M. Mellor, "Sea ice pressure ridges and ice islands," Technical Note TN-122, Creare Inc., Hanover, NH, 1971, 127 p.

[14] National Aeronautics and Space Administration, "Satellites show Arctic literally on thin ice," http://www.nasa.gov/topics/earth/features/arctic_thinice.html, April 2009.

[15] National Snow and Ice Data Center, " All about sea ice – Environment: operations," http://nsidc.org/cryosphere/seaice/environment/human_operations.html, 2013.

[16] T. Vihma, "Effects of Arctic sea ice decline on weather climate: A review," *Surv. Geophys.* **35**(5), 1175-1214 (2014). doi: 10.1007/s10712-014-9284-0

[17] S. W. Laxon, K. A. Giles, A. L. Ridout, D. J. Wingham, R. Willatt, R. Cullen, R. Kwok, A. Schweiger, J. Zhang, C. Haas, S. Hendricks, R. Krishfield, N. Kurtz, S. Farrel, and M. Davidson, "CryoSat-2 estimates of Arctic sea ice thickness and volume," *Geophys. Res. Lett.,* **40***(4),* 732–737 (2013).

[18] B. E. Schutz, H. J. Zwally, C. A. Shuman, D. Hancock, and J. P. DiMarzio, "Overview of the ICESat mission," *Geophys. Res. Lett., **32**(21), L21S01 (2005).*

[19] D. Fissel, R. Chave, and J. Buermans, "Real-time measurement of sea ice thickness, keel sizes and distributions and ice velocities using upward looking sonar instruments," *MTS/IEEE Biloxi - Mar. Technol. Future: Global Local Chall., OCEANS*, 2009.

[20] J. R. Rossiter and J. S. Holladay, "Ice-thickness measurement," in *Remote Sensing of Sea Ice and Icebergs*, S. Haykin, E. O. Lewis, R. K. Raney, and J. R. Rossiter, Eds., John Wiley & Sons, 1994, p. 142.

[21] D. V. Fitterman and V. F. Labson, "Chapter 10: Electromagnetic induction methods for environmental problems," in *Near Surface Geophysics*, D. K. Butler, Ed. Society of Exploration Geophysicists, ISBN 1-56080-130-1, 2005, p. 303.

[22] E. O. Lewis, C. E. Livingstone, C. Garrity, and J. R. Rossiter, "Properties of snow and ice," in *Remote Sensing of Sea Ice and Icebergs*, S. Haykin, E. O. Lewis, R. K. Raney, and J. R. Rossiter, Eds., John Wiley & Sons, 1994, p. 65.

[23] F. Jones, "Geophysics foundations: Model types produced by geophysical work," University of British Columbia, June 2007. https://www.eoas.ubc.ca/ubcgif/iag/foundations/modelytpes.htm

[24] Geotech Limited. http://geotech.ca/resources/glossary/

[25] F. J. Herrmann, "EOSC 454 – Applied Geophysics," The University of British Columbia – Vancouver, 2008. Available: https://www.eoas.ubc.ca/courses/eosc454/content/Electromagnetics%201.0%20Fundamentals.pdf

[26] Geonics Limited. http://www.geonics.com/html/em31-mk2.html.

[27] Geophysical Survey Systems, Incorporated. http://www.geophysical.com/Documentation/Brochures/GSSI-ProfilerBrochure.pdf

[28] J. R. Wait, *Electromagnetic Waves in Stratified Media*, Pergamon Press, 1962, 372 p.

[29] A. Pfaffling, C. Haas, and J. E. Reid, "Direct helicopter EM – Sea-ice thickness inversion assesses with synthetic and field data," *Geophys.* **72**(4), 127-137 (2007). doi: 10.1190/1.2732551

[30] W. L. Anderson, "Numerical integration of related Hankel transforms of orders 0 and 1 by adaptive digital filtering," *Geophys*. **44**(7), 1287-1305 (1979). doi:10.1190/1.1441007

[31] C. A. Balanis, *Advanced Engineering Electromagnetics*, John Wiley & Sons: New York, 1989.

[32] C. Haas C, S. Gerland, H. Eicken, and H. Miller, "Comparison of sea-ice thickness measurements under summer and winter conditions in the Arctic using a small electromagnetic induction device," *Geophys*. **62**(3), 749-757 (1997).

[33] H. Eicken H, W. B. Tucker III, and D. K. Perovich, "Indirect measurements of the mass balance of summer Arctic sea ice with an electromagnetic induction technique," *Ann. Glaciol.* **33**(1), 194-200 (2001). doi:10.3189/172756401781818356

[34] W. H. Press, S. A. Teukolsky, W. T. Vetterling, and B. P. Flannery, *Numerical Recipes: The Art of Scientific Computing*, 3rd Edition, Cambridge University Press, 2007, p. 797.

[35] C. Geiger, H. R. Mueller, J. P. Samluk, E. R. Bernstein, and J. Richter-Menge, "Impact of spatial aliasing on sea ice thickness measurements," *Ann. Glaciol*. **56**(69), 353-362 (2015). doi: 10.3189/2015AoG69A644

[36] A. Barron and J. Kim, "Introduction to statistics: Life sciences," 1997, Yale University. http://www.stat.yale.edu/Courses/1997-98/101/confint.htm

[37] H. Ward and G. W. Hohmann, "Electromagnetic theory for geophysical applications," in *Electromagnetic Methods in Applied Geophysics-Theory,* Vol. 1., M. Nabighian, Ed. Society of Exploration Geophysicists, Tulsa, 1988.

[38] G. Keller and F. Frischknecht, *Electrical Methods in Geophysical Prospecting*, Pergamon Press, Oxford, 1966, pp 330-335.

[39] F. S. Grant and G. F. West, *Interpretation Theory in Applied Geophysics*, McGraw-Hill, New York, 1965, pp. 444-546.

[40] S. Orfanidis, *Electromagnetic Waves and Antennas*, Rutgers University, 2014, p. 13. Available: http://www.ece.rutgers.edu/~orfanidi/ewa/ch01.pdf

[41] C. J. Weiss, "The electromagnetic response of a layered earth to an inductively-coupled, circular-loop antenna," Virginia Tech, 2010, p. 16.

[42] F. T. Ulaby, *Fundamentals of Applied Electromagnetics*, Pearson Prentice Hall, 2004, p. 14-18, 22.

[43] R. F. Harrington, *Time-Harmonic Electromagnetic Fields*, McGraw-Hill Book Co., New York, 1961, p. 19, 129-134.

[44] W. H. Hayt, J. E. Kemmerly, S. M. Durbin, *Engineering Circuit Analysis*, McGraw-Hill, New York, 2002, p. 192.

[45] A. Baños, *Dipole Radiation in the Presence of a Conducting Half-Space*, Permagon Press, 1966, 245 p.

[46] F. Bowman, *Introduction to Bessel Functions*, Dover Publications, 2010, 160 p.

[47] A. Sommerfeld, *Partial Differential Equations in Physics,* Academic Press, 1949, p. 242.

[48] A. Erdélyi, Ed., *Tables of Integral Transforms*, McGraw-Hill Book Co., New York, 1954, 391 p.

[49] R. Lyons, "Quadrature signals: Complex, but not complicated," *IEEE Long Island Section*. Available: http://www.ieee.li/pdf/essay/quadrature_signals.pdf, (2008).

[50] A. E. Beck, *Physical Principles of Exploration Methods*, Macmillan Press Ltd., Hong Kong, 1981, p. 127.

[51] C. J. Weiss, "Project APhiD: A Lorenz-gauged **A**-Φ decomposition for parallelized computation of ultra-broadband electromagnetic induction in a fully heterogeneous Earth," *Comput. Geosci*. **58**, 40-52 (2013). doi: 10.1016/j.cageo.2013.05.002

[52] J. A. Heras, "How the potentials in different gauges yield the same retarded electric and magnetic fields," *Am. J. Phys.* **75**(2), 176-183 (2007). doi: 10.1119/1.2400238

[53] J. P. Samluk, C. A. Geiger, and C. J. Weiss, "3D electromagnetic induction field simulations of level and deformed sea ice," *Ann. Glaciol.* **56**(69), 405-414 (2015). doi: 10.3189/2015AoG69A737

[54] K. Yee, "Numerical solution of initial boundary value problems involving Maxwell's equations in isotropic media," *IEEE T. Antenn. Propag.* **14**(3), 302-307 (1966). doi: 10.1109/TAP.1966.1138693

[55] R. W. Freund and N. M. Nachtigal, "QMR: a quasi-minimal residual method for non-Hermitian linear systems," *Numer. Math.* **60**(1), 315-339 (1991).

[56] A. A. Pfaffhuber, S. Hendricks S, Y. A. Kvistedal, "Progressing from 1D to 2D and 3D near-surface airborne electromagnetic mapping with a multisensory, airborne sea-ice explorer," *Geophys.* **77**(4), WB109-WB117 (2012). doi: 10.1190/geo2011-0375.1

[57] ParaView by Kitware. http://www.paraview.org

[58] A. J. Witten, *Handbook of Geophysics and Archeology*, Equinox Publishing Ltd., 2006, p.133, 139-146, 166-170, 215-216, 234-236.

[59] B. E. A. Saleh and M. C. Teich MC, *Fundamentals of Photonics*, John Wiley and Sons, 1991, p. 85, 121.

[60] C. Haas, V. Alexandrov, S. Kern, J. Lieser, J. Lobach, T. Martin, A. Pfaffling, and S. Willmes, "Sea ice remote sensing, thickness profiling, and ice and snow analyses during Polarstern cruise Ark 19/1 / CryoVex2003 in the Barents Sea and Fram Strait, February 28 – April 24, 2003: Cruise report," p. 18-19 (2003).

[61] A. Pfaffling, *Helicopter electromagnetic sea ice thickness estimation: An induction method in the centimeter scale*, PhD Thesis, Alfred Wegener Institute, 2006, p. 15.

[62] B. Anderson B and T. Barber, *Induction Logging*, Schlumberger Wireline and Testing, Document SMP-7056, 1997, 45 p.

[63] D. Beard, Q. Zhou, E. Bigelow, "Practical applications of a new multichannel and fully digital spectrum induction system," Presented at the SPE Annual Technical Conference and Exhibition, Denver, Colorado, SPE-36504-MS (1996).

[64] R. Beste, T. Hagiwara, G. King, R. Strickland, and G. A. Merchant, "A new high resolution array induction tool," Presented at the SPWLA 41st Annual Logging Symposium, SPWLA-2000-C (2000).

[65] G. Liu and A. Becker, "Two-dimensional mapping of sea ice keels with electromagnetics," *Geophys.* **55**(2), 239-248 (1990). doi: 10.1190/1.1442832

[66] J. Gardner, J. Richter-Menge, S. Farrell, and J. Brozena, "Coincident multiscale estimates of Arctic sea ice thickness," *EOS, Trans. Amer. Geophys. U.* **93**(6) 57-58 (2012). doi: 10.1029/2012EO060001

[67] W. Bangerth, "Finite element methods in scientific computing," Texas A&M University. Available: http://www.math.tamu.edu/~bangerth/videos/676/slides.34.pdf

[68] G. Baddeley, "GPS – NMEA Sentence Information," accessed online: http://aprs.gids.nl/nmea/#gga (2001).

[69] Geophysical Survey Systems, Incorporated. *Profiler EMP-400 User's Manual*, p. 34.

[70] B. P. Weissling and M. J. Lewis, "A report on sea ice sounding field trials of the GSSI EMP-400 electromagnetic induction meter," Unpublished report furnished by Geophysical Survey Systems, Incorporated, Nashua, NH (2008).

[71] J. D. McNeill, "Technical note TN-31: Why doesn't Geonics Limited build a multi-frequency EM31 or EM38?" Geonics Limited, November, 1996.

[72] Rogue Wave Software, Incorporated. http://www.roguewave.com/products-services/pv-wave/technical-specs

[73] C. A. Geiger, T. L. Deliberty, R. Kane, and J. P. Samluk (2015) *ACADIS Archive of Raw and Processed Data from NSF Project ARC-1107725: Precision, Accuracy, and Aliasing of Sea Ice Thickness from Multiple Observing Platforms,* https://www.aoncadis.org/project/SeaIceThickness_PrecisionAccuracyAliasing.html

[74] SEDNA: Sea Ice Experiment – Dynamic Nature of the Arctic. Data Archive (2007), available: http://research.iarc.uaf.edu/SEDNA/data.php

[75] S. J. Leon, *Linear Algebra with Applications*, Prentice Hall, 2002, p. 1, 75.

[76] S. Haykin, *An Introduction to Analog and Digital Communications*, John Wiley and Sons, New York, 1989, p. 160.

[77] S. W. Smith, *The Scientist and Engineer's Guide to Digital Signal Processing*, California Technical Publishing, 1997, p. 17.

[78] U.S. Department of Commerce, *NIST/SEMATECH e-Handbook of Statistical Methods*, April 2012. Available: http://www.itl.nist.gov/div898/handbook/eda/section3/histogr6.htm

[79] A. Dinsmore, "Propagating uncertainties – a primer," 2009, University of Massachusetts. Available: http://courses.umass.edu/phys286/Propagating_uncertainty.pdf

[80] W. Bauer, "Error Propagation," 1999, Michigan State University. Available: http://lectureonline.cl.msu.edu/~mmp/labs/error/e2.htm

[81] C. Sampson, K. M. Golden, A. Gully, A. P. Worby, "Surface impedance tomography for Antarctic sea ice," *Deep-Sea Res. Pt. II* **58**(9-10), 1149-1157 (2011). doi: 10.1016/j.dsr2.2010.12.003

[82] S. Chatterjee and B. Price, *Regression Analysis by Example*, John Wiley & Sons, New York, 1977, p. 63.

[83] A. G. McNish, "Physical constants and conversion factors," in *Handbook of Mathematical Functions*, M. Abramowitz and I. A. Stegun, Eds. Dover Publications, New York, 1965, p. 14.

Appendix A

PERMISSIONS

International Glaciological Society

Scott Polar Research Institute,
Lensfield Road,
Cambridge, CB2 1ER, UK
Tel: +44 (0)1223 355 974
Fax: +44 (0)1223 354 931
E-mail: igsoc@igsoc.org
Web: http://www.igsoc.org

Mr J P Samluk
University of Delaware
140 Evans Hall
Newark
DE
19716
USA

24 April 2016

Dear Mr Samluk

We are pleased to give you permission to use the paper below in your dissertation. The permission covers the use of the paper in paper form or in such electronic forms as are now known, and in future reprints and all languages.

Samluk, J P, Geiger, C A, Weiss & Chester, J (2015) Full-physics 3-D heterogeneous simulations of electromagnetic induction fields on level and deformed sea ice. *A. Glaciol.,* **56** (69), pp405–414.

The acknowledgment should read '*reprinted from the Annals of Glaciology with permission of the International Glaciological Society'* or similar.

Sincerely,

Magnús Már Magnússon
Secretary General

Appendix B

APPARENT CONDUCTIVITY FROM A GEOPHYSICAL STANDPOINT

Relative to terminology in [6], the relationship between apparent conductivity, ratios in magnetic fields, and material conductivity is expressed as follows (refer to Figure 2-1 for a visual reference):

$$\sigma_a = \frac{4}{\omega\mu_0 r^2}\left(\frac{\mathbf{H}_s}{\mathbf{H}_p}\right) \approx j\sum_{n=1}^{N}\sigma_n\left[\int_{\zeta_{n-1}}^{\infty}\phi(\zeta)\,d\zeta - \int_{\zeta_n}^{\infty}\phi(\zeta)\,d\zeta\right] \tag{B.1}$$

$$\sigma_a = j\sum_{n=1}^{N}\sigma_n\left[R_{n-1} - R_n\right] \tag{B.2}$$

where:

σ_a = the apparent conductivity at instrument receiver location (mS/m)

$\omega = 2\pi f$

μ_0 = the magnetic permeability of free space (4π x 10^{-7} H/m)

$\mathbf{H}_s$ = the secondary magnetic field (A/m)

$\mathbf{H}_p$ = the primary magnetic field (A/m)

σ_n = the conductivity of material at location n

ϕ = the relative response function at point n as a function of ζ

$\zeta = z/r$

z = the depth (m)

r = the coil separation length (m)

n = locations 1 to N where each location is the same size

$\gamma = \sqrt{j\omega\mu_0\sigma}$

f = coil separation length (m)

σ = electric conductivity (mS/m)

$\delta = \sqrt{\dfrac{2}{\omega\mu_0\sigma}} = \dfrac{\sqrt{2j}}{\gamma}$ = skin depth (m); e-folding signal strength

$\Psi = \dfrac{r}{\delta}$ = induction number.

Assumptions:

1.) $\gamma r << 1;\ \Psi << 1$

2.) Composite layers are horizontal and each layer is uniform

$$\phi_V(\zeta) = \frac{4\zeta}{\left(4\zeta^2+1\right)^{3/2}}$$

$$\phi_H(\zeta) = 2 - \frac{4\zeta}{\left(4\zeta^2+1\right)^{1/2}}$$

Cumulative Response: $R(\zeta) = \int_{\zeta}^{\infty} \phi(\zeta)\, d\zeta$

where:

$$R_V(\zeta) = \frac{1}{\left(4\zeta^2+1\right)^{1/2}}$$

$$R_H(\zeta) = \left(4\zeta^2+1\right)^{1/2} - 2\zeta$$

Special Cases:

$$R_0(\zeta) = \int_{\zeta=0}^{\infty} \phi(\zeta)\, d\zeta = 1 \tag{B.3}$$

$$R_N(\zeta) = \int_{\zeta=N}^{\infty} \phi(\zeta)\, d\zeta = 0\ , \tag{B.4}$$

such that a general numerical solution through superposition is

$$\sigma_a = j\sum_{n=1}^{N} \sigma_{a_n} \tag{B.5}$$

$$n = 1 : \sigma_{a_1} = j\sigma_1\left[R_0 - R_1\right] = j\sigma_1\left[1 - R_1\right] \tag{B.6}$$

$$1 < n < N : \sigma_{a_n} = j\sigma_n \left[R_{n-1} - R_n \right] \tag{B.7}$$

$$n = N : \sigma_{a_N} = j\sigma_N \left[R_{N-1} - R_N \right] = j\sigma_N \left[R_{N-1} - 0 \right] = j\sigma_N R_{N-1} \ . \tag{B.8}$$

Appendix C

APhiD DIPOLE LOOP CONFIGURATION

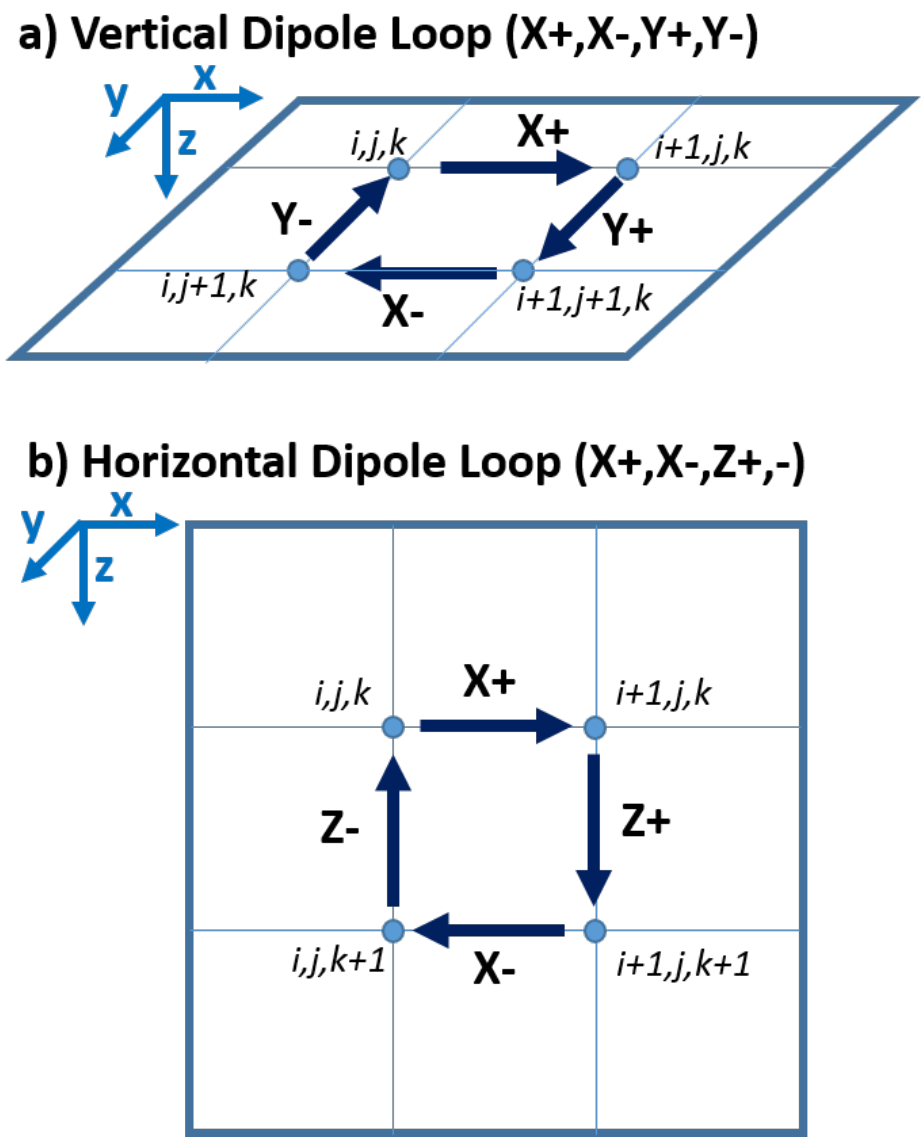

Figure C-1. Schematic of how a dipole loop is configured in the APhiD model with (a) a vertical dipole (HCP mode) and (b) a horizontal dipole (VCP mode).

Appendix D

CO-CALIBRATION ROUTINE DERIVATIONS

As stated in Chapter 5, the following set of linear equations is used as the starting point to determine the material conductivities of σ_1 and σ_2 used in the developed co-calibration routine. Equation 5.7 is repeated here:

$$\begin{aligned} \sigma_a &= \sigma_1\left[R_{a0} - R_{a1}\right] + \sigma_2 R_{a1} \\ \sigma_b &= \sigma_1\left[R_{b0} - R_{b1}\right] + \sigma_2 R_{b1} \end{aligned} \quad . \tag{D.1}$$

First, σ_2 can be defined for in terms of solving for σ_1 first by rearranging terms, such as,

$$\sigma_1 = \frac{\sigma_a - \sigma_2 R_{a1}}{R_{a0} - R_{a1}} = \frac{\sigma_b - \sigma_2 R_{b1}}{R_{b0} - R_{b1}} \quad . \tag{D.2}$$

Then, σ_1 is substituted into σ_a in the following manner,

$$\sigma_a = \frac{\sigma_b - \sigma_2 R_{b1}}{\left[R_{b0} - R_{b1}\right]}\left[R_{a0} - R_{a1}\right] + \sigma_2 R_{a1} \ , \tag{D.3}$$

where expanding terms leads to

$$\sigma_a = \frac{\sigma_b R_{a0} + \sigma_2 R_{b1} R_{a1} - \sigma_2 R_{b1} R_{a0} - \sigma_b R_{a1}}{R_{b0} - R_{b1}} + \sigma_2 R_{a1} \ . \tag{D.4}$$

Both sides of Equation D.4 can now be multiplied through by the denominator, resulting in the following form of

$$\sigma_a\left[R_{b0} - R_{b1}\right] = \sigma_b R_{a0} + \sigma_2 R_{b1} R_{a1} - \sigma_2 R_{b1} R_{a0} - \sigma_b R_{a1} + \sigma_2 R_{a1} R_{b0} - \sigma_2 R_{a1} R_{b1} \ . \tag{D.5}$$

The next several steps consist of placing σ_2 on one side, via a continuation of Equation D.5:

$$\sigma_a\left[R_{b0} - R_{b1}\right] - \sigma_b R_{a0} + \sigma_b R_{a1} = \sigma_2 R_{b1} R_{a1} - \sigma_2 R_{b1} R_{a0} + \sigma_2 R_{a1} R_{b0} - \sigma_2 R_{a1} R_{b1} \tag{D.6}$$

$$\sigma_a\left[R_{b0} - R_{b1}\right] - \sigma_b R_{a0} + \sigma_b R_{a1} = \sigma_2\left[R_{b1} R_{a1} - R_{b1} R_{a0} + R_{a1} R_{b0} - R_{a1} R_{b1}\right] \tag{D.7}$$

$$\frac{\sigma_a\left[R_{b0} - R_{b1}\right] - \sigma_b R_{a0} + \sigma_b R_{a1}}{\left[R_{b1} R_{a1} - R_{b1} R_{a0} + R_{a1} R_{b0} - R_{a1} R_{b1}\right]} = \sigma_2 \ , \tag{D.8}$$

where now σ_2 can be stated in final form as

$$\sigma_2 = \frac{\sigma_a\left[R_{b0} - R_{b1}\right] - \sigma_b\left[R_{a0} - R_{a1}\right]}{\left[R_{a1}R_{b0} - R_{b1}R_{a0}\right]} \quad . \tag{D.9}$$

A similar approach is used for defining σ_1 from the system defined in Equation D.1, but now σ_2 is solved first this time, starting with the following relationship:

$$\frac{\sigma_b - \sigma_1\left[R_{b0} - R_{b1}\right]}{R_{b1}} = \sigma_2 \quad . \tag{D.10}$$

Now Equation 5.6, stated as

$$\sigma_a = \sigma_1\left[R(\zeta_0)_{HCP,VCP} - R(\zeta_1)_{HCP,VCP}\right] + \sigma_2 R(\zeta_1)_{HCP,VCP} \quad , \tag{D.11}$$

can be substituted into the first part of the system in Equation D.1 as

$$\sigma_a = \sigma_1\left[R_{a0} - R_{a1}\right] + \sigma_2 R_{a1} \tag{D.12}$$

$$\sigma_a = \sigma_1\left[R_{a0} - R_{a1}\right] + \frac{\sigma_b - \sigma_1\left[R_{b0} - R_{b1}\right]}{R_{b1}} R_{a1} \quad , \tag{D.13}$$

where multiplying through the substitution of σ_1 results in the following equations:

$$\sigma_a = \sigma_1\left[R_{a0} - R_{a1}\right] + \frac{\sigma_b - \sigma_1 R_{b0} + \sigma_1 R_{b1}}{R_{b1}} R_{a1} \tag{D.14}$$

$$\sigma_a = \sigma_1\left[R_{a0} - R_{a1}\right] + \frac{\sigma_b - \sigma_1 R_{b0}R_{a1} + \sigma_1 R_{b1}R_{a1}}{R_{b1}} \quad . \tag{D.15}$$

Now, when the denominator is multiplied through on both sides of Equation D.15, the following relationship develops,

$$\sigma_a R_{b1} = \sigma_1 R_{a0}R_{b1} - \sigma_1 R_{a1}R_{b1} + \sigma_b R_{a1} - \sigma_1 R_{b0}R_{a1} + \sigma_1 R_{b1}R_{a1} \quad , \tag{D.16}$$

where putting σ_1 on one side results in the following steps:

$$\sigma_a R_{b1} - \sigma_b R_{a1} = \sigma_1 R_{a0}R_{b1} - \sigma_1 R_{a1}R_{b1} - \sigma_1 R_{b0}R_{a1} + \sigma_1 R_{b1}R_{a1} \tag{D.17}$$

$$\sigma_a R_{b1} - \sigma_b R_{a1} = \sigma_1\left[R_{a0}R_{b1} - R_{a1}R_{b1} - R_{b0}R_{a1} + R_{b1}R_{a1}\right] \tag{D.18}$$

$$\sigma_a R_{b1} - \sigma_b R_{a1} = \sigma_1\left[R_{a0}R_{b1} - R_{b0}R_{a1}\right] \quad . \tag{D.19}$$

Finally, σ_1 can be defined as

$$\sigma_1 = \frac{\sigma_a R_{b1} - \sigma_b R_{a1}}{R_{a0}R_{b1} - R_{b0}R_{a1}} \quad . \tag{D.20}$$

For defining the inversion solution of Z_1, Equation D.11 is used, and making the appropriate distributions leads to the following:

$$\sigma_a = \sigma_1 R(\zeta_0) - \sigma_1 R(\zeta_1) + \sigma_2 R(\zeta_1) \quad . \tag{D.21}$$

Since finding Z_1 is the objective, recall that $R(\zeta_1)$ is a function of ζ, which is the thickness divided by the coil spacing. So to receive Z_1 on one side, the following steps show the process:

$$\sigma_a - \sigma_1 R(\zeta_0) = -\sigma_1 R(\zeta_1) + \sigma_2 R(\zeta_1) \tag{D.22}$$

$$\sigma_a - \sigma_1 R(\zeta_0) = \sigma_2 R(\zeta_1) - \sigma_1 R(\zeta_1) \tag{D.23}$$

$$\sigma_a - \sigma_1 R(\zeta_0) = R(\zeta_1)(\sigma_2 - \sigma_1) \tag{D.24}$$

$$R(\zeta_1) = \frac{\sigma_a - \sigma_1 R(\zeta_0)}{\sigma_2 - \sigma_1} \quad . \tag{D.25}$$

Equation D.25 can also be set to the cumulative HCP or VCP response equations discussed in Chapter 2 (Equations 2.7 and 2.8, respectively). For the purposes of this dissertation, Equation D.25 will be set to the VCP response equation, expressed as

$$R(\zeta_1) = \frac{\sigma_a - \sigma_1 R(\zeta_0)}{\sigma_2 - \sigma_1} = \sqrt{4\left(\frac{Z_1}{r}\right)^2 + 1} - 2\left(\frac{Z_1}{r}\right) \quad . \tag{D.26}$$

Rearranging some terms leads to

$$\sqrt{4\left(\frac{Z_1}{r}\right)^2 + 1} = \frac{\sigma_a - \sigma_1 R(\zeta_0)}{\sigma_2 - \sigma_1} + 2\left(\frac{Z_1}{r}\right) \quad . \tag{D.27}$$

If both sides of Equation D.26 are squared, the result is

$$4\left(\frac{Z_1}{r}\right)^2 + 1 = \left(\frac{\sigma_a - \sigma_1 R(\zeta_0)}{\sigma_2 - \sigma_1} + 2\frac{Z_1}{r}\right)^2 \quad . \tag{D.28}$$

Expanding the right-hand side of Equation D.28 leads to the following equation:

$$4\left(\frac{Z_1}{r}\right)^2 + 1 = \left(\frac{\sigma_a - \sigma_1 R(\zeta_0)}{\sigma_2 - \sigma_1} + 2\frac{Z_1}{r}\right)^2 + 2\left(\frac{\sigma_a - \sigma_1 R(\zeta_0)}{\sigma_2 - \sigma_1}\right)\left(2\frac{Z_1}{r}\right) + \left(2\frac{Z_1}{r}\right)^2 \quad . \tag{D.29}$$

Combining terms results in

$$4\left(\frac{Z_1}{r}\right)^2-\left(2\frac{Z_1}{r}\right)^2-2\left(\frac{\sigma_a-\sigma_1 R(\zeta_0)}{\sigma_2-\sigma_1}\right)\left(2\frac{Z_1}{r}\right)=\left(\frac{\sigma_a-\sigma_1 R(\zeta_0)}{\sigma_2-\sigma_1}+2\frac{Z_1}{r}\right)^2-1 \quad . \text{(D.30)}$$

Some terms on the left-hand side cancel, and Equation D.30 can be restated as

$$4\left(\frac{\sigma_a-\sigma_1 R(\zeta_0)}{\sigma_2-\sigma_1}\right)\left(\frac{Z_1}{r}\right)=1-\left(\frac{\sigma_a-\sigma_1 R(\zeta_0)}{\sigma_2-\sigma_1}\right)^2 \quad . \qquad \text{(D.31)}$$

Finally, Z_1 can be expressed as

$$Z_1=\frac{r\left(1-\left(\frac{\sigma_a-\sigma_1 R(\zeta_0)}{\sigma_2-\sigma_1}\right)^2\right)}{4\left(\frac{\sigma_a-\sigma_1 R(\zeta_0)}{\sigma_2-\sigma_1}\right)} \quad , \qquad \text{(D.32)}$$

or, per Equation 5.21 restated here,

$$Z_1=\frac{r\left(1-R(\zeta_1)^2\right)}{4R(\zeta_1)} \quad . \qquad \text{(D.33)}$$